O[illegible] AL LABORATORY
operated by
UNION CARBIDE CORPORATION
NUCLEAR DIVISION
for the
U.S. ATOMIC ENERGY COMMISSION

ORNL - TM - 1988

THE MEASUREMENT OF HIGH-ENERGY CHARGE TRANSFER CROSS SECTIONS FOR INCIDENT PROTONS AND ATOMIC HYDROGEN IN VARIOUS GASES
and
THE K-, L-, AND M-AUGER, L-COSTER-KRONIG, AND THE CONVERSION-ELECTRON SPECTRA OF PLATINUM IN THE DECAY OF ^{195}Au
(Thesis)

L. H. Toburen
M. Y. Nakai
R. A. Langley

Submitted as a thesis by L. H. Toburen to the Graduate School of Vanderbilt University in partial fulfillment of the requirements for the degree of Doctor of Philosophy in Physics.

ORNL-TM-1988

Contract No. W-7405-eng-26

HEALTH PHYSICS DIVISION

THE MEASUREMENT OF HIGH-ENERGY CHARGE TRANSFER CROSS SECTIONS FOR INCIDENT PROTONS AND ATOMIC HYDROGEN IN VARIOUS GASES

and

THE K-, L-, AND M-AUGER, L-COSTER-KRONIG, AND THE CONVERSION-ELECTRON SPECTRA OF PLATINUM IN THE DECAY OF ^{195}Au

L. H. Toburen, M. Y. Nakai, and R. A. Langley

Submitted as a thesis by L. H. Toburen to the Graduate School of Vanderbilt University in partial fulfillment of the requirements for the degree of Doctor of Philosophy in Physics

NOVEMBER 1967

OAK RIDGE NATIONAL LABORATORY
Oak Ridge, Tennessee
operated by
UNION CARBIDE CORPORATION
for the
U.S. ATOMIC ENERGY COMMISSION

TABLE OF CONTENTS

TABLE OF CONTENTS (Continued) Page

TABLE OF CONTENTS (Continued) Page

LIST OF TABLES

LIST OF TABLES (Continued) Page

LIST OF ILLUSTRATIONS

LIST OF ILLUSTRATIONS (Continued) Page

LIST OF ILLUSTRATIONS (Continued) Page

LIST OF ILLUSTRATIONS (Continued) Page

LIST OF ILLUSTRATIONS (Continued) Page

PART I. THE MEASUREMENT OF HIGH-ENERGY CHARGE TRANSFER CROSS SECTIONS FOR INCIDENT PROTONS AND ATOMIC HYDROGEN IN VARIOUS GASES

SECTION A. SINGLE-ELECTRON CAPTURE AND LOSS CROSS SECTIONS OF INCIDENT PROTONS AND ATOMIC HYDROGEN IN THE ENERGY RANGE 100 TO 2500 keV

CHAPTER I

INTRODUCTION

During the past two decades a great deal of effort has been expended in the study of charge transfer or charge exchange reactions. Information on this type of collision is useful in the design of radiation detectors, in studies of the upper atmosphere, in astrophysics, in radiation damage studies and more recently in the development of controlled thermonuclear fusion devices and gas masers. The experimental determination of charge transfer cross sections is useful in the development of theoretical descriptions of atomic and molecular collision processes.

The accurate measurement of charge transfer cross sections has been encouraged by refinements in techniques such as the development of solid state particle detectors, a reliable capacitance manometer and ultrahigh vacuum techniques. The solid state detector makes possible the determination of very weak neutral particle intensities by counting techniques while the capacitance manometer is capable of accurate and continuous measurement of gas pressures as low as 5×10^{-5} torr. Pressure measurements made by means

of the capacitance manometer are also independent of the nature of the gas under study, including condensable gases. Previously, gas target densities were determined primarily by the use of McLeod gages which cannot be used for continuous pressure monitoring and which are incorrect for condensable gases. Ultrahigh vacuum systems are necessary to reduce charge transfer between the beam and residual gas molecules.

The electron capture cross sections (σ_{10}) and electron loss cross sections (σ_{01}) are measured in this work for incident protons and atomic hydrogen on the target gases H_2, He, Ar, Kr, N_2, O_2, CO, CO_2, H_2O, CH_4, C_2H_4, C_2H_6, and C_4H_{10}. The incident particle energies were from 100 to 2500 keV. This energy range should lie within the range of validity of the Born and impulse approximations and the impact parameter formulation used in cross section calculations. Chapter II describes briefly the theoretical approaches made in the calculation of charge transfer cross sections. Chapter III contains descriptions of the apparatus used, the measurement technique and methods of data analysis. The experimental results are presented in Chapter IV along with previous experimental and theoretical work. A discussion of the possible uncertainties and evaluation of these uncertainties is given in Chapter V.

CHAPTER II

THEORY

A. Introduction

There have been numerous theoretical approaches to the calculation of cross sections for electron capture and electron loss by incident proton and atomic hydrogen beams. The majority of this work has been concerned with the calculation of cross sections for electron capture by incident protons on atomic hydrogen targets. This, the simplest of all charge transfer processes, is in general a three-body problem with its many computational difficulties.

In the electron capture process the electron jumps from the bound state of the target atom to a bound state of the projectile with the difference in energy between the two bound states being absorbed in the relative translational energy of the two heavy particles. The capture process is complicated by the possibility that the electron may be captured into one of many bound states of the projectile. In the electron loss process an electron is ejected from a bound state of the projectile into the continuum. The initial and final states of the charge transfer systems have the same total energy; however, the wave functions representing them are not necessarily orthogonal. This non-orthogonality results from the fact that the

non-interacting initial and final states of the charge transfer process are described by different Hamiltonians.

In this chapter a brief description of the major theoretical approaches to high-energy charge transfer will be given. Detailed reviews of the theoretical studies of the charge transfer process may be found in several papers, for example, references 1 through 4.

B. Classical Calculations

A theoretical treatment of the electron capture phenomenon was first attempted by Fowler[5] who compared the balance between capture and loss of electrons by α-particles. He^{++} and He^{+} were considered as existing in thermodynamic equilibrium in an electron atmosphere with the electron density comparable to the electron density in an atom. The temperature was selected such that the average electron velocity was equal to the α-particle velocity. These considerations were found to yield suggestive agreement with the experimental results; however, this method is not reliable when the electron velocities are small compared to incident particle velocities.

A detailed classical theory for the capture of electrons by α-particles has been developed by Thomas.[6] The work of Thomas was based on the assumption that electron capture occurs as a result of two successive close collisions; the first between the incident particle and the electron and

the second between the electron and the target nucleus. It was assumed that, as a result of the first collision, the electron was deflected towards the nucleus with speed approximately equal to that of the incident particle. In the second collision the electron was deflected with no change in speed to a path parallel to the incident particle. The two scattering events occur at a fixed separation r, which is taken to be the appropriate Bohr radius. With these assumptions the cross section for electron capture from hydrogen was found to vary as v^{-11}, where v is the velocity of the incident particle.

The validity of the Thomas result has been questioned by Cook,[7] who pointed out that the Thomas picture fails at all velocities. Cook based his statement on the failure of Thomas' results to satisfy uncertainty relationships at high energy and on the lack of a velocity dependent cut-off to the separation r at which the scattering events occur.

The classical theory of Thomas has recently been investigated by Bates and Mapleton,[8] who introduce a modification involving the distribution of electrons in phase space. The capture cross section calculated for incident protons has the form

$$\sigma_{10} \propto E^{-11/4} \lambda^{3/4} C \qquad (1)$$

where E is the proton energy, λ is a parameter derived from the atomic potential and, as a result of the modification made to the Thomas theory, C is a function of E/J. The quantity J is the ionization potential of the target atom. A scaling factor can be deduced from Equation (1) which when

multiplied by the experimental cross section should result in a parameter that is independent of the target atom. This parameter is given by

$$\mathrm{P} = \frac{\sigma_{10} E^{11/4}}{\lambda^{3/4}} \quad . \tag{2}$$

Bates and Mapleton plotted P versus E/J for several different target atoms. Their results showed the experimental data to fit a single curve quite well for incident proton energies less than 300 keV. Although the theory was designed for fast encounters, the accord with experimental data is poor at high energies. This failure of the theory at high energies is due partially to not accounting for the electron shell structure of the target atom. Most recently Bates and Mapleton[9] have included the effects of electron shell structure in the calculation of electron capture cross sections for the target atoms argon and neon. The inclusion of shell structure in this calculation brings about much better agreement with experimental results.

Electron capture cross sections have been estimated by Bohr[10] by simple statistical considerations. The orbital electrons are subject to a momentum change due to the passage of a charged particle. The capture of an electron can result from any collision in which an energy of the order $\frac{1}{2}m_e v^2$ is transferred to an electron with orbital velocity comparable to the incident particle velocity $\underline{v}$. The statistical distribution of energy transferred in a collision was deduced by mechanical considerations of energy and momentum transfer for particles interacting through a force which is inversely

proportional to the square of their separation. By means of these considerations, the probability for transfer of sufficient energy to cause electron capture was found to be proportional to v^{-4}. The probability of electron capture also depends on the fraction f of velocity space containing electrons of velocity $\underline{v}$ and on the number of electrons n [$n \propto Z^{1/3} v$] in this velocity space. These quantities, f and n, are deduced from Coulomb field strengths within the target atoms. The above considerations result in the capture cross section

$$\sigma_{10} \propto Z_1^5 Z_2^{1/3} v^{-6} \tag{3}$$

where Z_1 is the atomic number of the projectile and Z_2 is the atomic number of the target.

The electron loss cross sections estimated by Bohr[10] were also deduced from statistical considerations of energy and momentum transfer. Sufficient energy must be transferred during the collision to remove an electron from the projectile atom. For close encounters with target atoms of low atomic number the ionizing effects of the atomic particles within the target act nearly independent of each other. The electron loss cross sections for light target elements were given by Bohr as

$$\sigma_{01} \propto (Z^2 + Z) v^{-2} \tag{4}$$

where Z is the atomic number of the target and $\underline{v}$ is the velocity of the incident particles. For target atoms of higher atomic number the atomic

particles within the target do not act independently on the projectile and the total interaction will more resemble that of a screened nuclear field. The electron loss cross sections for target atoms of high atomic number are given as

$$\sigma_{01} \propto Z^{2/3} v^{-1} \quad . \tag{5}$$

The effects of screening on the electron loss cross sections for targets of low atomic number have been investigated by Dmitriev and Nikolaev[11] in the free-collision approximation. In the free-collision approximation "resonance effects", i.e., cases of electron loss in long-range collisions with a small change in the momenta of the colliding particles, were neglected. The expression for the electron loss cross sections obtained in this calculation includes Bohr's formula as a special case. At high velocities of the incident particle the free-collision approximation gives results identical with those obtained in the Born approximation.

More recently Gryzinski[12] has developed a classical theory for inelastic atomic collisions which is described by Coulomb-type interactions between the particles and depends on the binding energy and momentum distribution of the electrons. This approximation is based on a binary collision concept, i.e., the independent pair interactions of the individual elements of the colliding systems. His calculations include (1) ionization of atoms and molecules by light particles (electrons), as well as by heavy particles (protons, deuterons), including inner-shell ionization and double ionization; (2) excitation of singlet

and triplet lines; (3) capture of electrons from atoms by moving ions; (4) slowing down of heavy charged particles, and (5) inelastic scattering of electrons on atoms and nuclei. The electron capture cross section calculations are applicable to the present work. For incident proton energies greater than 300 keV the cross sections calculated for electron capture from hydrogen targets decrease with the inverse sixth power of the impact velocity. This velocity dependence is to be compared with the $v^{-10.6}$ dependence found in the present work for electron capture from hydrogen by protons.

C. Born Approximation

When the velocity of relative motion of the colliding systems is high, the cross section for a given process may be obtained by the use of the first Born approximation. In this approximation it is assumed that the incident and scattered waves associated with the relative motion are plane waves and that all transition matrix elements are small compared with unity. A further assumption which is usually made is that there is no Pauli Principle exchange of electrons between the systems. The Born approximation cross section for the capture of an electron from a stationary atom Z (mass = AM) into a final state f of a projectile atom Z' (mass = $A'M$) is given by*

$$\frac{d\sigma_f}{d\Omega} = \left(\frac{\mu_f}{2\pi\hbar^2}\right)^2 \left(\frac{v'}{v}\right) \left| I_f \right|^2 \qquad (6)$$

with

*The notation is that of reference 20.

$$I_f = \int \exp(-i\underline{k}' \cdot \underline{R}') \Psi_f^*(\underline{r}') V \exp(i\underline{k} \cdot \underline{R}) \Psi_o(\underline{r}) d\underline{r} d\underline{R} \tag{7}$$

where $\Psi_o(\underline{r})$ is the ground state wave function for the electron in atom Z; $\Psi_f(\underline{r}')$ is the wave function for the electron in state f of atom Z′; $\underline{R}$ and $\underline{r}$ are the coordinates of the initial ion and electron with respect to the center of mass of the stationary atom Z; $\underline{R}'$ and $\underline{r}'$ are the corresponding coordinates with respect to the moving atom Z′ following charge transfer; V is the interaction potential and $\underline{k}$ and $\underline{k}'$ are defined by $h\underline{k} = \mu_i \underline{v}$ and $h\underline{k}' = \mu_f \underline{v}'$, respectively. The quantities μ_i and μ_f are the reduced masses of the initial and final systems, respectively; $\underline{v}$ is the velocity of the incident particle relative to atom Z at rest and $\underline{v}'$ is the corresponding outgoing velocity of atom Z′ relative to the stripped atom Z. Conservation of energy requires that

$$1/2\,\mu_i v^2 - \epsilon = 1/2\,\mu_f v^2 - \epsilon' \tag{8}$$

where ϵ, ϵ' are the binding energies of the electrons in atoms Z, Z′.

The direct calculation of charge transfer cross sections is hampered by several difficulties:

1) The interaction potential prior to the charge transfer is, in general, different from the interaction potential following the charge transfer and it is not clear which form of the interaction is best to use.

$$V_i = \frac{Z'Ze^2}{|\underline{R} + [m/(AM + m)]\underline{r}|} - \frac{Z'e^2}{|\underline{R} - [AM/(AM + m)]\underline{r}|} \tag{9}$$

$$V_f = \frac{Z'Ze^2}{|\underline{R}' - [m/(A'M + m)]\underline{r}'|} - \frac{Ze^2}{|\underline{R}' + [A'M/(A'M + m)]\underline{r}'|} \qquad (10)$$

2) Since the non-interacting initial and final states are described by different Hamiltonians, the initial and final state wave functions are not necessarily orthogonal; and

3) The wave functions Ψ_o and Ψ_f are in many cases not known.

The first attempts to calculate the cross section in the Born approximation were for a very simplified version of the charge transfer process. This simple picture consisted of an incident proton capturing an electron from a hydrogen atom. This system was first investigated by Oppenheimer,[13] Brinkman and Kramers,[14] and Massey and Smith[15] who considered the interaction potential to be simply the Coulomb interaction between the incoming proton and the atomic electron. The argument in support of this approximation of the interaction potential was that at proton energies greater than 50 keV, where the Born approximation should be valid, it appears legitimate to replace the protons by classical centers of force; thus, the original three body problem can be reduced to a one body problem. With this replacement, it can be proved rigorously[16] that the electron capture cross section is independent of the proton-nucleus interaction. One can also argue from a physical point of view that the proton-nuclear interaction should cause only a slight deflection of the moving proton which would not be expected to affect the probability of electron capture. The lack of

orthogonality between the wave functions was ignored in the early calculations; however, it was recognized in the work of Oppenheimer.[13] The numerical results of these calculations were higher than the early experimental results of Keene,[17] Ribe,[18] and Whittier[19] by a factor of 3 to 4 for proton energies near 100 keV. However, the velocity dependence, $\sigma_{10} \propto v^{-12}$, derived by these authors is similar to experimental results.

In order to reduce the discrepancies between theory and experiment, Jackson and Schiff[20] and Bates and Dalgarno[21] included the proton-nucleus interaction as part of the total interaction potential. Equations (9) and (10) are the total prior and post interaction potentials, respectively, as given by Jackson and Schiff. These potentials include the p-p and p-e Coulomb interactions; however the lack of orthogonality is still not included in the calculations of these authors. Jackson and Schiff have shown that the results obtained by means of the prior interaction and those of the post interaction are identical provided exact wave functions are used for the initial and final states. They also show that capture into the n^{th} excited state of hydrogen is proportional to n^{-3}. These results obtained with inclusion of the p-p interaction were found to be in very close agreement with the experimental data at proton energies of approximately 100 keV. The good agreement with experimental results obtained in this calculation implies that the use of the whole perturbation Hamiltonian in an approximate calculation of the capture process greatly improves the convergence of the approximation scheme,

even though it can be shown that some parts of the perturbation will give rise to negligible effects in an exact calculation.

Due to the various arguments from a physical point of view in which it was pointed out that the proton-nucleus interaction should be negligible, and because of the work of Drisko[22] which showed that the second order Born contribution of the proton-nucleus interaction canceled the first order contribution, several authors sought to improve upon this aspect of the theory. One method attempted was the use of the distorted wave approximation. This approximation, as described by Bassel and Gerjuoy,[23] is performed by replacing the plane waves in the matrix elements for the collision amplitude by distorted waves. The distortion of the incident wave is induced by the Coulomb interaction. This distortion is in effect a way of obtaining orthogonality between the initial and final state wave functions and as a result the matrix element of the proton-nucleus interaction can be neglected with an error of the order of the ratio of electron to proton masses. This result was also obtained by Bates[24] who took explicit account of the non-orthogonality of the wave functions by means of an effective interaction potential. The results of these calculations for protons on hydrogen show close agreement with experimental values for proton energies in the region 35 to 200 keV with discrepancies occurring at higher energies.

The Born approximation has been used by Mapleton in the calculation of electron capture cross sections for protons on several

different target atoms. His calculations include the electron capture cross sections for protons on hydrogen and helium[25] by means of both the proton-electron interaction potential and the more complete proton-electron plus proton-nucleus interaction. The results of these calculations indicate that the ratio of the cross sections obtained by means of the proton-electron interaction to the corresponding value obtained with the more complete interaction is nearly the same for both hydrogen and helium target atoms. In view of the similarity of this ratio for these two target atoms, Mapleton[25] proposed that cross sections which include the effects of the complete interaction potential could be calculated for any atom by first calculating the cross section by means of the proton-electron interaction potential and then multiplying the result by the ratio $\sigma_{(pe + pn)}/\sigma_{pe}$ calculated for helium or hydrogen. This method, which greatly simplifies the calculations for many-electron atoms has been used by Mapleton[26] in calculations of the electron capture cross sections for protons on nitrogen and oxygen. These calculations included electron capture of only 2p electrons from the target atom; therefore, at proton energies high enough for electron capture from inner shells to be energetically possible, the calculated results are expected to be too small. The results of the calculations are found to be in good agreement with experimental results up to approximately 800 keV where inner shell capture becomes energetically possible.

Mapleton has made several additional calculations which are refinements of the work described above. He used the six-parameter helium wave function of

Hylleras and both post and prior interaction potentials[27] in evaluating the electron capture cross sections for protons on helium. The post-prior discrepancy was usually less than 1% in the energy range investigated, 40 keV to 1 MeV. These results were slightly lower than the earlier values calculated by means of a simple helium wave function; however, the differences are generally less than 20%.

Mapleton[28] has also re-evaluated the electron capture cross sections for protons on nitrogen and oxygen. In this calculation more accurate atomic orbitals were used. The earlier values differ from the new results by less than 30%. Mapleton's most recent use of the Born approximation[29] has been in the calculation of cross sections for electron capture by protons from the inner electron shells of nitrogen. The results of this calculation are higher than the measured values by nearly a factor of two.

A simple generalization of the Born approximation involving only the proton-electron interaction has been used by Nikolaev[30] to calculate electron capture cross sections for protons on the target atoms H_2, He, Li, N_2, Ne, Ar, and Kr. The Brinkman-Kramers type calculation was generalized by the introduction of external screening parameters and capture probabilities were calculated for each electron shell of the target atom. The ratio of experimental to calculated cross sections was represented, accurate to approximately 25%, by a single-parameter function that is valid for all media. This function was used as a scaling factor in obtaining the final results of the calculated

cross section values. These calculations also show the importance of electron capture from inner electron shells of the target atom at incident proton energies above approximately 800 keV.

Further refinements in the first Born approximation which include a description of the rearrangement process in terms of a multi-channel scattering process have been reviewed in detail by Dalgarno.[4] This procedure removes the lack of orthogonality between the initial and final state wave functions by considering the wave functions to correspond to elastic scattering into particular scattering channels. The wave functions of the system are then written as a superposition of the various scattering channel eigenfunctions with particular states identified by properly defined projection operators.

It must be noted that the results of all the theoretical calculations described above are for atomic targets, whereas, the majority of the experimental results are for molecular targets. It has been generally assumed that for high-energy protons ($E > 50$ keV) a diatomic molecular target appears as two independent atoms to the incoming proton. The validity of this assumption has recently been investigated theoretically by Taun and Gerjuoy[31] for the case of protons on hydrogen. They point out that this assumption is valid, if it is valid at all, only as a result of accidental cancellation of a number of molecular effects which have no analog in the atomic reaction. They find that the ratio of the atomic cross section to the molecular cross section is very close to one half for $E < 400$ keV, whereas, at higher energies

this ratio reduces to 0.42. They arrived at these results by the application of molecular wave functions in the first Born approximation.

In the electron capture calculations carried out for protons on hydrogen, the results of the first Born approximation, which includes the more complete proton-nucleus interaction potential, tend asymptotically at high energies to the value $0.661\ \sigma_{BK}$. The quantity σ_{BK} is the Brinkman-Kramers result and is proportional to v^{-12}, where v is the incident proton velocity. The factor 0.661 arises presumably from the singularity of the proton-nuclear interaction potential. Drisko[22] has reported the results of a second Born approximation based upon a free particle Green's function which contained a v^{-11} term arising from successive scatterings of the electron by two nuclei. Explicitly he obtained the formula:

$$\sigma_{10} \propto (0.295 + \frac{5\pi v}{2^{10}})\ \sigma_{BK} \tag{11}$$

Drisko showed further that the third Born approximation would modify the v^{-12} term ($\sigma_{BK} \propto v^{-12}$) but leave the v^{-11} term unaltered. This work as well as that of Aaron et al.[32] suggests that the Born series for rearrangement collision diverges at high impact energies, if not for all energies. However, a more recent calculation,[33] which included more terms in the second order approximation, indicates that the Born series will converge even at high energies.

The Born approximation has also been applied by Bates and co-workers[34-37] to the calculation of the probability of excitations and electron loss for hydrogen atoms incident on target hydrogen and helium atoms. No account was taken of electron exchange; however, the total interaction potential was considered.

Calculations have been made which include transitions occurring in the target atom simultaneously with the loss of the electron from the incident atom. The results are in agreement with experimental values at particle energies of approximately 100 keV; however, the theoretical values fall off more slowly with energy than the measured values.

D. Impulse Approximation

In order to resolve the many difficulties associated with the Born approximation several authors have employed an impulse approximation in the study of the electron capture process. This calculation is described in detail by Bransden and Cheshire[38] and by McDowell[39] and in general by Dalgarno.[4] In the impulse approximation the effect of the binding energy of the electron in the initial state is neglected during the collision and the initial state vector $\phi_{i,\alpha}$ is replaced by a scattered wave which allows for distortion by the proton-electron interaction potential. The transition amplitude for transitions from an initial state α to a final state β is given by

$$T_{f,\beta;i,\alpha} = (\phi_{f,\beta}, V_\alpha \omega^+ \phi_{i,\alpha}) \tag{12}$$

where ω^+ is a two-body scattering operator and V_α is the interaction potential. The function $\omega^+ \phi_{i,\alpha}$ is evaluated by expanding $\phi_{i,\alpha}$ in terms of a complete set of free particle wave functions. This use of a distorted wave function

removes the proton-nuclear interaction since the initial and final state wave functions are orthogonal. In the high energy limit the cross section according to the impulse approximation has been evaluated by Bransden and Cheshire as

$$\sigma_{10} \propto (0.295 + \frac{5\pi v}{2^{11}})\, \sigma_{BK} \quad . \tag{13}$$

This result, which is for electron capture by protons on target hydrogen, differs from Drisko's results [Equation (11)] for the second Born approximation by a factor of 2 in the second term.

E. Impact Parameter Formulation

The impact parameter formulation has been described in detail by Bates and McCarroll.[1] This formulation exploits fully the simple behavior of the nuclei which, unless the energy is very low ($E < 25$ keV), may be taken to be that of classical particles of infinite mass. This method has also had considerable success at low energies ($E < 25$ keV) where the relative velocity is considered as the perturbation causing the charge transfer; this is the so-called perturbed stationary states calculation. At higher energies the Coulomb interaction is considered as the perturbation which causes the charge transfer. The impact parameter formulation involves difficulties similar to the first Born approximation; namely, the entire interaction potential must be used, proton-nucleus plus proton-electron, and the lack of orthogonality of the initial and final state wave functions must be considered.

The impact parameter method has been applied by McCarroll[40] to the reaction $H^+ + H\ (1S) \rightarrow H\ (1S) + H^+$. Full account was taken of momentum transfer and non-orthogonality of the wave functions of the initial and final states. This formulation is equivalent to the distorted wave formulation of Bassel and Gerjuoy;[23] however, the results of the impact parameter calculation are larger at low energies of the incident proton than the corresponding values calculated by Bassel and Gerjuoy. The results of McCarroll are 25% higher than those of Bassel and Gerjuoy at 25 keV, whereas, the discrepancy at 100 keV is approximately 5% and close agreement is obtained at proton energies greater than 200 keV.

CHAPTER III

EXPERIMENTAL METHOD

A. Apparatus

In the low-energy range (100-600 keV), protons were provided by a conventional gas-discharge ion source and accelerated by a 600 keV high-voltage supply. The voltage supply was extremely stable and had been calibrated to $\pm$ 2 kev by ^{19}F (p, γ) resonances at 340 and 483 keV. The proton beam was momentum analyzed by a 90° bending magnet before entering the first collision cell. The protons for the high-energy measurements (800-2500 keV) were accelerated by means of the ORNL 3-MeV Van de Graaff generator. This accelerator used a duoplasmatron[41] ion source which was employed in a pulsed mode with repetition rates in the range of 0.0315 to 2.00 MHz. The beam intensity was reduced to ensure that an average particle intensity of less than one particle per beam pulse struck the detector when counting techniques were used for beam detection. The proton energies were determined by a magnetic resonance probe in the 90° analyzing magnet at the base of the Van de Graaff generator. This probe had previously been calibrated to within $\pm$ 0.5% against the $^{7}Li(p,n)$ threshold.

The apparatus constructed for the cross section measurements is shown schematically in Figure 1 and a photograph of the apparatus is shown in Figure 2. The apparatus consists basically of two differentially pumped gas cells, two sets of electrostatic deflection plates for separation of beam charge states and detectors for the determination of the intensity of the neutral and charged components of the beam.

The circular apertures designed by a, b, c, c′, and d in Figure 1 were machined with knife edges of diameter 0.010, 0.062, 0.020, 0.020, and 0.062 inches, respectively. The respective diameters of the apertures were selected to minimize scattering of the beam. Alignment of the system was made possible by the use of bellows sections between apertures.

The length of the first collision cell, defined by apertures "a" and "b", was 17.50 ± 0.06 inches. Apertures "c" and "d" defined the length of the second collision cell which was also 17.50 ± 0.06 inches long. The dashed lines in Figure 1 indicate a modification of the second cell made during the experiment. The path length of the modified gas cell, defined by apertures "c′" and "d", was 3.00 ± 0.06 inches. Rapid evacuation of these collision cells was accomplished by means of a vacuum line by-pass. With the by-pass valve closed a pressure differential of approximately 1500 was obtained between the interior of the collision cell and the high vacuum region.

The electrostatic deflection plates shown in Figure 1 were 6 inches long and were separated by 1 inch. The insulation between the deflection plates and the chamber walls was sufficient to withstand voltages greater than 30 keV.

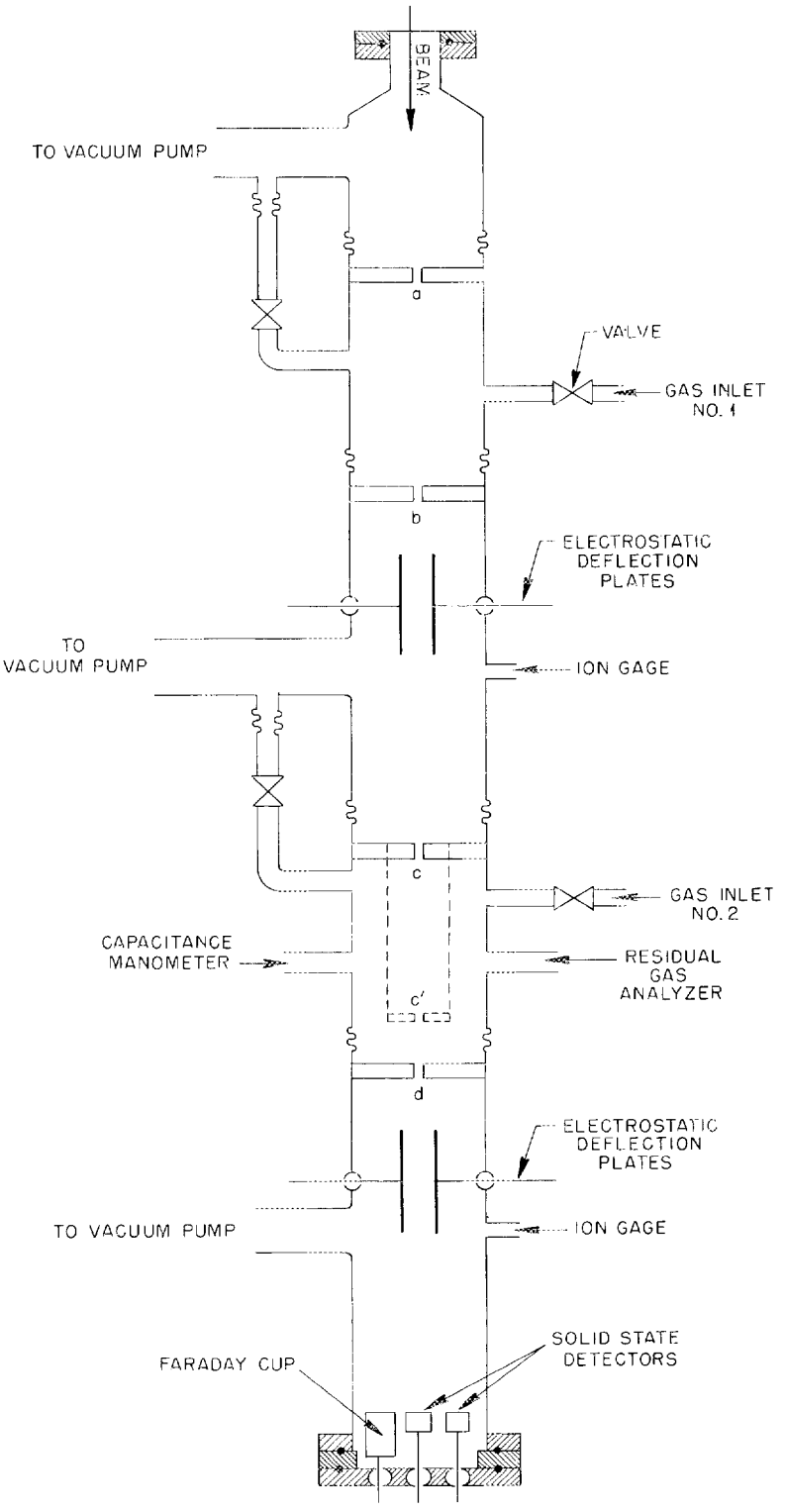

Fig. 1. A schematic drawing of the charge transfer apparatus.

PHOTO 83679

Fig. 2. A photograph of the charge transfer apparatus.

The entire vacuum system (excluding the beam detection assembly) was made from # 304 stainless steel and assembled using aluminum, copper, and gold "O"-rings. This construction enabled the system to be baked at temperatures of approximately 200°C by means of heater tapes which were wound around the vacuum chambers and insulated with asbestos. The system was pumped by three, 1500 liter/sec, NRC model HK6-1500 diffusion pumps containing DC 705 diffusion pump oil. The diffusion pump oil vapors were isolated from the high vacuum system by NRC series HW6 water-cooled baffles. Each diffusion pump was backed through an Ultec #50-055 foreline trap by a Duo Seal Model 1397 fore pump. An ultimate vacuum of 5×10^{-9} torr was obtained throughout the system before installation of the detectors. With the detector assembly in place the ultimate vacuum in the detector chamber was approximately 1×10^{-7} torr. This pressure was acceptable since the pressure in this chamber rose to approximately 2×10^{-7} torr when gas was introduced into the target chamber at pressures of 5×10^{-4} torr.

A cut-away view of the detector assembly is shown in Figure 3. This assembly consists of two movable plates (A and B) maintained vacuum tight by sliding on viton "O"-ring seals. Plate A provided for horizontal motion and plate B, which supported the detectors, provided for vertical motion. In this way two dimensional motion of the detectors with respect to the beam axis was obtained. This motion ensures that the detectors were centered with respect to the beam. The detectors were positioned such that

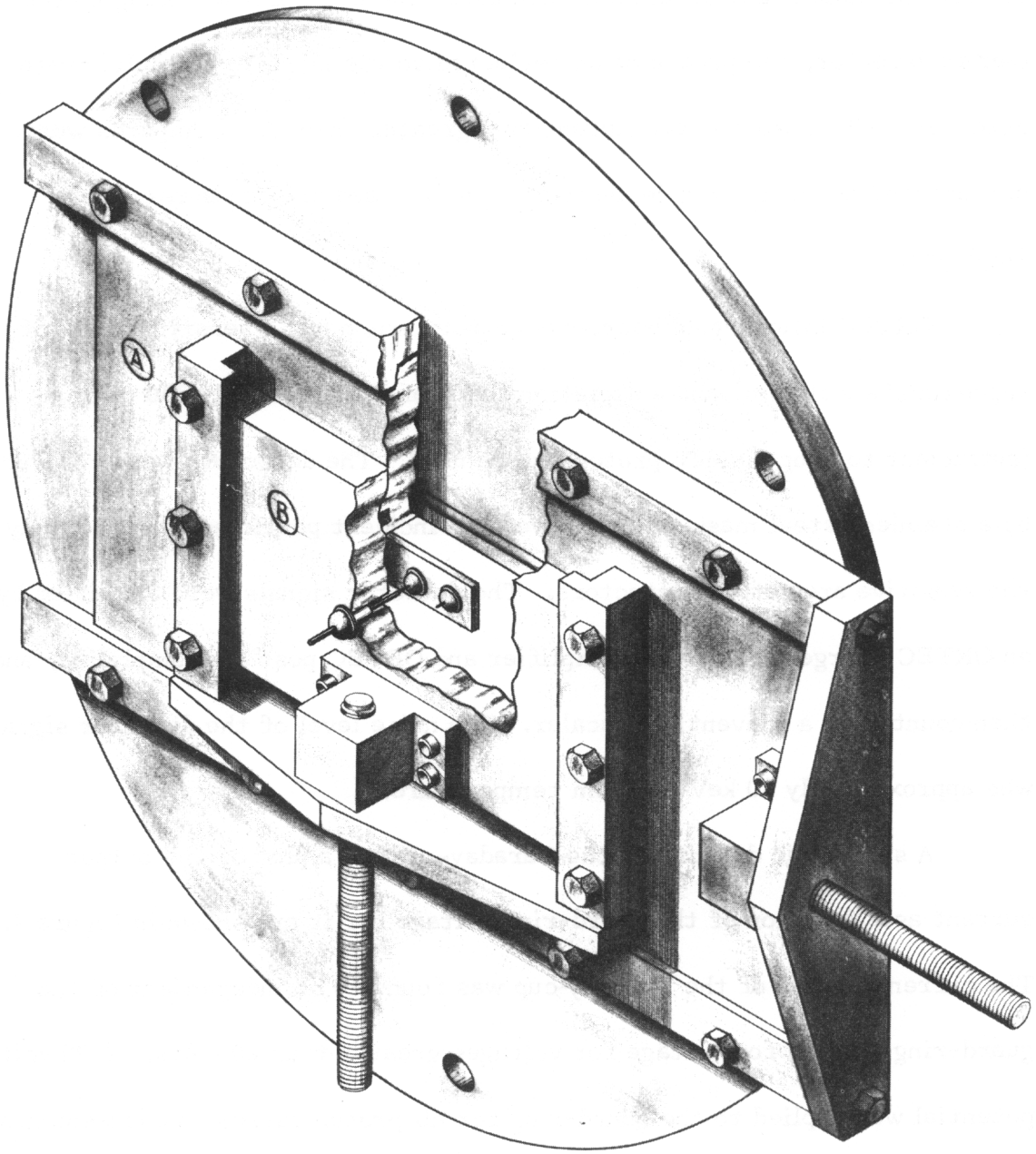

Fig. 3. A cut-away drawing of the detector assembly.

a solid state detector was on the neutral beam axis with a Faraday-cup and solid state detector on opposite sides. For beam intensities of 10^{-16} amperes or less the solid state detectors were used; the neutral beam going to the center detector, the proton beam deflected to the right to the solid state detector. When proton beam intensities greater than 10^{-14} amperes were encountered the beam was deflected to the left and the Faraday-cup was employed.

ORTEC silicon-gold barrier detectors which had a sensitive area of approximately 50 mm^2 and a depletion depth of approximately 330 microns (sufficient to stop 20 MeV protons) were used. The detectors were covered by a stainless steel mask which allowed the incident particles to strike only the sensitive area of the detectors. The detector signals were amplified by an ORTEC charge sensitive preamplifier and ORTEC post bias amplifier, and then counted by a conventional scaler. The noise level of the detector signal was approximately 50 keV at room temperature.

A schematic drawing of the Faraday-cup and a plot of the output current as a function of the guard-ring voltage for it are shown in Figure 4. The current output of the Faraday-cup was found to be independent of the guard-ring voltage for voltage for voltages greater than 20 volts. A 90 volt potential was applied to the guard-ring for all proton current measurements in order to ensure that no loss of secondary-emission electrons occurred. A Keithley Model 410 micro-microammeter was used to measure the cup

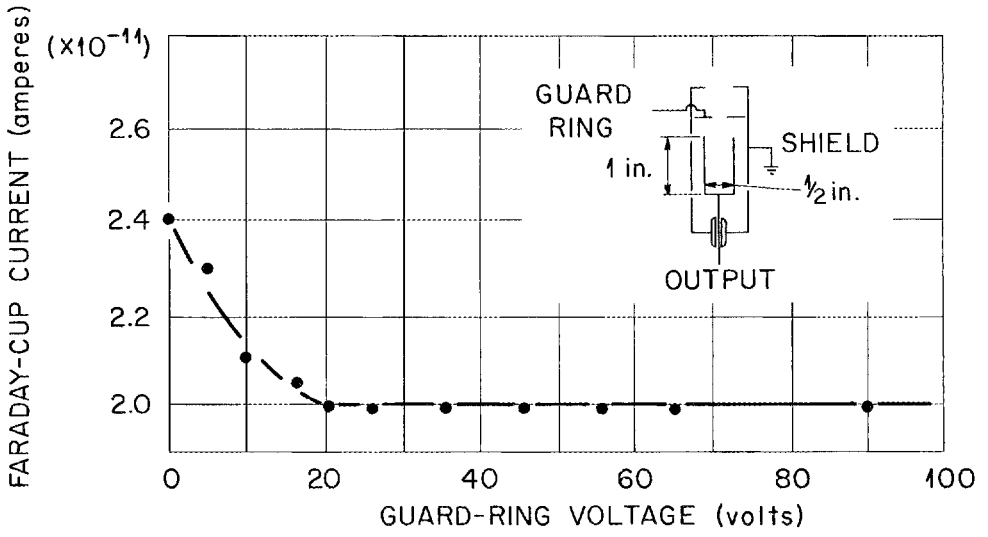

Fig. 4. A schematic drawing of the Faraday-cup and a plot of the output current as a function of guard-ring voltage for it.

current. The Keithley 410 calibration was checked against a Keithley Model 261 picoampere current source. The Keithley 261 has a maximum uncertainty on the most sensitive scale of 1.5%. The output of the micro-microammeter was displayed on a recorder in order to average the current over a given time interval. The accuracy of this averaging process is such that the average current could be determined to less than 10% uncertainty. The time interval was calibrated to within 1% by means of the preset timer and the 60 Hz test signal built into the scaler.

The target gas was introduced into the collision chamber through a Granville-Phillips variable leak valve. The conductance of this valve is continuously variable from 10 cc per second to 10^{-10} cc per second. The leak rate is constant at a given setting (as determined by a counter attached to the driver) such that the differentially pumped collision cell reaches an equilibrium pressure within a few minutes after the leak rate is set. For the highly condensable gases such as water vapor and butane the valve was heated to approximately 80°C in order to minimize the condensation of the gas on the metal to metal sealing surfaces. Any condensation on these surfaces produces a liquid seal which has only "on" or "off" properties.

An Aero-Vac residual gas analyzer was used to spot check the purity of the gases studied. This analyzer had an atomic mass range of 1 to 70 with resolution (fwhm) at mass 20 of one mass unit. Mass scans were made before and after the introduction of the target gas in order to determine if

impurities were present. In no case did impurities appear to amount to as much as 1% of the target gas at the time data were taken.

Of utmost importance in the measurement of cross sections is the accurate determination of target gas densities. This problem has especially hampered the measurement of charge transfer cross sections for condensable gas targets. The pressure measuring device used in this work was a commercially available capacitance manometer. The advantage of this instrument is that it provides continuous pressure monitoring and the pressure determinations are independent of the nature of the gas used. An MKS baratron pressure meter type 77 and pressure head type 77H-1 were purchased from MKS Instruments, Inc. The pressure head has built-in thermostatically regulated heating elements for operation at a constant temperature. These heating elements can also be used to bake-out the pressure head at temperatures near 150°C. The pressure range of the type 77H-1 baratron head is 2×10^{-5} torr to 1.0 torr. The instrument had been factory calibrated to 1 part in 10^4 for the pressure range 0.1 to 1.0 torr. For operation in the pressure range 1×10^{-3} to 1×10^{-4} torr the calibration of the manometer was further checked against a McLeod gage. The results of this comparison, reported in Appendix I, show that the capacitance manometer is in agreement with the McLeod gage, which was used as a standard, to pressures as low as 1×10^{-4} torr. At gas pressures less than 1×10^{-4} torr the uncertainty in reading the McLeod gage as well as

instability in the capacitance manometer result in rather large uncertainties in the pressure readings. In the pressure range at which the measurements of charge transfer cross sections were made (1×10^{-3} to 1×10^{-4} torr) the uncertainties in pressure measurement were approximately 3%.

B. Mathematical Formulation

In order to calculate charge transfer cross sections from experimental data a mathematical description of the charge transfer process must be formulated. Such a description has been presented by Allison[42,43] and will be reviewed here. Consider the charge transfer processes that initially take place when a proton beam interacts with a target tas:

$$H^+ + G \rightarrow H^o + G^+ \tag{14}$$

$$\rightarrow H^- + G^{++} \quad . \tag{15}$$

These beam products, H^o and H^-, may undergo further charge transfer collisions such as:

$$H^o + G \rightarrow H^- + G^+ \tag{16}$$

$$\rightarrow H^+ + G + e \tag{17}$$

$$H^- + G \rightarrow H^o + G + e \tag{18}$$

$$\rightarrow H^+ + G + 2e \tag{19}$$

where G designates any target gas molecule. One may describe these processes mathematically by the following set of differential equations:

$$dF_o = -F_o(\sigma_{01} + \sigma_{0\bar{1}})\, d\pi + F_1 \sigma_{10}\, d\pi + F_{\bar{1}}\sigma_{\bar{1}0}\, d\pi \tag{20}$$

$$dF_1 = -F_1 (\sigma_{10} + \sigma_{1\bar{1}}) d\pi + F_o \sigma_{01} d\pi + F_{\bar{1}} \sigma_{\bar{1}1} d\pi \tag{21}$$

$$dF_{\bar{1}} = -F_{\bar{1}} (\sigma_{\bar{1}0} + \sigma_{\bar{1}1}) d\pi + F_o \sigma_{0\bar{1}} d\pi + F_1 \sigma_{1\bar{1}} d\pi \tag{22}$$

with

$$F_1 + F_o + F_{\bar{1}} = 1 \tag{23}$$

where F_i is the fraction of the total beam in charge state i

σ_{if} is the probability of charge transfer from charge state i to charge state f

π is the number density of the target gas in molecules-cm^{-2} = $N_A \ell P (RT)^{-1}$

P is the target gas pressure in torr

ℓ is the path length through the target gas measured in centimeters

T is the absolute temperature of the target gas

N_A is Avogadro's number

R is the gas constant (8.31×10^7 ergs-mole^{-1}-°C^{-1}) .

General solutions to these equations can be obtained and evaluated for particular experimental conditions. Allison[42] has presented the solutions to Equations (20) through (23) for incident H^+, H^o, and H^- beams. These solutions are complicated by the variety of charge transfer processes which may occur. The problem of charge transfer is greatly simplified by approximations appropriate to the energy range of the present work. For incident H^+ or H^o particles with energies greater than 50 keV the cross

sections for the formation of negative hydrogen ions, σ_{11}^{-} and σ_{01}^{-}, respectively, are very small compared to the cross sections, σ_{10} and σ_{01}. For example, at 100 keV the cross section for H^- formation in an incident H^+ beam is less than 1% of that for H^o formation; likewise, for an incident H^o beam the probability of H^- formation is less than 1% of that for H^+ formation. One may, therefore, neglect the negative hydrogen ion component in either proton or neutral hydrogen beams with less than 1% error when the incident beam energy is 100 keV. At higher energies the probability of H^- formation decreases much faster than the corresponding probabilities for the formation of H^+ and H^{o*}.

When the H^- beam component is neglected in the above set of differential equations the resulting system of equations is

$$dF_o = -F_o\sigma_{01}\,d\pi + F_1\sigma_{10}\,d\pi \tag{24}$$

$$dF_1 = -F_1\sigma_{10}\,d\pi + F_o\sigma_{10}\,d\pi \tag{25}$$

with

$$F_1 + F_o = 1 \quad . \tag{26}$$

The symmetry of these equations should be noted, if the indices 0 and 1 are interchanged the resulting equations are identical. This symmetry implies that any results obtained for F_1 are applicable for F_o when all indices are interchanged. The differential Equations (24) and (25) may be uncoupled by the use of Equation (26) and readily solved by the methods of elementary differential

---

*See section B of Chapter VIII and reference 42.

equations. The general solutions are

$$F_i = F_{i\infty} + P(Z,i) \exp\left[-\pi(\sigma_{10} + \sigma_{01})\right] \tag{27}$$

with i = 0, 1 and

$$F_{o\infty} = \frac{\sigma_{10}}{\sigma_{10} + \sigma_{01}} \qquad F_{1\infty} = \frac{\sigma_{01}}{\sigma_{10} + \sigma_{01}} \tag{28)(29}$$

where Z describes the charge state of the initial beam and i describes the charge state of the beam component under consideration. The quantity $F_{i\infty}$ is an equilibrium fraction, that is, the fraction of the total beam in charge state i under equilibrium (multiple collision) conditions. Values of the parameter P (Z, i), which depend on experimental conditions, are given in Table 1.

The solutions to the two component problem may now be written as they apply to the experimental problem of determining "high-energy" charge transfer cross sections:

for an incident H^o beam

$$F_1 = \frac{\sigma_{01}}{\sigma_{10} + \sigma_{01}} \left\{1 - \exp\left[-\pi(\sigma_{10} + \sigma_{01})\right]\right\} ; \tag{30}$$

for an incident H^+ beam

$$F_o = \frac{\sigma_{10}}{\sigma_{10} + \sigma_{01}} \left\{1 - \exp\left[-\pi(\sigma_{10} + \sigma_{01})\right]\right\} . \tag{31}$$

For "thin" target conditions, conditions in which only single collisions occur as the beam passes through the target, the exponent is very small

$$\pi (\sigma_{10} + \sigma_{01}) << 1 \tag{32}$$

TABLE 1

VALUES OF P(Z, i) FOR THE SOLUTION OF THE TWO COMPONENT EQUATIONS

Initial beam	P(Z, i)	
All neutral	$P(0, 0) = F_{1\infty}$	$P(0, 1) = -F_{1\infty}$
All charged	$P(1, 0) = -F_{0\infty}$	$P(1, 1) = F_{0\infty}$

and one may expand the exponential in a power series. If, after this expansion, only the first terms are retained the two component, "thin" target solutions are given by the following:

for an incident H^o beam

$$F_1 = \sigma_{01} \pi \quad ; \tag{33}$$

for an incident H^+ beam

$$F_o = \sigma_{10} \pi \quad . \tag{34}$$

The quantity π can be written as

$$\pi = \alpha P \text{ mol-cm}^{-2} \tag{35}$$

where

$$\alpha = 9.90 \, \ell(\text{cm}) \, T^{-1} \, (^\circ\text{K}) \times 10^{15} \text{ mol-cm}^{-2}\text{-torr}^{-1} \quad . \tag{36}$$

The quantities ℓ and T in Equation (36) are the collision cell path length and target gas temperature, respectively. The "thin" target solutions, Equations (33) and (34), may now be related directly to the experimental data. For a given collision cell and room temperature, α is a constant; therefore π is only a function of the target gas pressure. Data were obtained for the value of F_f, where f is 1 and 0 in Equations (33) and (34), respectively, for various values of the target gas pressure. From the form of Equations (33) and (34) it is noted that a plot of F_f versus P should result in a straight line with the slope of the line proportional to the cross section σ_{if}. This method of measuring charge transfer cross sections depends on the validity of the two component and "thin" target approximations in giving reliable results. If

$\pi(\sigma_{10} + \sigma_{01})$ is allowed to become as high as 0.20, an error in the measured cross section of approximately 10% will result; thus, either the quantity $\pi(\sigma_{10} + \sigma_{01})$ must be kept very small or appropriate corrections must be made. Approximate corrections for large values of $\pi(\sigma_{10} + \sigma_{01})$ are described in section C of this chapter.

Plots of F_o versus P for protons of various energies in water vapor are shown in Figure 5. It can be seen that even for water vapor, which is a difficult gas to handle, a straight line can be drawn through the experimental points unambiguously. Where possible, the ratio $F_o = I_{H^o}/(I_{H^o} + I_{H^+})$ was not allowed to become larger than 0.05 in order to ensure that the approximation used in obtaining Equations (33) and (34) was valid to within 3%. Since the power series expansion of Equations (30) and (31) results in an alternating harmonic series, neglecting the terms of order greater than n results in an error less than the $(n + 1)^{st}$ term.[44] The cross sections were calculated from the slope of each straight line by the relationship

$$\sigma_{01} = \frac{\text{slope}}{\alpha} \tag{37}$$

where α is given by Equation (36). These results and the results for other target gases are presented later.

Equations (28) and (29) may be used as a convenient check on the measured cross sections. The quantities $F_{1\infty}$ and $F_{o\infty}$ may be measured directly by simply increasing the gas pressure until equilibrium conditions (multiple collisions) occur for incident H^o and H^+ beams, respectively.

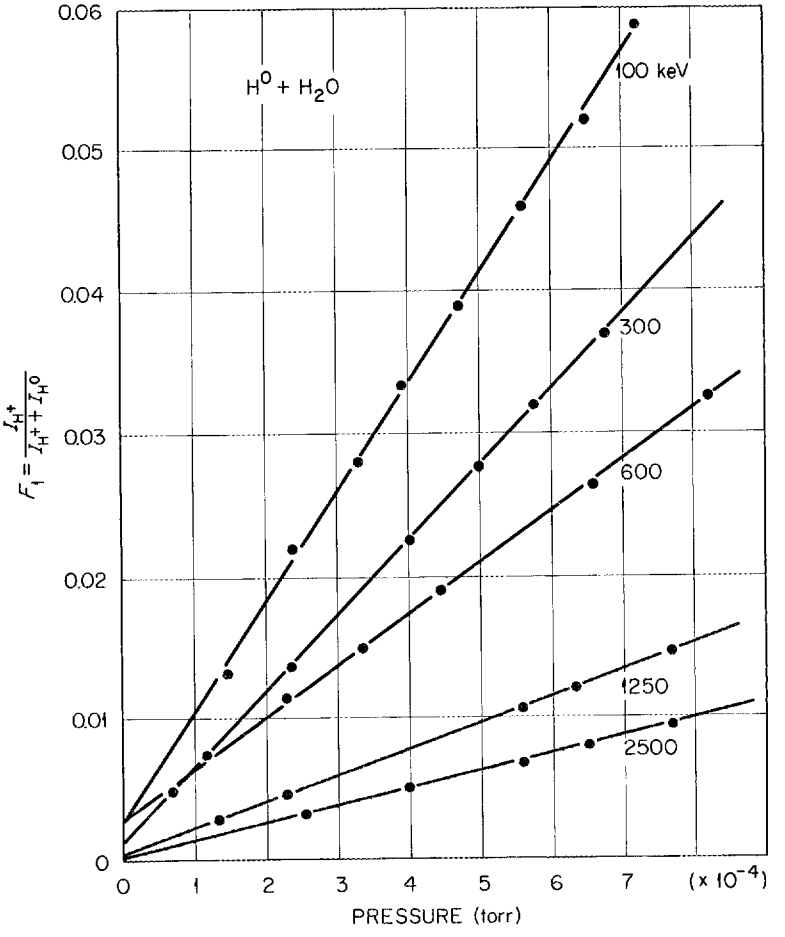

Fig. 5. An example of the growth of the charge-changed component in an initially pure beam with increased target density.

These values may then be compared to the measured cross sections by the relationship

$$\frac{F_{1\infty}}{F_{0\infty}} = \frac{\sigma_{01}}{\sigma_{10}} \tag{38}$$

and an estimation of the internal consistency of the measurements can be determined. At energies above a few hundred kilovolts the value of F_1 becomes very nearly equal to one ($F_{0\infty} = 1 - F_{1\infty}$) and accurate experimental values of the equilibrium fractions are difficult to obtain by direct measurement.

C. Experimental Procedure and Data Analysis

The apparatus used to obtain the data to which Equations (33) and (34) were applied is described in section A of this chapter. For measurements of cross sections for neutral beams the incident proton beam underwent charge-changing collisions with either nitrogen or argon gas introduced into the first gas cell at a pressure of approximately one micron. A minimum amount of beam scattering occurred at this gas pressure while a neutral beam component of the desired intensity was produced. Following the first collision cell the charged components were deflected from the beam by an electric field leaving a pure neutral beam incident on the target gas cell. For measurements where a pure proton beam was necessary the first collision cell was evacuated to approximately 2×10^{-8} torr and the first set of electrostatic deflection plates

was electrically grounded. After having passed through the target chamber the beam components were separated by an electric field and their intensities were determined. From these measurements and a knowledge of the target gas pressure the plots of $F_o(F_1)$ versus P described earlier were made and the cross sections $\sigma_{10}(\sigma_{01})$ calculated.

For the measurement of very small electron capture cross sections the neutral component in the proton beam due to interactions with residual gas molecules in the beam tube becomes comparable to the neutral component formed by interactions with the target molecules. In order to reduce this neutral background a slight modification was made to the charge transfer apparatus. A small bend (approximately 1° with respect to the incident beam axis) was introduced after the first two apertures. The proton beam could then be bent by the first set of electrostatic deflection plates into the 0.020 inch diameter entrance aperture of the target gas cell; whereas the neutral beam would continue in a straight line unable to enter the target cell. Electron capture cross sections for protons on hydrogen and helium were measured by means of the apparatus containing the bend for incident proton energies greater than 600 keV. With the reduced background the electron capture cross sections for hydrogen and helium targets could be measured to 1.75 and 2.00 MeV, respectively, before the signal-to-noise ratio was too small for meaningful results to be obtained. Cross sections for other gas targets are much larger and could be measured without the bend placed in the apparatus.

Calculation of the charge transfer cross sections from the actual experimental data is seen most clearly when the mathematical equations describing the process are written in the following form:

$$\sigma_{10} = \frac{1}{\alpha}\left(\frac{I_{H^o}}{I_{H^o} + I_{H^+}}\right)\frac{1}{P} \tag{39}$$

$$\sigma_{01} = \frac{1}{\alpha}\left(\frac{I_{H^+}}{I_{H^o} + I_{H^+}}\right)\frac{1}{P} \tag{40}$$

These equations are Equations (33) and (34) rewritten in terms of the measured quantities. I_{H^+} and I_{H^o} are the proton and neutral beam intensities, P is the target gas pressure and α is given by Equation (36). In this section the methods of obtaining the parameters in Equations (36), (39), and (40) will be described.

The temperature referred to in Equation (36) is the target gas temperature in degrees Kelvin. Since the target gas pressures were quite low (the mean free path of a target molecule was greater than the dimensions of the gas chamber), the gas temperature was taken to be that of the walls of the collision chamber. The wall temperature was measured by means of an iron-constantan thermocouple to within $\pm$ 2°C. Two different collision cells were used in this work which result in two different values of ℓ in Equation (36). The first data were obtained by means of a collision cell of

length $\ell = 17.50 \pm 0.06$ inches. In order to check the reproducibility of the measured cross sections, a shorter collision cell was installed. The short cell was 3.06 ± 0.06 inches in length. The two different cell lengths were also used in estimating the effective increase in the path length due to a pressure gradient outside of the collision cell apertures which results from differential pumping. Since the same size entrance and exit apertures were used for both collision cells the effective path length increase should be the same; however the percentage increase in path length is quite different. An increase in path length of one centimeter corresponds to an increase of 13% for the short cell and only 2% for the long cell. A comparison of cross section measurements made with the two collision cells shows that the cross section values obtained by means of the short cell were approximately 3% greater than those obtained by means of the long cell. This increase of 3% is in close agreement with a simple calculation which gives the effective increase in cell length to be 2.7% for the short cell and less than 0.5% for the long cell (see Appendix II). The use of the short cell is advantageous in that higher gas pressures could be used before secondary collisions occur. The gas pressures of less than 3×10^{-4} torr necessary to ensure single collisions for some target gases when the long cell was used were extremely difficult to measure accurately.

The measurement of target gas pressures was made by means of a capacitance manometer. This device has been described in section A of

this chapter and the accuracy is considered in Appendix I. Upon introduction of the target gas into the collision chamber, the pressure was found to reach an equilibrium value in a few minutes. For the highly condensable gases such as water vapor and butane, it was necessary to wait a few minutes more to reach pressure equilibrium. At no time was the pressure allowed to drift more than a few percent during a data collection period. In most cases the drift was negligible.

Precautions were taken to ensure that no impurities were introduced into the target gas as it was transferred from the supply cylinder (the initial gas purities are discussed in Chapter V) to the collision cell. The copper line connecting the supply to the collision cell was first evacuated to 10^{-3} torr. While evacuated the line was heated by a torch flame in order to remove any adsorbed gases. The valve between the line and fore pump was then closed and gas from the supply cylinder introduced at a pressure of approximately 20 lbs-in.$^{-2}$ above atmospheric pressure except for water vapor which was introduced at its equilibrium vapor pressure. A cold trap between the collision cell and gas supply was filled with liquid nitrogen for the target gases H_2 and He while a dry ice slurry was used for all other gases except H_2O, C_4H_{10}, and Kr. The dry ice slurry was made by mixing crushed dry ice with either acetone or butyl cellosolve (a mixture of ethylene glycol and mono-butyl ether). For butane and krypton the trap was left at room temperature since they will condense at dry ice temperature, and for water vapor the transfer line was

heated to approximately 50°C to ensure that no condensation would occur. The valve through which gas was introduced into the collision chamber was heated at all times to reduce the possibility of gas condensation on the sealing surfaces.

The accuracy of the measured cross sections can be seen in Equations (39) and (40) to depend directly on the accuracy of the beam intensity determinations. The entire beam which enters the collision chamber must be detected in terms of its charge state components at the detectors. One possible cause of a systematic error in the cross section measurements is due to scattering of the incident particles during charge transfer processes. If the deflection of the incident particle is sufficient during charge transfer, the charge-changed component of the beam may strike the walls of the exit aperture and be preferentially removed from the beam. A rough estimate of the maximum scattering angle which may occur during charge transfer can be obtained from a classical picture in which an electron is stripped from the projectile.[43] The maximum scattering angle obtained in this estimate is 2m/M where m is the electron mass and M is the proton mass. Scattering at this angle would cause a maximum beam spread at the exit aperture due to single collisions of 0.036 inches for the long cell and 0.006 inches for the short cell. In the present work the exit aperture was large enough (0.062 inches in diameter) relative to the entrance aperture (0.020 inches in diameter) to ensure that scatter during the charge transfer process did not

cause the interacting beam particles to strike the aperture walls.

A second possible cause of a systematic error in the determination of the ratio of charge state components within the beam is separation of the components of the beam by external electric or magnetic fields. If charge separation occurs, one of the charge states may be preferentially removed from the beam by striking the edge of the exit aperture. The external magnetic field was monitored and a maximum field strength of 1.3 Gauss was measured. This magnetic field could deflect a 100 keV beam of protons approximately 0.020 inches with the deflection decreasing at higher energies. A deflection as high as 0.025 inches could be tolerated if extreme care was taken in the alignment procedure. For the data taken with the short cell the alignment was checked each time the energy was changed, whereas periodic alignment checks were made when the long collision cell was used. The collision chamber was electrostatically shielded by the stainless steel walls so that electrostatic deflection of the beam within the collision cell was minimized. Since the effects of beam deflection within the collision cell due to stray fields would be more pronounced for the long cell than the short cell, the fact that the results obtained with both cells were in close agreement at all energies is quantitative evidence that charge separation did not occur.

Once the beam had passed through the collision cell, the center detector was centered with respect to the beam. In order to ensure total

beam collection it is important that the detector area be large relative to the beam diameter. The beam dimensions and profile were determined by scanning with the movable detector. Due to uncertainties in the knowledge of the exact position of the detectors, only rough estimates of the beam size could be made; however an upper limit on the beam diameter was placed at 0.050 inches. The beam profile was flat on top with rapidly decreasing intensity on either side. Since the sensitive area of each detector was 0.300 inches in diameter, 100% beam detection could be expected when the beam was properly centered. When the center detector had been centered on the beam with respect to both the vertical and horizontal directions a potential was applied to the deflection plates to deflect the protons to the side detector. The protons were centered on the side detector by proper deflection potentials, then the beams were scanned by the detectors to determine if both beams were simultaneously centered on their respective detectors. This procedure was carried out each time the energy was changed or the alignment checked.

For large cross sections where the proton and atomic hydrogen components of the beam differ by a factor of approximately 10^3 the two components were detected on respective solid state detectors. In this way the relative intensities were determined simultaneously and any fluctuations in the incident beam were automatically compensated. The counters were started and stopped by a common switch to reduce possible errors in this

procedure. Sufficient data were accumulated to obtain counting statistics of less than one percent for the less intense of the two charge state components. Since it is possible that a malfunction of the electronics could result in a systematic error in the ratio of beam components, the leads from the detectors to the amplification-scaling systems were interchanged periodically. The detectors were also interchanged with respect to the beam components at various times. These interchanges had no effect on the value of the cross sections determined from the data.

For small cross sections, such as the electron capture cross sections at energies of more than a few hundred kilovolts, the number of neutral particles produced when the proton beam interacted with the target was very small. In order to obtain reliable statistics for the neutral component the proton beam had to be quite intense. A Faraday-cup was used to measure these proton beam intensities which were in the range of 2×10^{-13} to 5×10^{-10} amperes. Since single particle counting was still necessary for the neutral beam component the counts per minute neutral intensity had to be converted to equivalent current for comparison to the proton current. The conversion to equivalent current was accomplished by counting neutral particles for a given period of time while simultaneously recording the proton current on a chart recorder. The neutral particle intensity in particles per unit time could then be converted to equivalent current and compared to the average proton current. The unit of counting time was determined by a preset timer

which was calibrated to less than 2% uncertainty by means of a 60 Hz signal generator built into the scaler.

For given experimental conditions of path length ℓ, temperature T, incident beam H^i (i = 0 or +) and incident beam energy E, several different values of the intensity ratio $I_{H^i}/(I_{H^0} + I_{H^+})$ were obtained for corresponding target gas pressures. A plot of $I_{H^i}/(I_{H^0} + I_{H^+})$ versus P results in a straight line (under "thin" target conditions) and the charge transfer cross section is proportional to the slope. The line does not pass through the origin due to charge-changed beam components which are independent of the target gas density and form a small percentage of the incident beam intensity. These background charge components are due primarily to charge transfer between the incident beam and residual gas molecules within the vacuum system and charge transfer in collisions between the beam and the defining apertures. This background was reduced in several ways, (1) the use of ultra-high vacuum techniques to reduce the residual gas molecule density, (2) the reduction of path length between the charge analyzing system and the collision cell, (3) the use of knife-edge apertures, and (4) careful alignment of the apertures. The major effect of a small background component is a nonzero intercept which will not affect the cross section determination. However, for target gases with very small cross sections the background component may become comparable to the charge component produced by interactions between the beam and the target gas, in which case the ability

to measure the cross sections is affected. The accuracy of the electron capture cross sections for hydrogen and helium was limited by this "signal" to noise ratio.

Equations (39) and (40) were obtained by an approximation of a power series expansion. The approximation, which was a result of "thin" target conditions defined by Equation (32), had the following form:

$$1 - \exp\left[-\alpha P(\sigma_{01} + \sigma_{10})\right] \cong \alpha P(\sigma_{01} + \sigma_{10}) \quad . \tag{41}$$

As the value of the exponent, $\alpha P(\sigma_{10} + \sigma_{01})$, becomes large, the approximation indicated by Equation (41) is no longer valid. An estimation of the correction needed to account for the error in Equation (41) at large values of $\alpha P(\sigma_{10} + \sigma_{01})$ is given by the ratio

$$\frac{\alpha P(\sigma_{10} + \sigma_{01})}{1 - \exp\left[-\alpha P(\sigma_{10} + \sigma_{01})\right]} \tag{42}$$

At incident particle energies greater than 100 keV, $\sigma_{01} >> \sigma_{10}$; therefore $\alpha P(\sigma_{10} + \sigma_{01}) \cong \alpha P\sigma_{01}$. The quantity $\alpha P\sigma_{01}$ is given approximately by Equation (40) to be the measured quantity $I_{H^+}/(I_{H^+} + I_{H^o})$ for an incident H^o beam and a given target pressure. Each fraction $I_{H^+}/(I_{H^+} + I_{H^o})$ must be multiplied by the correction factor given by Equation (42) before that fraction is plotted versus pressure. This correction allows one to apply Equation (39) to the plotted data and obtain a cross section from the slope which is effectively corrected to second order terms in the power series expansion. This correction was applied initially to the data for approximately

50 cross section measurements. The cross sections determined from the corrected data were then compared to the uncorrected results. A plot of the ratio (σ_{01} corrected)/(σ_{01} uncorrected) versus the maximum value of the fraction $I_{H^o}/(I_{H^o} + I_{H^+})$ allowed in determining the slope from which the cross sections were calculated is shown in Figure 6. From this graph correction factors for other cross sections could be determined to within $\pm$ 2% by a knowledge of the maximum value of the ratio $I_{H^o}/(I_{H^o} + I_{H^+})$ used in the slope determination. Due to the symmetry of Equations (39) and (40) the same correction must be made for σ_{10} has been described above for σ_{01} when equivalent target gas densities are used in the measurement. This is quite clear when the second order terms are observed in the power series expansion as is shown in Equations (43) and (44).

$$\frac{I_{H^+}}{I_{H^+} + I_{H^o}} = \alpha P \sigma_{01} [1 - \tfrac{1}{2}\alpha P(\sigma_{10} + \sigma_{01})] \tag{43}$$

$$\frac{I_{H^o}}{I_{H^+} + I_{H^o}} = \alpha P \sigma_{10} [1 - \tfrac{1}{2}\alpha P(\sigma_{10} + \sigma_{01})] \tag{44}$$

The correction to the cross sections to account for small deviations from the validity of approximation (41) were made only for the measurements obtained by means of the long path length collision cell. When the short path length collision cell was used the value of $\alpha P(\sigma_{10} + \sigma_{01})$ was not allowed to reach a value greater than 0.05. At $\alpha P(\sigma_{10} + \sigma_{01}) = 0.05$ Equation (41) is accurate to within 3%.

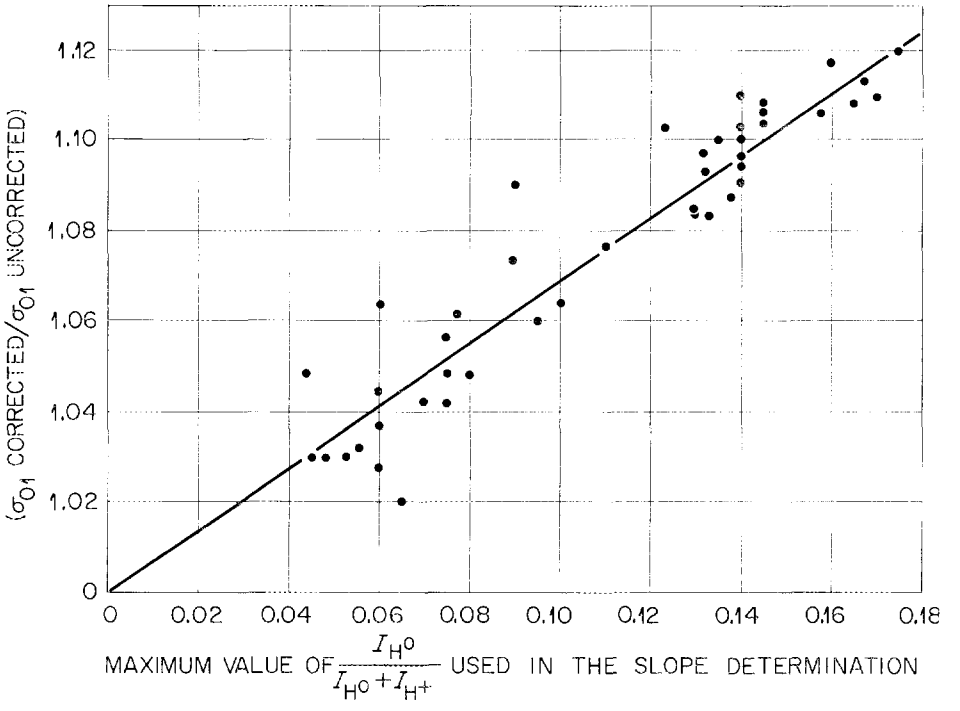

Fig. 6. The ratio of the electron loss cross sections which have been corrected for secondary collisions to the uncorrected values as a function of the maximum value of F_1 allowed in determining the slope from which the cross sections were calculated.

CHAPTER IV

EXPERIMENTAL RESULTS AND DISCUSSION

For incident particle energies greater than 600 keV the cross section values reported in Table 2, except for the electron capture cross sections for hydrogen and helium targets, were measured by means of the collision cell of 17.50 ± 0.06 inches in length. The electron capture cross sections for hydrogen and helium, and spot checks of both electron capture and electron loss cross sections for other targets, were measured with the short collision cell. A bend was placed in the apparatus immediately preceding the short collision cell for electron capture measurements in order to reduce the neutral particle background. There was some doubt as to the precise path length of the gas cell during the measurements with the short cell. This uncertainty in the path length resulted when the end plate of the collision cell slipped and increased the path length by approximately $\frac{1}{2}$ inch. Since the end plate is within the vacuum system, the fact that it had slipped was not discovered until the vacuum system was disassembled following the cross section measurements. The path length was measured after the system was disassembled and this length was used in the calculation of the cross sections from these data. The cross sections determined in this way were in agreement with the measurements made by means of the long cell to within approximately $\pm$ 10%.

TABLE 2

SINGLE-ELECTRON CAPTURE AND LOSS CROSS SECTIONS

σ_{01}	Cross section per molecule			
Energy (keV)	Target gas			
	H_2	He	Ar	Kr
100	1.09×10^{-16}	8.52×10^{-17}	4.59×10^{-16}	4.22×10^{-16}
200	7.14×10^{-17}	5.38×10^{-17}	3.47×10^{-16}	3.75×10^{-16}
300	5.18×10^{-17}	4.15×10^{-17}	2.97×10^{-16}	3.41×10^{-16}
400	4.11×10^{-17}	3.27×10^{-17}	2.57×10^{-16}	3.25×10^{-16}
550	3.10×10^{-17}	2.44×10^{-17}	2.19×10^{-16}	2.80×10^{-16}
800	2.31×10^{-17}	1.82×10^{-17}	1.70×10^{-16}	2.03×10^{-16}
1000	1.97×10^{-17}	1.52×10^{-17}	1.84×10^{-16}	1.93×10^{-16}
1250	1.63×10^{-17}	1.25×10^{-18}	1.49×10^{-16}	1.72×10^{-16}
1500	1.34×10^{-17}	9.99×10^{-18}	1.24×10^{-16}	1.64×10^{-16}
1750	1.19×10^{-17}	9.06×10^{-18}	1.22×10^{-16}	1.60×10^{-16}
2000	1.05×10^{-17}	7.94×10^{-18}	1.10×10^{-16}	1.46×10^{-16}
2250		7.20×10^{-18}	9.98×10^{-17}	1.31×10^{-16}
2500	8.20×10^{-18}	6.31×10^{-18}	8.93×10^{-17}	1.32×10^{-16}
σ_{10}				
100	2.86×10^{-17}	2.98×10^{-17}	8.54×10^{-17}	1.02×10^{-16}
*200			8.04×10^{-18}	8.62×10^{-18}
300	2.42×10^{-19}	8.17×10^{-19}	1.59×10^{-18}	2.01×10^{-18}
*400			5.96×10^{-19}	1.38×10^{-18}
550	1.11×10^{-20}	6.41×10^{-20}	3.50×10^{-19}	8.82×10^{-19}
800	1.56×10^{-21}	1.17×10^{-20}	1.52×10^{-19}	3.76×10^{-19}
1000	4.74×10^{-22}	3.87×10^{-21}	8.99×10^{-20}	2.34×10^{-19}
1250	1.25×10^{-22}	1.17×10^{-21}	5.08×10^{-20}	1.31×10^{-19}
1500	5.18×10^{-23}	5.26×10^{-22}	3.25×10^{-20}	7.29×10^{-20}
1750	1.69×10^{-23}	2.15×10^{-22}	1.96×10^{-20}	4.16×10^{-20}
2000		1.17×10^{-22}	1.32×10^{-20}	2.70×10^{-20}
2250			8.02×10^{-21}	1.70×10^{-20}
2500			5.50×10^{-21}	1.13×10^{-20}

*Calculated by means of measured equilibrium fractions and measured σ_{01}

TABLE 2 (cont.)

σ_{01}	Cross section per molecule			
Energy (keV)	Target gas			
	O_2	N_2	CO	CO_2
100	3.91×10^{-16}	4.47×10^{-16}	4.60×10^{-16}	5.85×10^{-16}
200	3.55×10^{-16}	3.89×10^{-16}	3.60×10^{-16}	4.69×10^{-16}
300	3.00×10^{-16}	3.07×10^{-16}	3.25×10^{-16}	4.28×10^{-16}
400	2.59×10^{-16}	2.53×10^{-16}	2.63×10^{-16}	3.72×10^{-16}
550	2.28×10^{-16}	2.22×10^{-16}	2.32×10^{-16}	3.27×10^{-16}
800	1.74×10^{-16}	1.79×10^{-16}	1.63×10^{-16}	2.44×10^{-16}
1000	1.56×10^{-16}	1.57×10^{-16}	1.47×10^{-16}	2.17×10^{-16}
1250	1.32×10^{-16}	1.34×10^{-16}	1.27×10^{-16}	1.91×10^{-16}
1500	1.24×10^{-16}	1.07×10^{-16}	1.10×10^{-16}	1.69×10^{-16}
1750	1.13×10^{-16}	1.01×10^{-16}	1.02×10^{-16}	1.51×10^{-16}
2000	1.01×10^{-16}	9.16×10^{-17}	9.10×10^{-17}	1.33×10^{-16}
2250	8.94×10^{-17}	8.44×10^{-17}	8.51×10^{-17}	1.22×10^{-16}
2500	8.34×10^{-17}	7.79×10^{-17}	7.94×10^{-17}	1.11×10^{-16}
σ_{10}				
100	9.80×10^{-17}	9.00×10^{-17}	1.01×10^{-16}	1.51×10^{-16}
*200	1.78×10^{-17}	1.54×10^{-17}	1.50×10^{-17}	2.26×10^{-17}
300	5.01×10^{-18}	3.42×10^{-18}	4.33×10^{-18}	6.41×10^{-18}
*400	1.56×10^{-18}	1.09×10^{-18}	1.10×10^{-18}	2.25×10^{-18}
550	5.50×10^{-19}	4.30×10^{-19}	4.92×10^{-19}	7.50×10^{-19}
800	1.33×10^{-19}	1.18×10^{-19}	1.25×10^{-19}	1.93×10^{-19}
1000	6.85×10^{-20}	5.77×10^{-20}	6.65×10^{-20}	8.97×10^{-20}
1250	3.18×10^{-20}	3.20×10^{-20}	3.58×10^{-20}	5.14×10^{-20}
1500	1.94×10^{-20}	1.71×10^{-20}	1.70×10^{-20}	2.41×10^{-20}
1750	1.07×10^{-20}	1.02×10^{-20}	1.05×10^{-20}	1.53×10^{-20}
2000	6.97×10^{-21}	6.90×10^{-21}	5.35×10^{-21}	9.73×10^{-21}
2250	4.25×10^{-21}	4.40×10^{-21}	4.29×10^{-21}	6.63×10^{-21}
2500	3.55×10^{-21}	2.95×10^{-21}	3.01×10^{-21}	3.62×10^{-21}

*Calculated by means of measured equilibrium fractions and measured σ_{01}

TABLE 2 (cont.)

σ_{01}	Cross section per molecule			
Energy (keV)	Target gas			
	H_2O	CH_4	C_2H_4	C_2H_6
100	3.18×10^{-16}	4.22×10^{-16}	5.63×10^{-16}	6.57×10^{-16}
200	2.70×10^{-16}	3.00×10^{-16}		4.98×10^{-16}
300	2.10×10^{-16}	2.52×10^{-16}	3.73×10^{-16}	4.14×10^{-16}
400		1.90×10^{-16}		3.21×10^{-16}
550	1.45×10^{-16}	1.69×10^{-16}	2.54×10^{-16}	2.85×10^{-16}
800	1.12×10^{-16}	1.32×10^{-16}	2.00×10^{-16}	2.12×10^{-16}
1000	9.81×10^{-17}	1.05×10^{-16}	1.68×10^{-16}	1.78×10^{-16}
1250	8.02×10^{-17}	8.38×10^{-17}	1.46×10^{-16}	1.49×10^{-16}
1500	6.82×10^{-17}	7.60×10^{-17}	1.28×10^{-16}	1.35×10^{-16}
1750	6.07×10^{-17}	6.67×10^{-17}	1.09×10^{-16}	1.21×10^{-16}
2000	5.67×10^{-17}	5.95×10^{-17}	9.78×10^{-17}	1.03×10^{-16}
2250	5.11×10^{-17}	5.48×10^{-17}	8.71×10^{-17}	9.65×10^{-17}
2500	4.91×10^{-17}	4.96×10^{-17}	7.39×10^{-17}	8.68×10^{-17}
σ_{10}				
100	9.60×10^{-17}	1.08×10^{-16}	1.47×10^{-16}	1.75×10^{-16}
*200	1.01×10^{-17}	8.00×10^{-18}		1.43×10^{-17}
300	3.06×10^{-18}	1.87×10^{-18}	2.46×10^{-18}	3.00×10^{-18}
*400	9.70×10^{-19}	4.47×10^{-19}		6.43×10^{-19}
550	3.15×10^{-19}	2.00×10^{-19}	3.45×10^{-19}	3.40×10^{-19}
800	6.80×10^{-20}	6.11×10^{-20}	1.20×10^{-19}	1.01×10^{-19}
1000	2.81×10^{-20}	3.11×10^{-20}	5.96×10^{-20}	6.01×10^{-20}
1250	1.69×10^{-20}	1.43×10^{-20}	3.60×10^{-20}	3.05×10^{-20}
1500	9.05×10^{-21}	8.07×10^{-21}	1.87×10^{-20}	1.70×10^{-20}
1750	5.21×10^{-21}	5.05×10^{-21}	1.16×10^{-20}	9.29×10^{-21}
2000	3.25×10^{-21}	3.19×10^{-21}	5.96×10^{-21}	5.93×10^{-21}
2250	2.15×10^{-21}	1.93×10^{-21}	4.04×10^{-21}	3.57×10^{-21}
2500	1.65×10^{-21}	1.16×10^{-21}	2.73×10^{-21}	2.22×10^{-21}

*Calculated by means of measured equilibrium fractions and measured σ_{01}

TABLE 2 (cont.)

σ_{01}	Cross section per molecule
Energy (keV)	Target gas
	C_4H_{10}
100	9.69×10^{-16}
200	
300	6.62×10^{-16}
400	
550	4.64×10^{-16}
800	3.76×10^{-16}
1000	3.17×10^{-16}
1250	2.80×10^{-16}
1500	2.42×10^{-16}
1750	2.13×10^{-16}
2000	1.98×10^{-16}
2250	1.73×10^{-16}
2500	1.60×10^{-16}
σ_{10}	
100	2.50×10^{-16}
*200	
300	5.41×10^{-18}
*400	
550	6.21×10^{-19}
800	2.43×10^{-19}
1000	1.06×10^{-19}
1250	6.05×10^{-20}
1500	3.30×10^{-20}
1750	1.98×10^{-20}
2000	1.23×10^{-20}
2250	6.70×10^{-21}
2500	5.56×10^{-21}

*Calculated by means of measured equilibrium fractions and measured σ_{01}

For incident particle energies less than 600 keV only the electron loss cross sections were measured by means of the long collision cell. The short cell, 3.06 inches in length, was used to measure both the electron capture and electron loss cross sections at energies of 100, 300, and 550 keV. For these measurements the length of the short collision cell was accurately known. Where measurements were made with both collision cells the average value is given in Table 2. The agreement between the two measurements was of the order of $\pm$ 6 to 8%.

The uncertainties associated with the cross section measurements are evaluated in Chapter V with the result that uncertainties of $\pm$6% and $\pm$8% are assigned to the measured values of σ_{01} and σ_{10}, respectively. These uncertainties include possible errors in the absolute values as well as relative values.

The ratio of charge state components was also measured under multiple collision conditions by simply increasing the target gas pressure until an equilibrium condition existed between the neutral and charged components of the beam. A comparison of these measured equilibrium fractions and the corresponding fractions calculated from the measured charge transfer cross sections [see Equations (28) and (29)] is a convenient check of the internal consistency of the experimental results. The equilibrium fractions determined in these two ways are compared in Table 3. There is good agreement between the equilibrium fractions measured in these two ways demonstrating the internal consistency of the experiment.

TABLE 3

COMPARISON OF MEASURED AND CALCULATED EQUILIBRIUM FRACTIONS[†]

Proton Energy (keV)	Target Gas					
	H_2		He		Ar	
	$F_{o\infty}$		$F_{o\infty}$		$F_{o\infty}$	
	Meas.	Calc.[*]	Meas.	Calc.[*]	Meas.	Calc.[*]
100	1.4×10^{-1}	2.1×10^{-1}	2.3×10^{-1}	2.6×10^{-1}	1.4×10^{-1}	1.6×10^{-1}
200	2.0×10^{-2}		5.8×10^{-2}		2.2×10^{-2}	
300	4.0×10^{-3}	4.7×10^{-3}	1.9×10^{-2}	1.9×10^{-2}	5.3×10^{-3}	5.3×10^{-3}
400	1.0×10^{-3}		8.0×10^{-3}		2.3×10^{-3}	
550	6.0×10^{-4}	3.6×10^{-4}	2.6×10^{-3}	2.6×10^{-3}		1.6×10^{-3}
800					8.8×10^{-4}	9.3×10^{-4}
1000					6.4×10^{-4}	4.9×10^{-4}
1250					4.0×10^{-4}	3.4×10^{-4}
1500					3.6×10^{-4}	2.6×10^{-4}
1750					1.5×10^{-4}	1.6×10^{-4}

[†] $F_{1\infty}$ and $F_{o\infty}$ are related by $F_{1\infty} + F_{o\infty} = 1$

[*] $F_{o\infty}\,(\text{calc}) = \dfrac{\sigma_{10}}{\sigma_{01} + \sigma_{10}}$

TABLE 3 (cont.)

Proton Energy (keV)	Target Gas					
	Kr		O_2		N_2	
	$F_{O\infty}$		$F_{O\infty}$		$F_{O\infty}$	
	Meas.	Calc.*	Meas.	Calc.*	Meas.	Calc.*
100	1.9×10^{-1}	2.0×10^{-1}	2.0×10^{-1}	2.0×10^{-1}	1.8×10^{-1}	1.7×10^{-1}
200	2.1×10^{-2}		5.0×10^{-2}		3.8×10^{-2}	
300	6.0×10^{-3}	5.9×10^{-3}	1.8×10^{-2}	1.6×10^{-2}	1.1×10^{-2}	1.1×10^{-2}
400	4.8×10^{-3}		6.0×10^{-3}		4.0×10^{-3}	
550	3.2×10^{-3}	3.1×10^{-3}	3.0×10^{-3}	2.4×10^{-3}	2.0×10^{-3}	1.9×10^{-3}
800			6.5×10^{-4}	7.6×10^{-4}	6.2×10^{-4}	6.6×10^{-4}
1000			3.6×10^{-4}	4.4×10^{-4}	3.5×10^{-4}	3.7×10^{-4}
1250			2.0×10^{-4}	2.4×10^{-4}	2.0×10^{-4}	2.3×10^{-4}
1500			1.4×10^{-4}	1.6×10^{-4}	1.6×10^{-4}	1.6×10^{-4}
1750			1.1×10^{-4}	0.9×10^{-4}	0.9×10^{-4}	1.0×10^{-4}
2000			6.9×10^{-5}	6.9×10^{-5}		
2250			5.3×10^{-5}	4.8×10^{-5}		
2500			3.9×10^{-5}	4.2×10^{-5}		

*$F_{O\infty}$ (calc) = $\dfrac{\sigma_{10}}{\sigma_{01} + \sigma_{10}}$

TABLE 3 (cont.)

Proton Energy (keV)	Target Gas					
	CO		CO_2		H_2O	
	$F_{o\infty}$		$F_{o\infty}$		$F_{o\infty}$	
	Meas.	Calc.*	Meas.	Calc.*	Meas.	Calc.*
100	1.7×10^{-1}	1.8×10^{-1}	2.0×10^{-1}	2.1×10^{-1}	1.7×10^{-1}	2.3×10^{-1}
200	3.6×10^{-2}		4.6×10^{-2}		3.6×10^{-2}	
300	1.1×10^{-2}	1.3×10^{-2}	1.5×10^{-2}	1.5×10^{-2}	1.2×10^{-2}	1.4×10^{-2}
400	4.0×10^{-3}		6.0×10^{-3}		4.0×10^{-3}	
550	2.0×10^{-3}	2.1×10^{-3}	2.2×10^{-3}	2.3×10^{-3}	1.4×10^{-3}	2.2×10^{-3}
800	6.0×10^{-4}	7.7×10^{-4}	6.2×10^{-4}	7.9×10^{-4}	6.0×10^{-4}	6.0×10^{-4}
1000	4.0×10^{-4}	4.5×10^{-4}	4.0×10^{-4}	4.1×10^{-4}	3.0×10^{-4}	2.9×10^{-4}
1250	1.9×10^{-4}	2.8×10^{-4}	2.0×10^{-4}	2.7×10^{-4}	2.0×10^{-4}	2.1×10^{-4}
1500	1.6×10^{-4}	1.5×10^{-4}	1.3×10^{-4}	1.4×10^{-4}	1.3×10^{-4}	1.3×10^{-4}
1750			1.0×10^{-4}	1.0×10^{-4}	8.0×10^{-5}	8.5×10^{-5}
2000	6.7×10^{-5}	5.8×10^{-5}	7.3×10^{-5}	7.3×10^{-5}	5.7×10^{-5}	5.7×10^{-5}
2250	4.8×10^{-5}	5.0×10^{-5}	4.5×10^{-5}	5.4×10^{-5}	4.4×10^{-5}	4.2×10^{-5}
2500	3.6×10^{-5}	3.7×10^{-5}	3.8×10^{-5}	3.2×10^{-5}	3.4×10^{-5}	3.3×10^{-5}

*$F_{o\infty}$ (calc) $= \dfrac{\sigma_{10}}{\sigma_{01} + \sigma_{10}}$

TABLE 3 (cont.)

Proton Energy (keV)	Target Gas			
	CH_4		C_2H_4	
	$F_{o\infty}$		$F_{o\infty}$	
	Meas.	Calc.*	Meas.	Calc.*
100	1.7×10^{-1}	2.0×10^{-1}	1.8×10^{-1}	2.1×10^{-1}
200	2.5×10^{-2}		2.8×10^{-2}	
300	6.0×10^{-2}	7.0×10^{-2}	8.4×10^{-3}	6.6×10^{-3}
400	2.4×10^{-3}		3.0×10^{-3}	
550	1.4×10^{-3}	1.2×10^{-3}	1.5×10^{-3}	1.4×10^{-3}
800	4.5×10^{-4}	4.6×10^{-4}	5.6×10^{-4}	6.0×10^{-4}
1000	2.4×10^{-4}	3.0×10^{-4}	3.4×10^{-4}	3.5×10^{-4}
1250	1.5×10^{-4}	1.7×10^{-4}	1.6×10^{-4}	2.5×10^{-4}
1500	1.1×10^{-4}	1.1×10^{-4}	1.3×10^{-4}	1.5×10^{-4}
1750	7.3×10^{-5}	7.5×10^{-5}	7.0×10^{-5}	10.6×10^{-5}
2000	4.7×10^{-5}	5.3×10^{-5}	5.6×10^{-5}	6.0×10^{-5}
2250	3.5×10^{-5}	3.5×10^{-5}	4.0×10^{-5}	4.6×10^{-5}
2500	2.4×10^{-5}	2.3×10^{-5}	2.8×10^{-5}	3.6×10^{-5}

$$^{*}F_{o\infty}\ (\text{calc}) = \frac{\sigma_{10}}{\sigma_{01} + \sigma_{10}}$$

TABLE 3 (cont.)

Proton Energy (keV)	Target Gas			
	C_2H_6		C_4H_{10}	
	$F_{o\infty}$		$F_{o\infty}$	
	Meas.	Calc.*	Meas.	Calc.*
100	1.9×10^{-1}	2.1×10^{-1}	2.0×10^{-1}	2.0×10^{-1}
200	2.8×10^{-2}		3.2×10^{-2}	
300	6.0×10^{-3}	7.2×10^{-3}	6.8×10^{-3}	8.1×10^{-3}
400	2.0×10^{-3}		2.6×10^{-3}	
550		1.2×10^{-3}	1.1×10^{-3}	1.3×10^{-3}
800	4.6×10^{-4}	4.8×10^{-4}	5.0×10^{-4}	6.4×10^{-4}
1000	3.2×10^{-4}	3.4×10^{-4}	2.2×10^{-4}	3.3×10^{-4}
1250	1.5×10^{-4}	2.0×10^{-4}	1.9×10^{-4}	2.1×10^{-4}
1500	1.2×10^{-4}	1.3×10^{-4}		1.4×10^{-4}
1750	7.3×10^{-5}	7.6×10^{-5}	8.0×10^{-5}	9.2×10^{-5}
2000	5.0×10^{-5}	5.7×10^{-5}	5.4×10^{-5}	6.2×10^{-5}
2250	3.5×10^{-5}	3.6×10^{-5}	4.0×10^{-5}	3.8×10^{-5}
2500	2.7×10^{-5}	2.5×10^{-5}	2.8×10^{-5}	3.4×10^{-5}

*$F_{o\infty}$ (calc) $= \dfrac{\sigma_{10}}{\sigma_{01} + \sigma_{10}}$

The charge transfer cross sections measured in this work are compared with existing theoretical and experimental results in Figures 7 through 16. As described in Chapter II the majority of the theoretical calculations are for hydrogen targets. Due to the large number of calculations for electron capture from hydrogen only a few were plotted in Figure 7 for comparison with the present work. The theoretical results selected for comparison were as follows: (1) the Born approximation calculations of Mapleton[25] in which capture into seven final states was considered; (2) the distorted wave approximation of Bassel and Gerjuoy[23] for capture into the ground state; (3) the impact parameter calculation by McCarroll[40] for capture from the 1s state of the target to the 1s state of the projectile and the Born approximation of Taun and Gerjuoy[31] which includes the molecular effects of the H_2 target. The electron loss cross section has been calculated by Bates and Griffing.[36] This is a calculation by means of the Born approximation which includes transitions which may occur in the target atom simultaneously with the loss of an electron from the projectile atom. The electron loss cross sections for atomic hydrogen particles on hydrogen has also been calculated by Dmitriev and Nikolaev.[11] Their calculation is by means of a free-collision approximation and the results are identical to those of Bates and Griffing. The theoretical calculations for atomic hydrogen targets are multiplied by a factor of two for comparison with experimental results. The previously measured cross sections which are

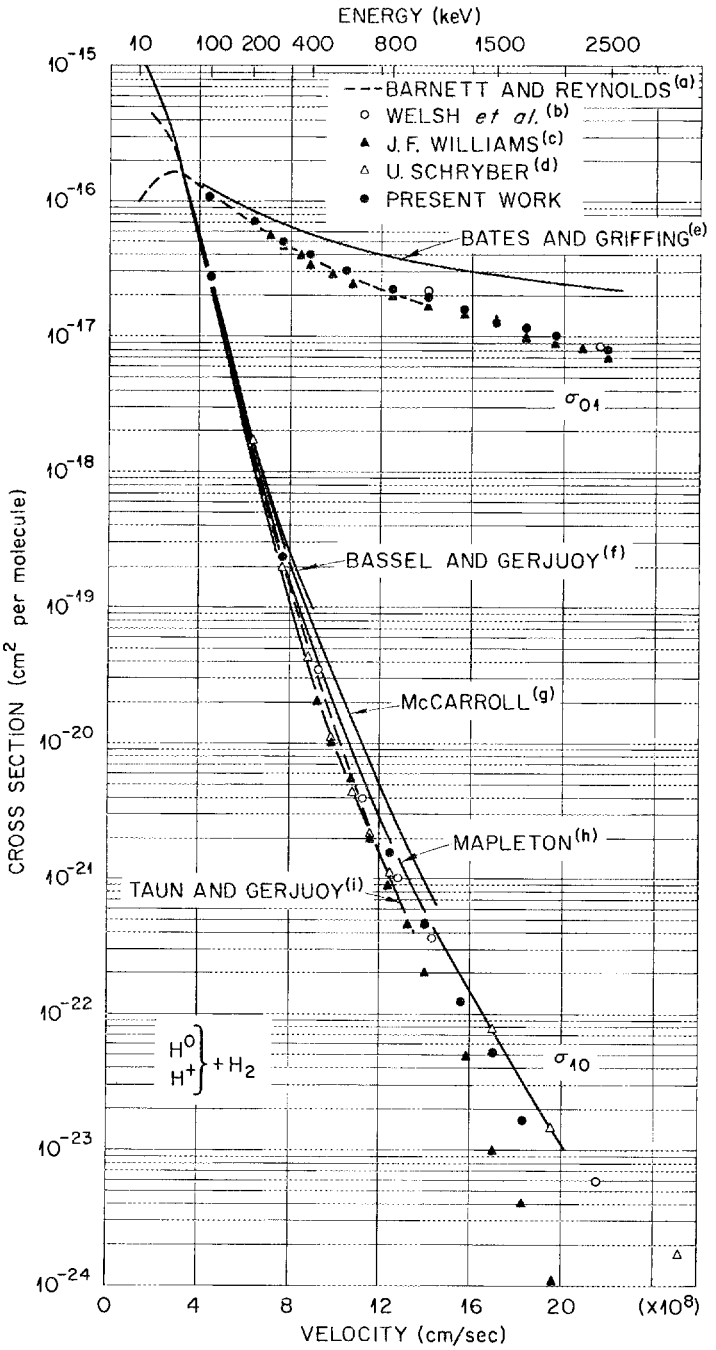

Fig. 7. The single-electron capture and loss cross sections for protons and atomic hydrogen, respectively, on hydrogen with previous experimental and theoretical values. The electron capture cross sections reported by Williams have been multiplied by a factor of two because of what appears to be an error in his paper. Experimental results: (a) see reference 45, (b) see reference 47, (c) see reference 46, and (d) see reference 48. Theoretical results: (e) see reference 36, (f) see reference 23, (g) see reference 40, (h) see reference 25, and (i) see reference 31.

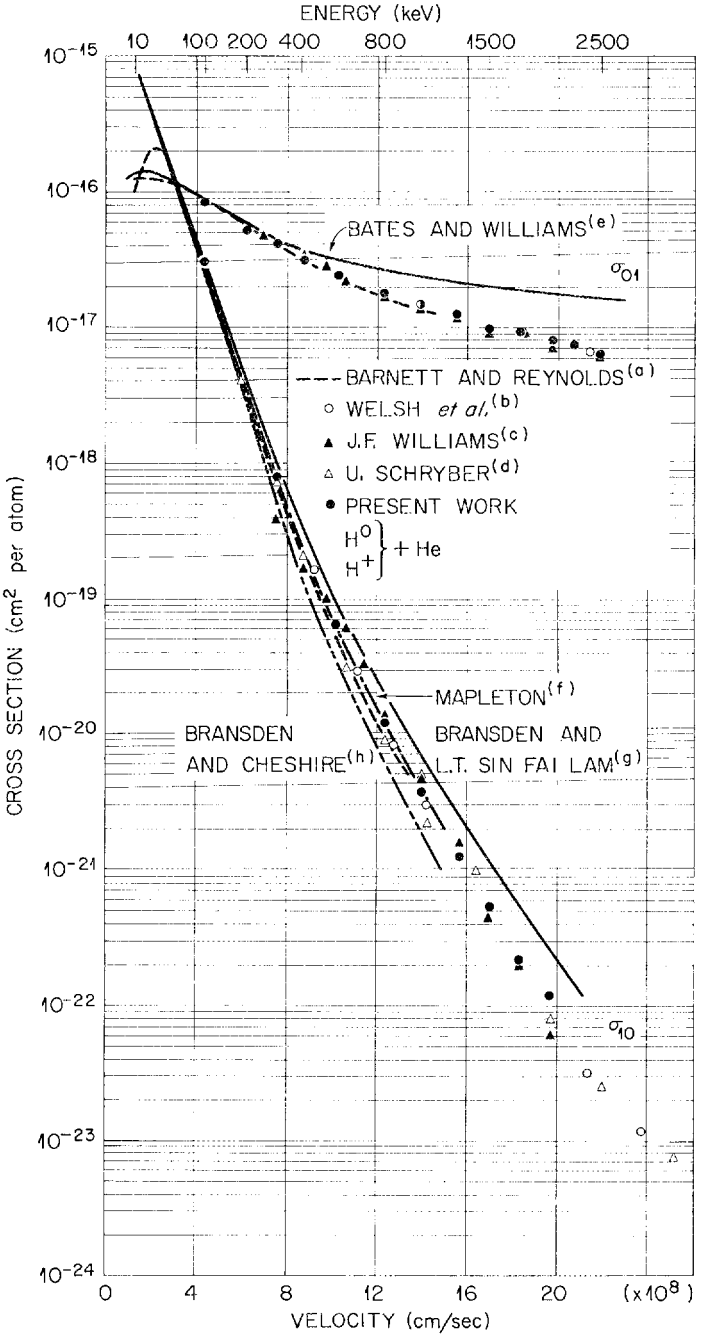

Fig. 8. The single-electron capture and loss cross sections for protons and atomic hydrogen, respectively, on helium with previous experimental and theoretical values. Experimental results: (a) see reference 45, (b) see reference 47, (c) see reference 46, and (d) see reference 48. Theoretical results: (e) see reference 37, (f) see reference 49, (g) see reference 50, and (h) see reference 38.

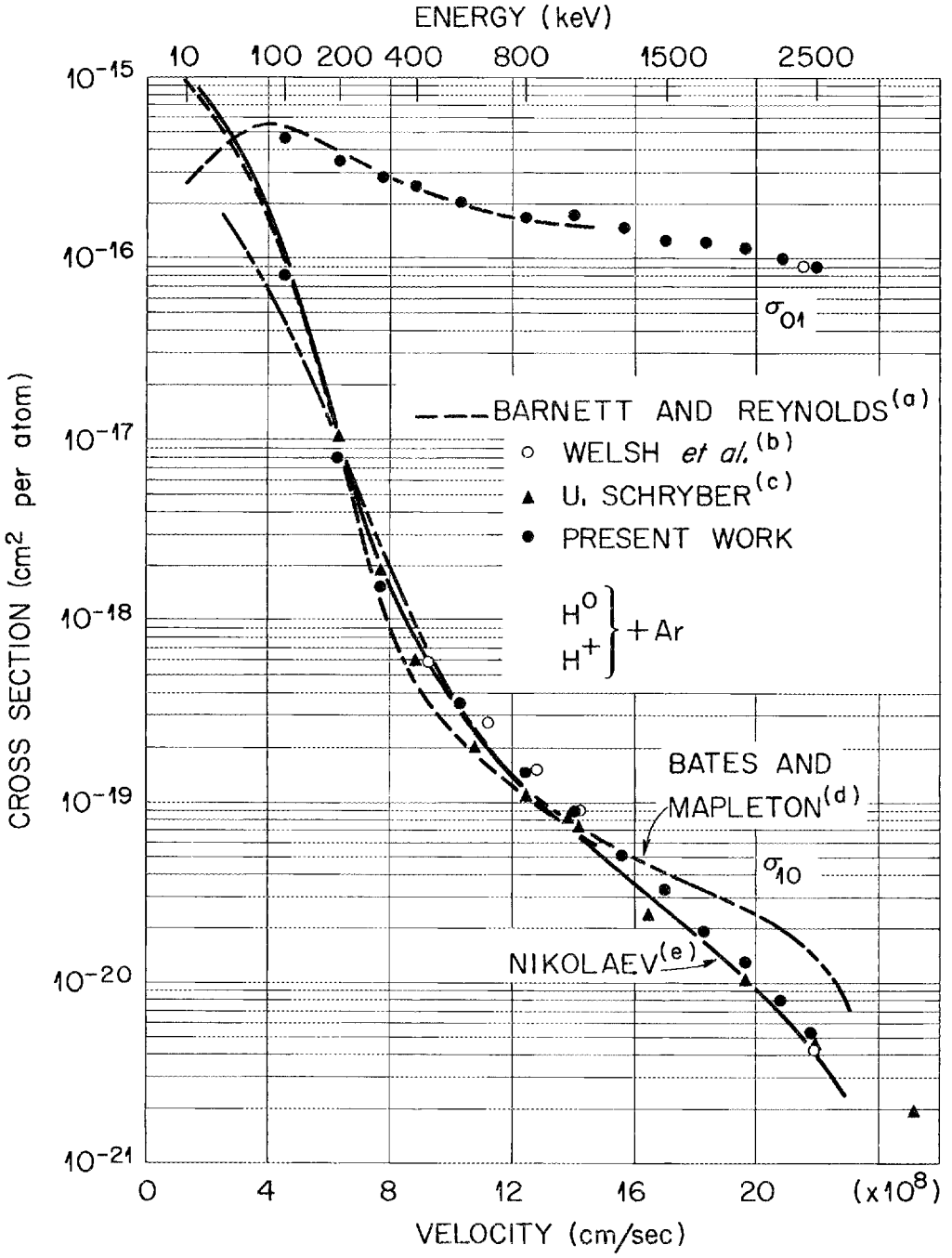

Fig. 9. The single-electron capture and loss cross sections for protons and atomic hydrogen, respectively, on argon with previous experimental and theoretical values. Experimental results: (a) see reference 45, (b) see reference 47, and (c) see reference 48. Theoretical results: (d) see reference 9, and (d) see reference 30.

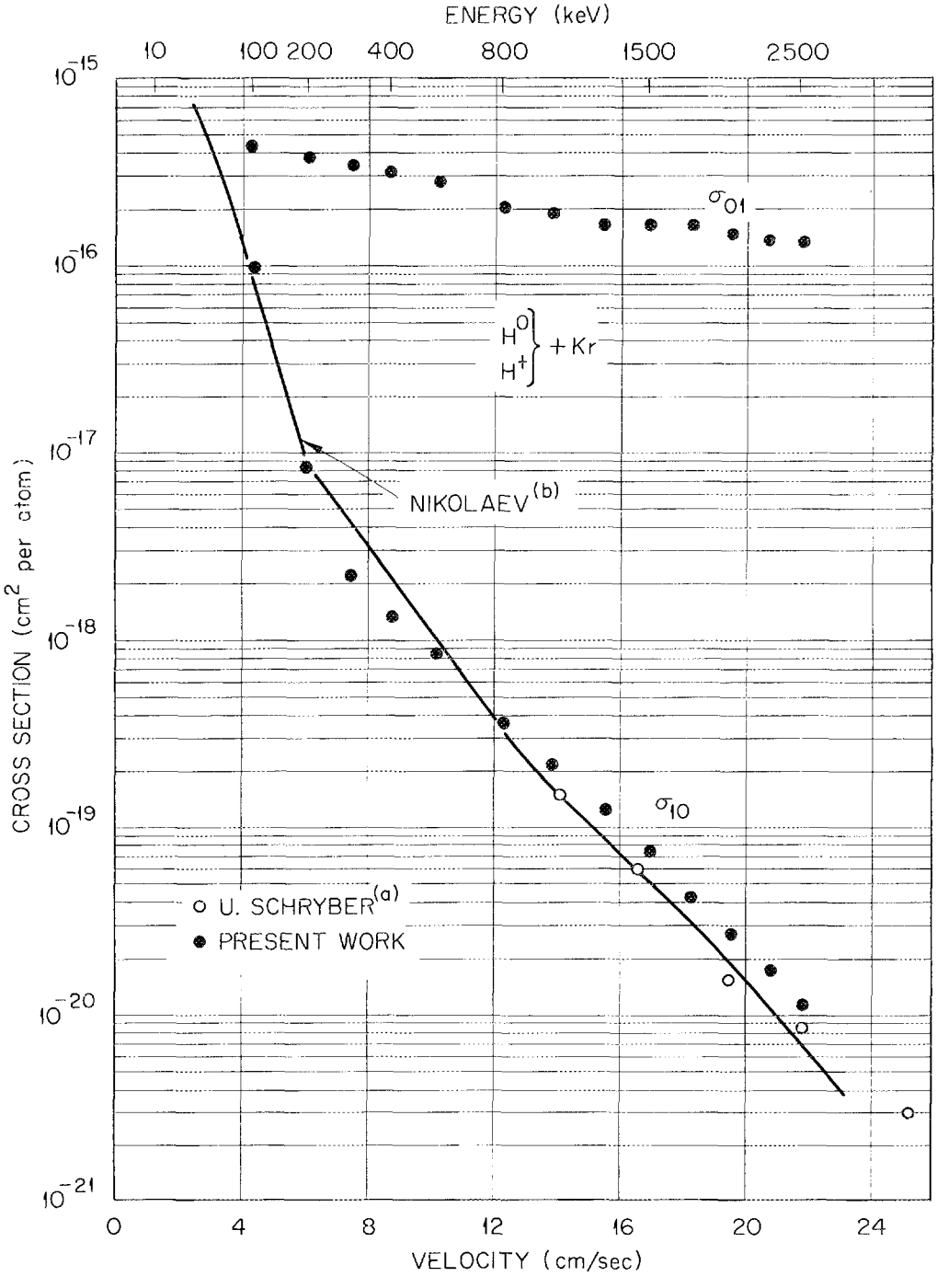

Fig. 10. The single-electron capture and loss cross sections for protons and atomic hydrogen, respectively, on krypton with previous experimental and theoretical values. Experimental results: (a) see reference 48. Theoretical results: (b) see reference 30.

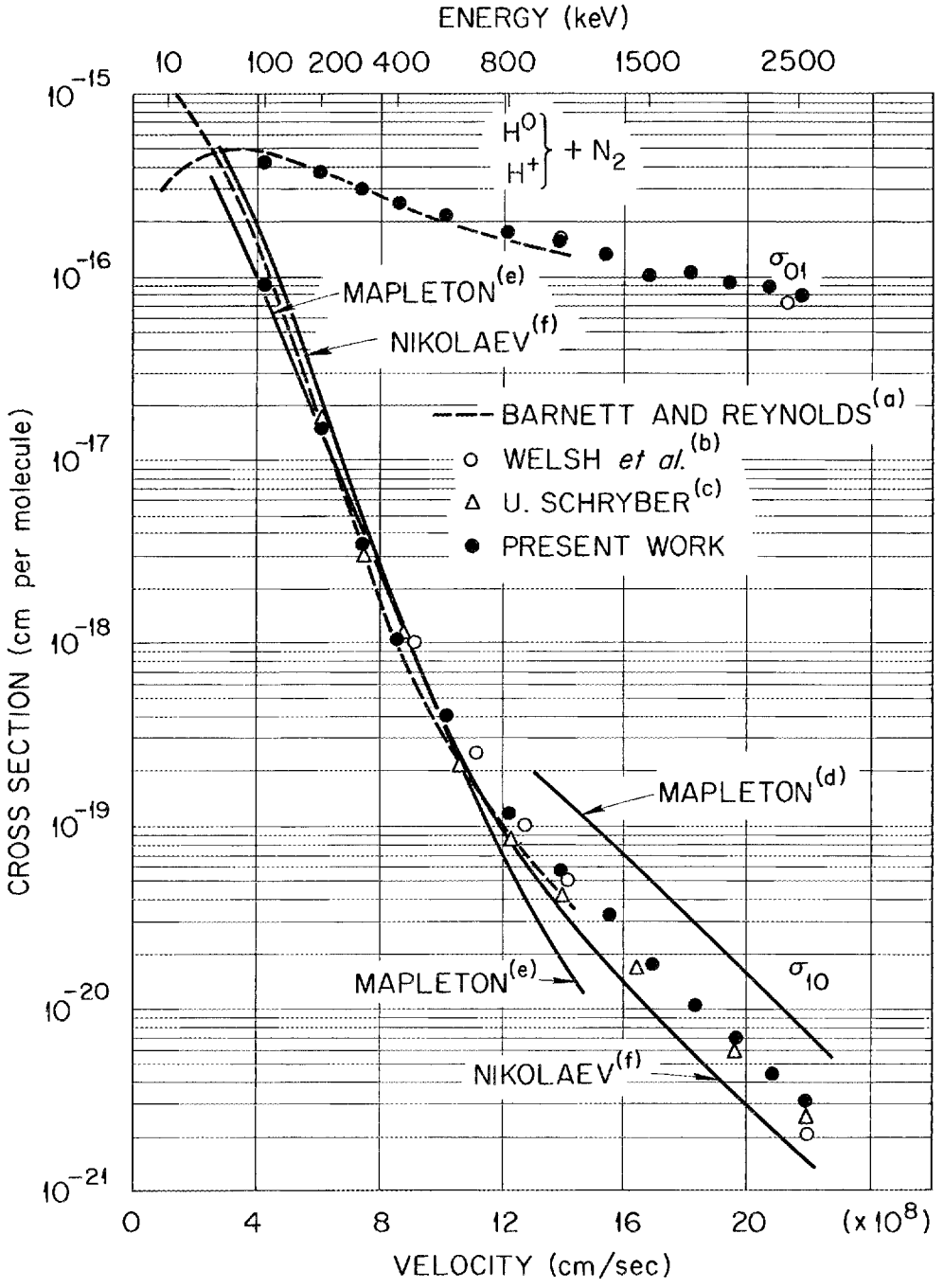

Fig. 11. The single-electron capture and loss cross sections for protons and atomic hydrogen, respectively, on nitrogen with previous experimental and theoretical values. Experimental results: (a) see reference 45, (b) see reference 47, and (c) see 48. Theoretical results: (d) see reference 29, (e) see reference 26, and (f) see reference 30.

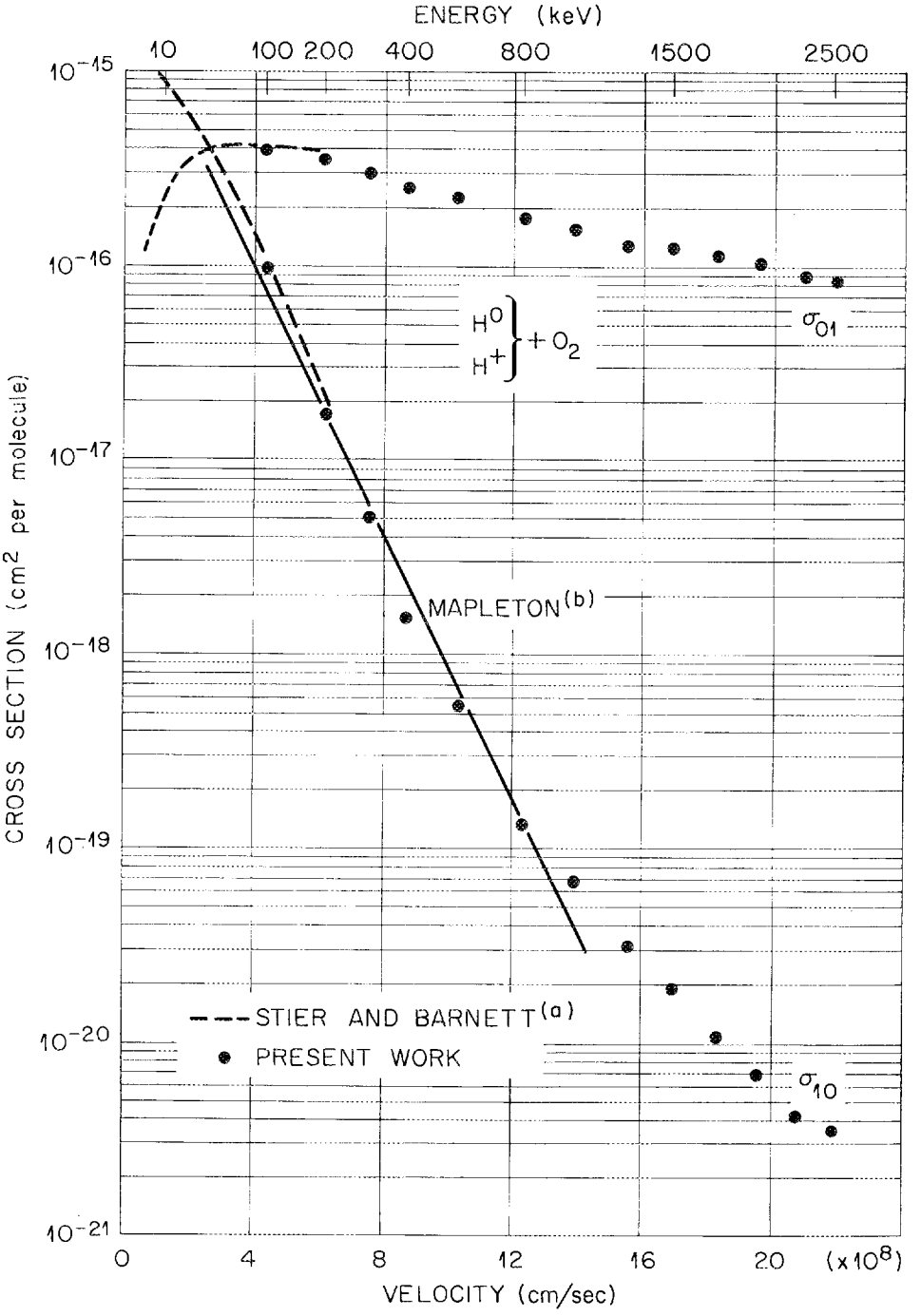

Fig. 12. The single-electron capture and loss cross sections for protons and atomic hydrogen, respectively, on oxygen with previous experimental and theoretical values. Experimental results: (a) see reference 51. Theoretical results: (b) see reference 26.

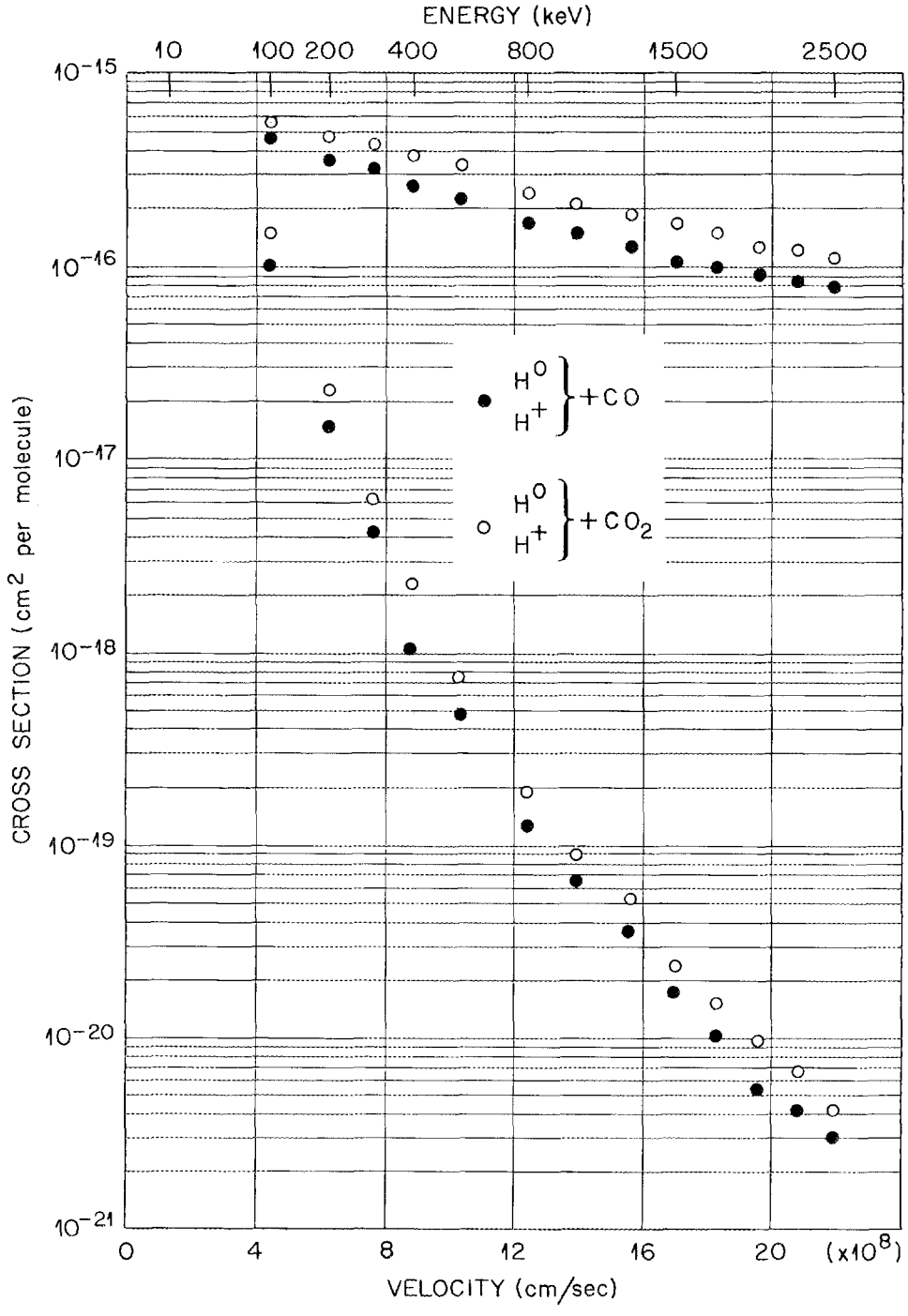

Fig. 13. The single-electron capture and loss cross sections for protons and atomic hydrogen, respectively on carbon monoxide and carbon dioxide.

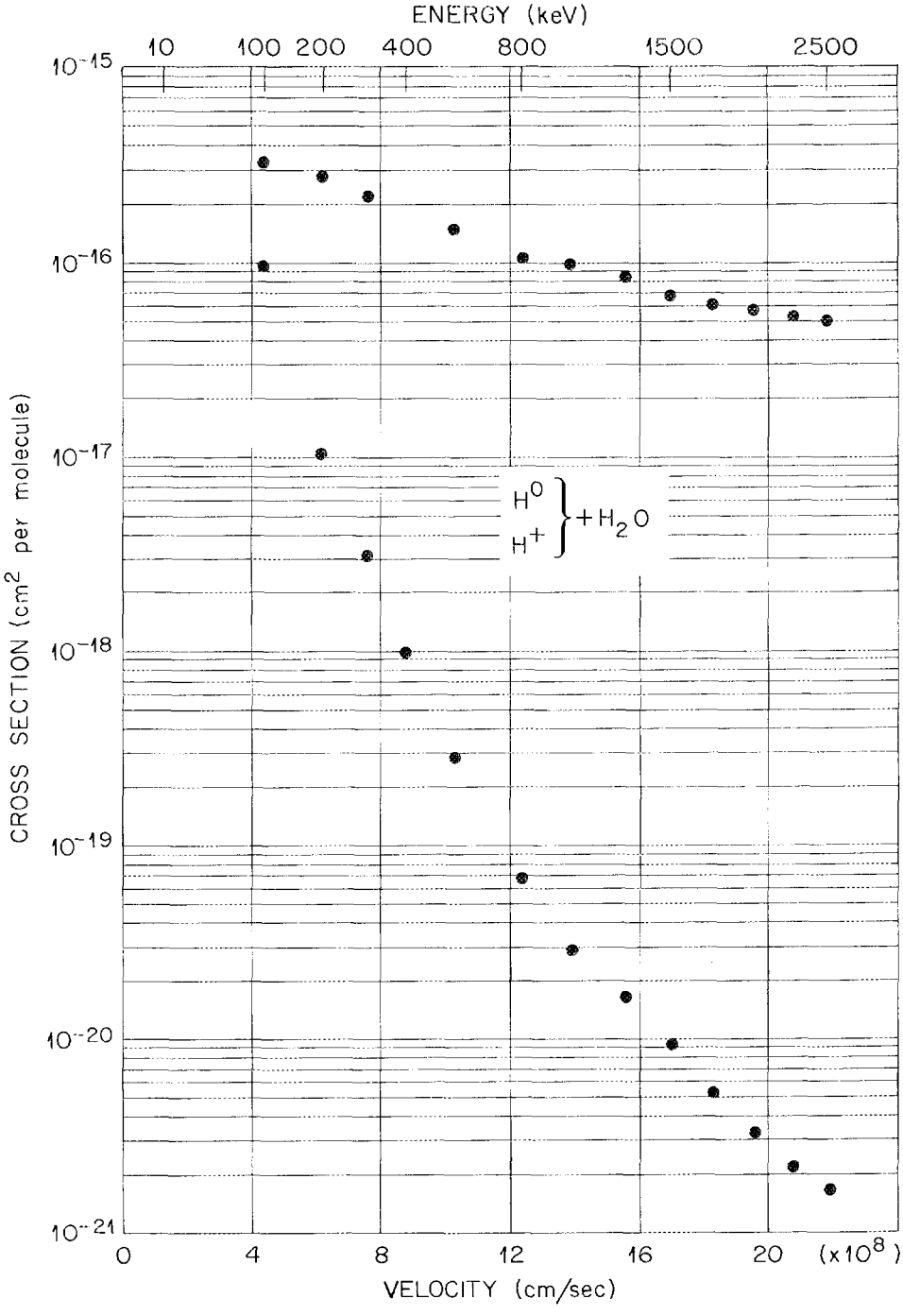

Fig. 14. The single-electron capture and loss cross sections for protons and atomic hydrogen, respectively, on water vapor.

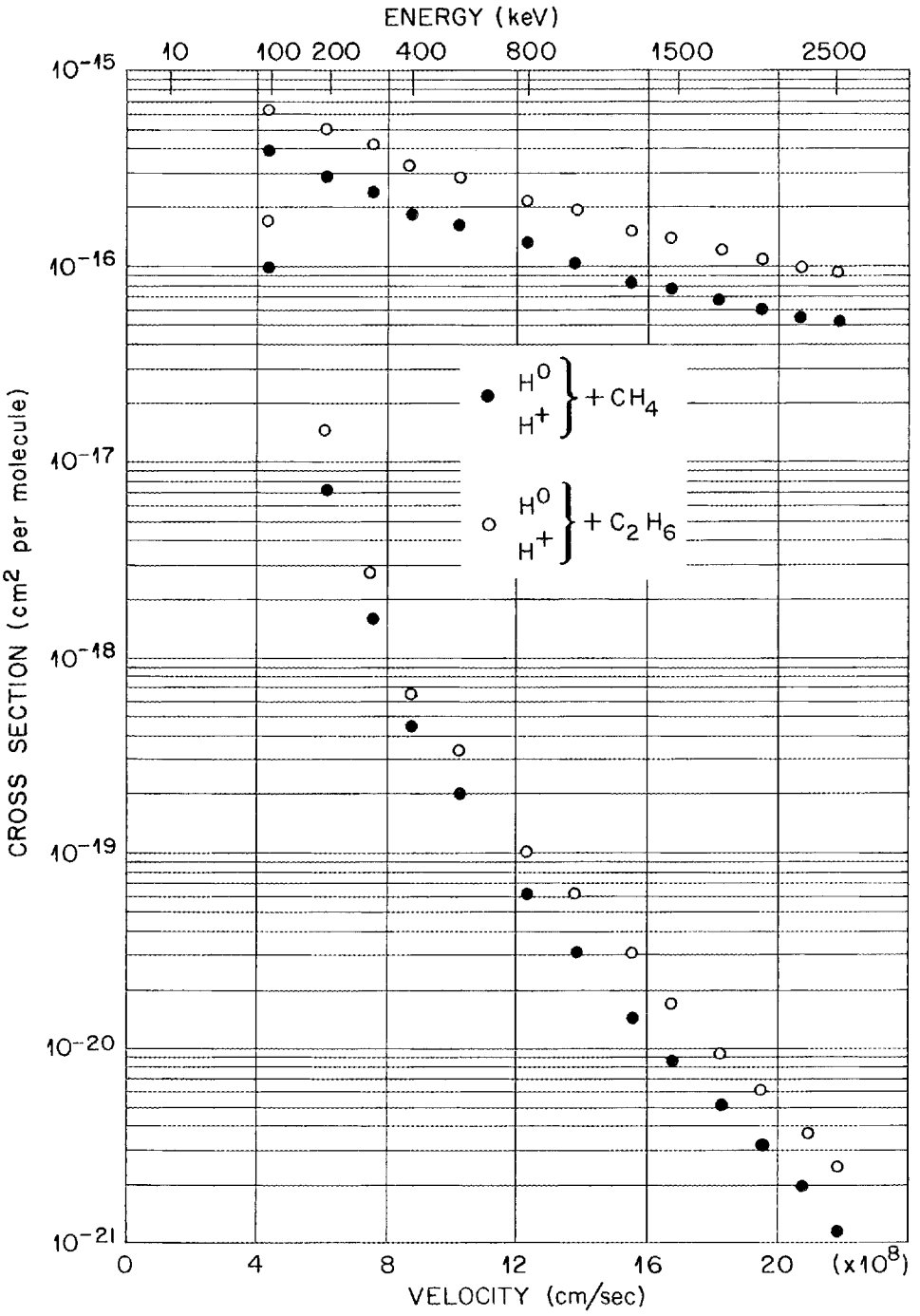

Fig. 15. The single-electron capture and loss cross sections for protons and atomic hydrogen, respectively, on methane and ethane.

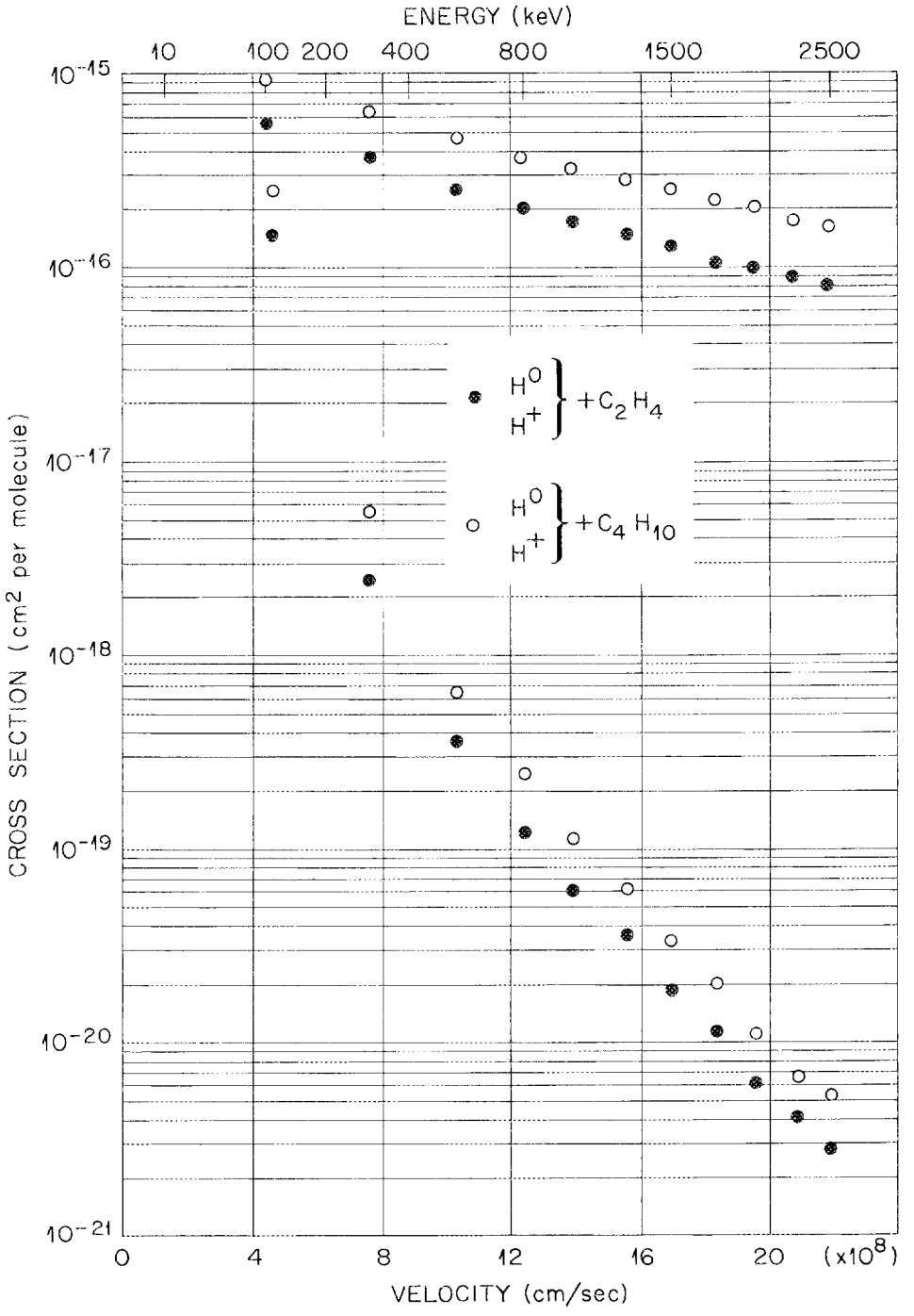

Fig. 16. The single-electron capture and loss cross sections for protons and atomic hydrogen, respectively, on ethylene and butane.

presented for comparison in the energy region corresponding to the results of the present work were reported by Barnett and Reynolds,[45] Williams,[46] Welsh et al.,[47] and Schryber.[48]

Agreement among the measured cross sections is quite good except for the high-energy electron capture cross sections reported by Williams.[46] His values decrease more rapidly with energy than do the other measured values. Although there is relatively good agreement between theoretical and experimental values at energies of approximately 100 keV, wide discrepancies occur at higher energies. The calculated electron capture cross sections of Mapleton[25] and of Taun and Gerjuoy,[31] however, are in good agreement with the experimental values to energies of 1 MeV.

Figure 8 is a comparison of experimental and theoretical results for the target gas helium. Several theoretical calculations of the electron capture cross sections have been made for helium targets. In order to avoid confusion in the drawing only three different theoretical calculations are plotted in Figure 8. The results of Mapleton[49] were obtained by a Born approximation using a simple helium wave function. The results of Bransden and Cheshire[38] were obtained by means of the impulse approximation; whereas the impace parameter formulation was used by Bransden and Sin Fai Lam.[50] The electron loss cross sections have been calculated by Bates and Williams.[37] The Born approximation was used for this calculation which includes the possibility of excitation and ionization of the residual helium atom as the electron is

removed from the incident hydrogen atom. The electron loss cross sections have also been calculated by Dmitriev and Nikolaev[11] by means of a free-collision approximation. Their results are identical to the results of Bates and Williams. The previously measured cross sections presented in Figure 8 for comparison with the present work are the results of Barnett and Reynolds,[45] Williams,[46] Welsh et al.,[47] and Schryber.[48]

There is very good agreement among the measured cross sections reported by different authors over the entire energy range. The theoretical values are, as was the case for hydrogen targets, in good agreement with measured values at energies near 100 keV. At higher energies the results of the electron capture cross sections of Mapleton[49] are in close agreement with measured values; whereas discrepancies as large as 100% occur between the calculated values of other authors and the measured values for incident particle energies of 1 MeV. The theoretical electron loss cross sections are found to decrease more slowly with energy than the measured values. The calculated values are a factor of two larger than the measured values at 1 MeV.

In Figure 9 the present results are compared with previous measurements and theoretical predictions for the target atom argon. Overall there is good agreement among the cross sections measured by the different workers. There are, however, discrepancies in the energy range of 500 to 1000 keV. In this energy range the present work is in close agreement with the work of Welsh et al.[47] while it is higher than the work of Barnett and Reynolds[45] and of Schryber[48] by as much as 50%. The theoretical values of both Bates

and Mapleton[9] and Nikolaev[30] include contributions to the electron capture cross sections due to capture of electrons from the inner shells of the target atom. The modified Born calculation of Nikolaev is in close agreement with the measured values, whereas, the semiclassical calculation of Mapleton underestimates the cross sections at low energies and overestimates the cross sections at high energies.

The cross sections for the target gas krypton are shown in Figure 10. The modified Born approximation of Nikolaev[30] is seen to give approximate agreement with the measured values. At energies above 1 MeV the theoretical electron capture cross sections are in close agreement with the measured values of Schryber;[48] however, these values are nearly 30% lower than the results of the present measurements.

Figure 11 contains a comparison of the cross sections determined in the present work with previous theoretical and experimental values for the target molecule nitrogen. At energies below 500 keV excellent agreement is obtained among the measured values. At energies above 500 keV the present results are in close agreement with the results of Welsh et al.;[47] however they are 15 to 20% higher than the values of Barnett and Reynolds[45] and Schryber.[48] The calculated electron capture cross sections of Mapleton,[26] which includes only capture of 2p electrons, are in close agreement with the measured values for energies as high as 800 keV. These calculated cross sections decrease more rapidly than measured values at higher energies

because capture from inner electron shells then becomes energetically possible. An estimation of the capture cross section for energies greater than 1 MeV which includes inner shell contributions has been made by Mapleton;[29] this calculation overestimates the cross sections by more than a factor of two. Nickolaev[30] has also calculated the electron capture cross sections for protons on nitrogen. His calculation, which includes the possibility of electron capture from inner electron shells of the target atom, are in good agreement with measured values for energies of 100 to 800 keV. Although Nikolaev's results are in closer agreement with measured values at high energy than Mapleton's calculations for the capture of 2p electrons, his results are still nearly a factor of two too small at energies above 1 MeV.

The only other target gas studied for which previous data are available for comparison is oxygen. Figure 12 shows the cross sections measured in the present work, the measured values of Stier and Barnett,[51] and the calculated values of Mapleton.[26] Good agreement is obtained between the present measurements and those of Stier and Barnett in the small energy region of overlap. Agreement is also obtained between the present results and the calculated electron capture cross sections of Maplteon[27] in the energy range 100 to 800 keV. For energies above 800 keV, where electron capture from inner levels of oxygen becomes energetically possible, the results of Mapleton are expected to decrease more rapidly with energy than the measured values since his results include only the capture of 2p electrons.

Figures 13 through 16 show graphically the results obtained in the present work for several other gases. These figures along with Figures 7 through 12 show the similar nature of both, electron capture and electron loss, cross sections with the different target molecules.

Figure 17 is an example of the $\log_{10} \sigma_{10}$ versus $\log_{10} E$ plots which were used to determine the velocity dependence of the electron capture cross sections. If the cross sections are proportional to some power of the velocity, $\sigma_{10} \propto v^{-k}$, a straight line will result. The slope of the straight line is proportional to k. An interesting feature of this $\log_{10} \sigma_{10}$ versus $\log_{10} E$ plot is that the onset of inner shell ionization is more pronounced than in the semilog plots of Figures 7 through 16. The gases CO, CO_2, and O_2 are linear for energies above about 200 keV, whereas, the other gases studied (except H_2 and He gases which have no inner shells) all show a departure from linearity at energies between 500 and 1000 keV. A small contribution to electron capture from the inner shells of nitrogen can be seen in Figure 17, whereas oxygen appears as a straight line for all energies from 200 to 2500 keV. Table 4 presents the velocity dependences of the cross sections. The velocity dependence of the electron capture cross sections for incident proton energies greater than 1 MeV is found to be approximately v^{-7} for the heavy gases. This is in approximate agreement with Bohr's prediction of $v^{-6.10}$ The velocity dependence of $v^{-10.6}$ found for the electron capture cross sections for protons on hydrogen is in close

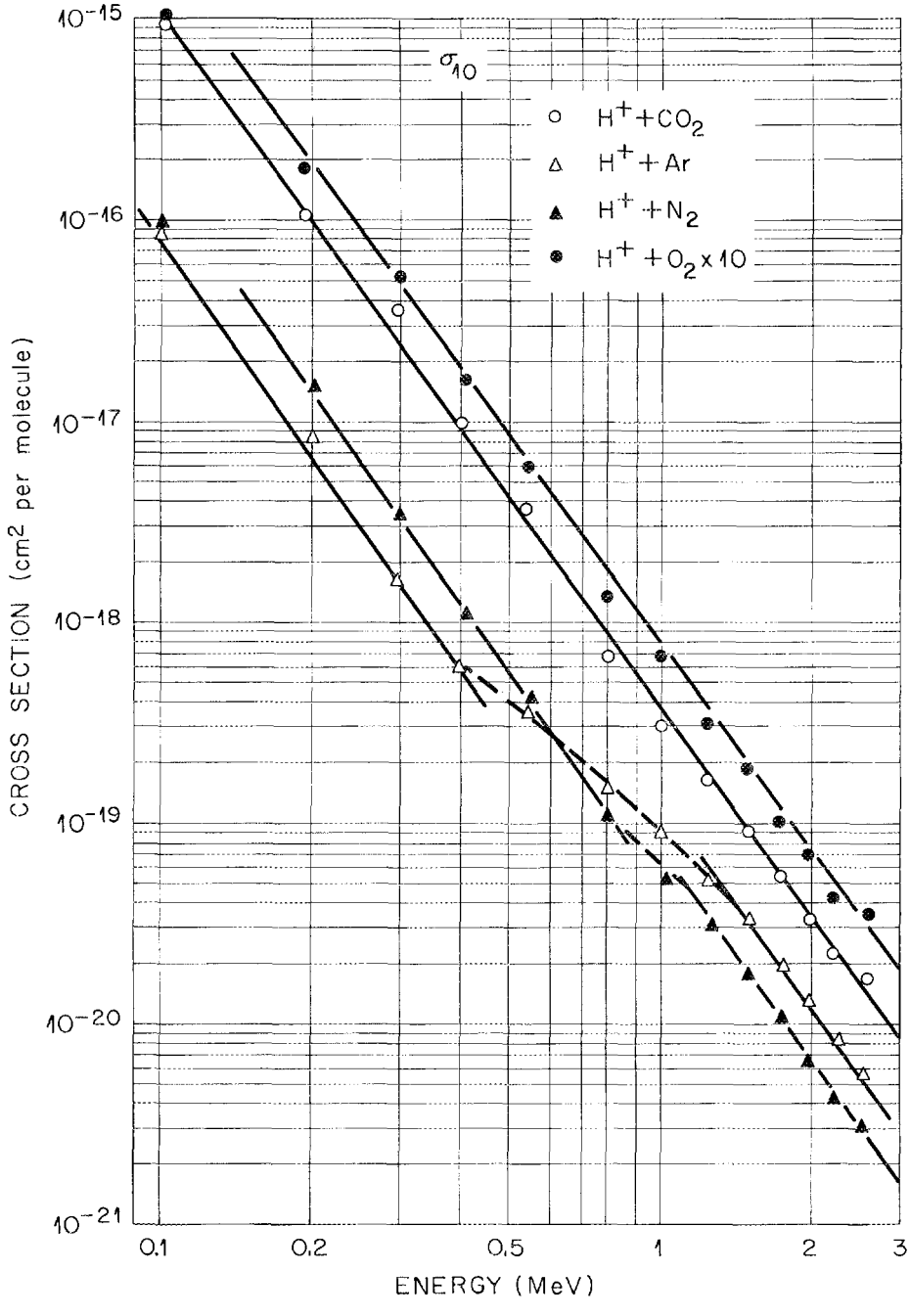

Fig. 17. The $\log_{10}$ of the single-electron capture cross section versus the $\log_{10}$ of the impact energy for protons on oxygen, nitrogen, carbon dioxide, and argon.

TABLE 4

VELOCITY DEPENDENCE OF THE SINGLE-ELECTRON CAPTURE AND LOSS CROSS SECTIONS

Target Gas	k^*			
	σ_{10}			σ_{01}
	$200 \leq E < 400$ keV	$400 < E < 1000$ keV	$1000 < E \leq 2500$ keV	$300 < E \leq 2500$ keV
H_2	10.6	10.6	10.6	1.70
He	9.7	9.7	9.7	1.76
Ar	7.1	4.4	7.1	0.98
Kr	7.0	**	7.0	0.98
N_2	7.2	**	7.2	1.52
O_2	6.9	6.9	6.9	1.20
H_2O	7.2	7.2	7.2	1.40
CO	6.6	6.6	6.6	1.38
CO_2	6.8	6.8	6.8	1.36
CH_4	8.0	6.1	8.0	1.64
C_2H_4	8.0	5.7	8.0	1.52
C_2H_6	8.0	5.7	5.7	1.52
C_4H_{10}	6.8	5.6	6.8	1.46

*$\sigma \propto v^{-k}$

**The value of k is continually changing in this energy region.

agreement with the v^{-11} dependence yielded by the classical calculations of Thomas[6] and the second Born approximation of Drisko.[22]

The velocity dependences for the electron loss cross sections given in Table 4 were obtained from $\log_{10} \sigma_{01}$ versus $\log_{10} E$ plots such as those shown in Figure 18. The straight line portion of these plots is reached at incident particle energies of about 300 keV and no departure from a straight line, within experimental uncertainties, is noted up to energies as high as 2500 keV. The velocity dependence of the electron loss cross sections which varies from 1.76 for helium to 0.98 for argon and krypton is in close agreement with the predictions of Bohr.[10] Bohr's classical calculations indicate that $\sigma_{01} \propto v^{-1}$ for heavy gases and $\sigma_{01} \propto v^{-2}$ for light gases. The uncertainties in the velocity dependence measured for each gas are estimated to be $\pm$ 10%.

A modification of the classical theory of Thomas[6] has been shown by Bates and Mapleton[8] to yield a parameter $\rho \propto \frac{\sigma_{10} E^{11/4}}{\lambda}$ which, when plotted as a function of E/J on a $\log_{10}$-$\log_{10}$ scale, is independent of the target atom. In this relationship σ_{10} is the measured electron capture cross section, E is the incident proton energy, J is the ionization potential of the target atom, and λ is a parameter deduced from the atomic potential of the target atom. This relationship has been tested by Bates and Mapleton[8] for incident proton energies less than 200 keV with excellent agreement among several different target atoms. Figure 19 shows the results of

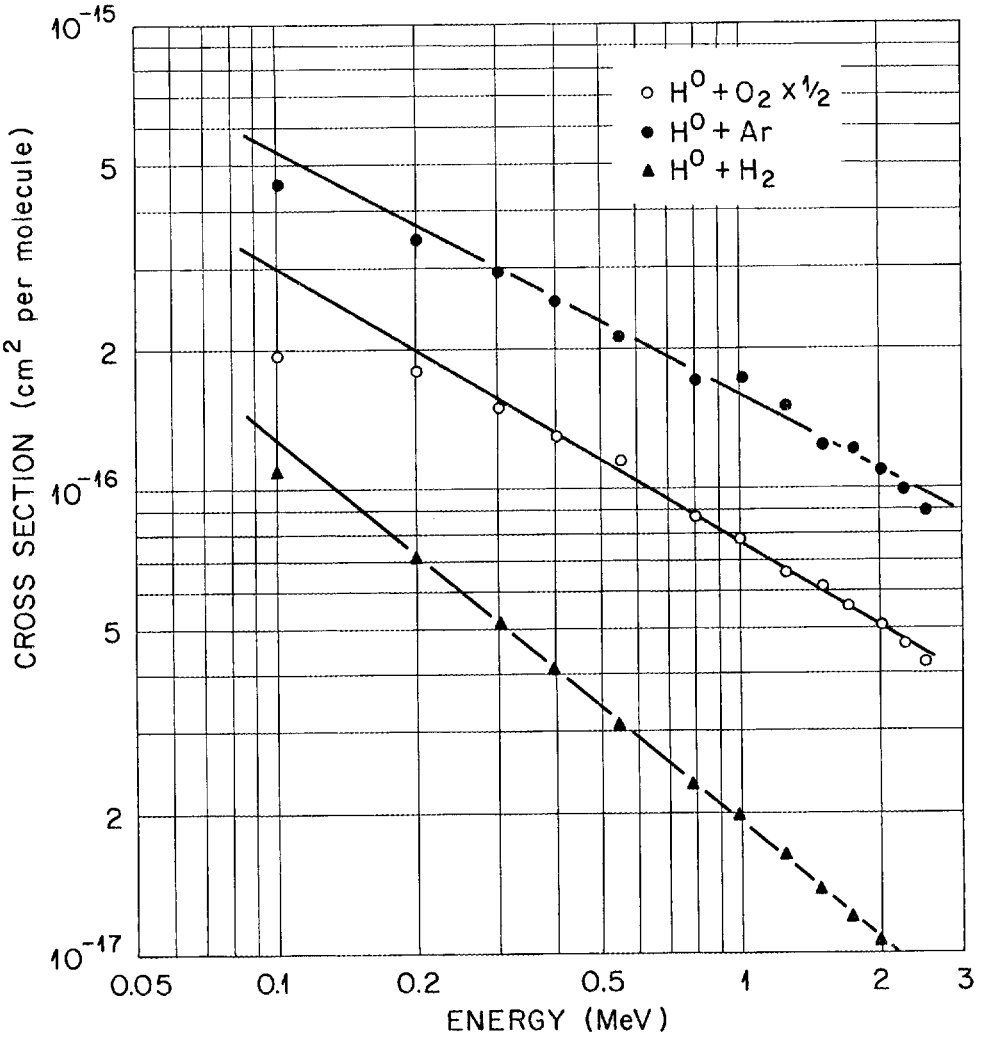

Fig. 18. The $\log_{10}$ of the single-electron loss cross section versus the $\log_{01}$ of the impact energy for hydrogen, argon, and oxygen.

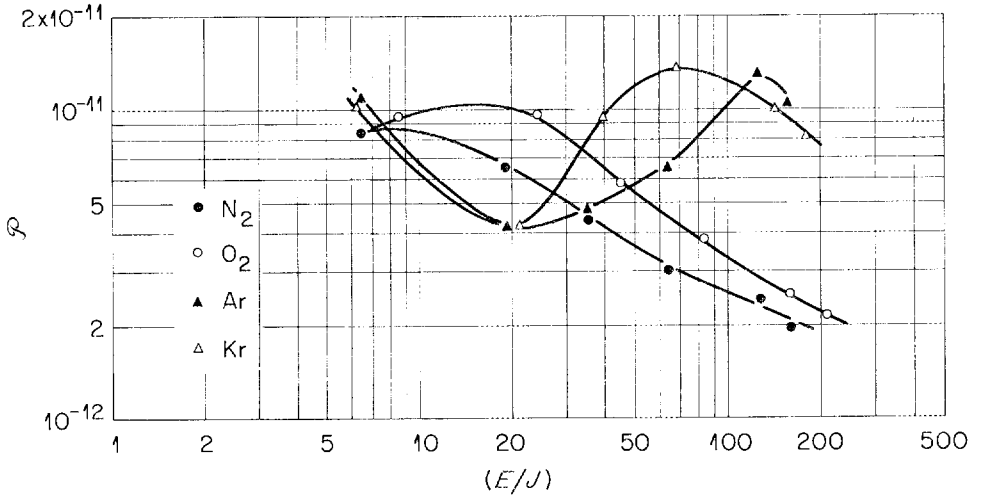

Fig. 19. The empirical parameter $\wp$ defined by Bates and Mapleton (see reference 8) versus the ratio of proton energy and ionization potential.

using the present results for σ_{10} in the calculation of Φ for proton energies from 100 to 2000 keV. The values for λ were obtained from Mapleton[52] and values for J were taken from reference 53. As can be seen in Figure 19 there is no evidence that Φ is strictly a function of E/J at energies above 300 keV ($E/J \cong 20$); however the spread of the points in Figure 19 may be due to an incomplete knowledge of the parameter J. At energies where electron capture from inner shells becomes possible the ionization potential is no longer a constant. In order to test the dependence of Φ on E/J explicitly the dependence of J on impact energy would be necessary.

With the measured cross section values of the various carbon-containing compounds, it is possible to estimate the charge transfer cross sections for carbon by applying an additive rule to the cross sections of the constituents of each compound. The possibility of using this procedure is based upon the assumption that, at high velocities of the incident particle, the target molecule appears as an assembly of individual atoms such that molecular forces are negligible. In an attempt to determine the carbon cross sections at a given energy by application of the sum rule to several carbon-containing compounds, an estimation of the accuracy of this rule may be obtained as well as an estimation of the magnitude of the charge transfer cross sections for carbon. Table 5 shows the results of an estimation of the carbon cross sections for electron capture and loss based on the sum rule applied to the gases H_2, O_2, CO, CO_2, CH_4, C_2H_4, C_2H_6,

TABLE 5

CHARGE TRANSFER CROSS SECTIONS FOR CARBON CALCULATED BY THE SUM RULE. THE VALUES LISTED IN THIS TABLE ARE IN UNITS OF 10^{-18} CM^2

Energy (keV)	100	300	550	800
σ_{01}				
$(\sigma_{CO} - \frac{1}{2}\sigma_{O_2})$	265	175	118	78
$(\sigma_{CO_2} - \sigma_{O_2})$	194	128	112	30
$(\sigma_{CH_4} - 2\sigma_{H_2})$	205	148	107	86
$\frac{1}{2}(\sigma_{C_2H_4} - 2\sigma_{H_2})$	165	129	94	47
$\frac{1}{2}(\sigma_{C_2H_6} - 3\sigma_{H_2})$	108	100	77	65
$\frac{1}{4}(\sigma_{C_4H_{10}} - 5\sigma_{H_2})$	173	135	96	77
Average	187 ± 80	136 ± 41	101 ± 25	64 ± 22
σ_{10}				
$(\sigma_{CO} - \frac{1}{2}\sigma_{O_2})$	48	1.83	0.23	0.058
$(\sigma_{CO_2} - \sigma_{O_2})$	45	1.40	0.20	0.060
$(\sigma_{CH_4} - 2\sigma_{H_2})$	42	1.41	0.18	0.058
$\frac{1}{2}(\sigma_{C_2H_4} - 2\sigma_{H_2})$	45	1.00	0.16	0.058
$\frac{1}{2}(\sigma_{C_2H_6} - 3\sigma_{H_2})$	44	1.14	0.15	0.048
$\frac{1}{4}(\sigma_{C_4H_{10}} - 5\sigma_{H_2})$	30*	1.08	0.14	0.059
Average	44.8 ± 2.8	1.31 ± 0.52	0.18 ± 0.05	0.056 ± 0.008

*Not included in average due to large deviation from the mean.

TABLE 5 (cont.)

Energy (keV)	1500	2000	2500
σ_{01}			
$(\sigma_{CO} - \frac{1}{2}\sigma_{O_2})$	52	41	38
$(\sigma_{CO_2} - \sigma_{O_2})$	45	32	28
$(\sigma_{CH_4} - 2\sigma_{H_2})$	49	39	33
$\frac{1}{2}(\sigma_{C_2H_4} - 2\sigma_{H_2})$	47	35	31
$\frac{1}{2}(\sigma_{C_2H_6} - 3\sigma_{H_2})$	44	36	30
$\frac{1}{4}(\sigma_{C_4H_{10}} - 5\sigma_{H_2})$	51	38	32
Average	45 ± 6	37 ± 5	32 ± 4
σ_{10}			
$(\sigma_{CO} - \frac{1}{2}\sigma_{O_2})$	0.0073	0.00151	0.00124
$(\sigma_{CO_2} - \sigma_{O_2})$	0.0046	0.00276	0.00045
$(\sigma_{CH_4} - 2\sigma_{H_2})$	0.0079	0.00315**	0.00120**
$\frac{1}{2}(\sigma_{C_2H_4} - 2\sigma_{H_2})$	0.0093	0.00300**	0.00115**
$\frac{1}{2}(\sigma_{C_2H_6} - 3\sigma_{H_2})$	0.0085	0.00300**	0.00136**
$\frac{1}{4}(\sigma_{C_4H_{10}} - 5\sigma_{H_2})$	0.0082	0.00300**	0.00130**
Average	0.0076 ± 0.0030	0.0027 ± 0.0012	0.0011 ± 0.0006

**Hydrogen cross section considered negligible.

and C_4H_{10}. The quoted uncertainties in the average values are the maximum variations from the average value. The ability of the sum rule to give a consistent value for the electron loss cross section is seen to increase steadily with increased impact energy. The electron capture cross sections do not show this increased consistency at higher energies. Even without obtaining a high degree of consistency between the electron capture cross sections, the individual values do not differ from the mean by more than approximately 50%. In the calculation of the electron capture cross sections at the two highest energies the contribution to the hydrocarbon cross sections from the hydrogen constituents was neglected. The error introduced at these high energies as a result of neglecting the hydrogen cross sections is considered negligible since the cross sections for hydrogen decrease with increased proton energies much more rapidly than the hydrocarbon cross sections.

Except for certain random cross sections, the values in Table 5 indicate that the sum rule may be applied in an attempt to estimate unknown charge transfer cross sections for incident protons and atomic hydrogen with energies from 100 to 2500 keV. The cross sections for carbon estimated by means of the sum rule are plotted in Figure 20. It must be emphasized that the sum rule is only an estimate and that effects of molecular forces on the measured cross sections are observed for incident particle energies as high as 2.5 MeV. The cross sections for ethane and ethylene are compared

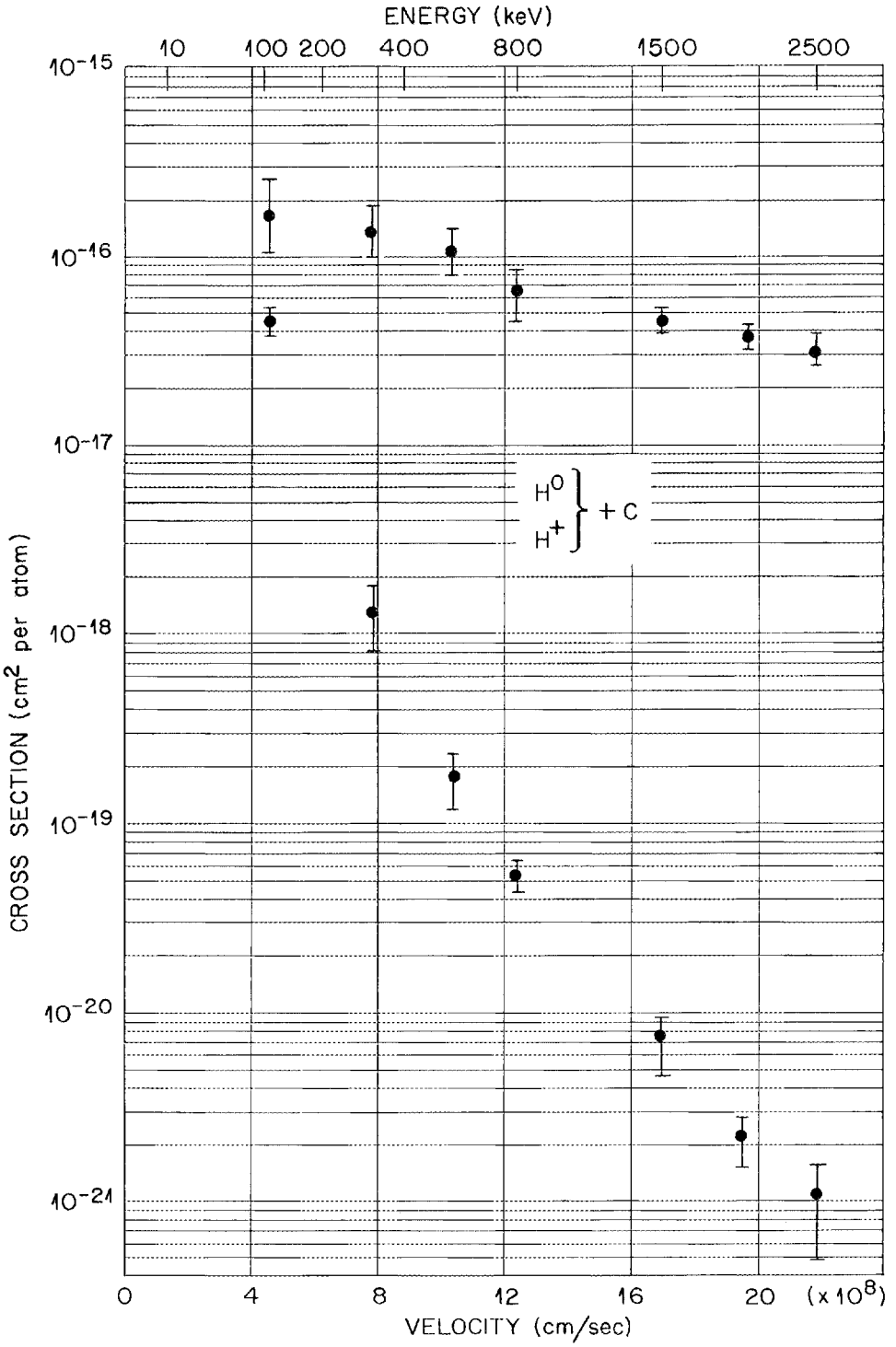

Fig. 20. The single-electron capture and loss cross sections for carbon as calculated by the sum rule.

in Figure 21 in order to show the effects of molecular forces on the cross sections. Since these molecules differ by two hydrogen atoms (ethane = ethylene + 2 hydrogen) the cross sections for molecular hydrogen are also plotted for reference. A close estimation of the electron loss cross section for ethane can be obtained by adding the corresponding cross sections of ethylene and hydrogen; however, this procedure does not give consistent results for the electron capture cross sections. Although the sum rule is found to give accurate results at incident proton energies near 100 keV the electron capture cross sections for ethylene for energies greater than 500 keV are larger than those of ethane and the addition of the hydrogen cross section to ethylene only increases the differences. The discrepancies between the measured values and those predicted by the sum rule in the case of ethylene and ethane are small, approximately 20%; however, these discrepancies point out that even for incident particle energies as high as 2.5 MeV a molecule cannot be precisely described as an assembly of independent atoms.

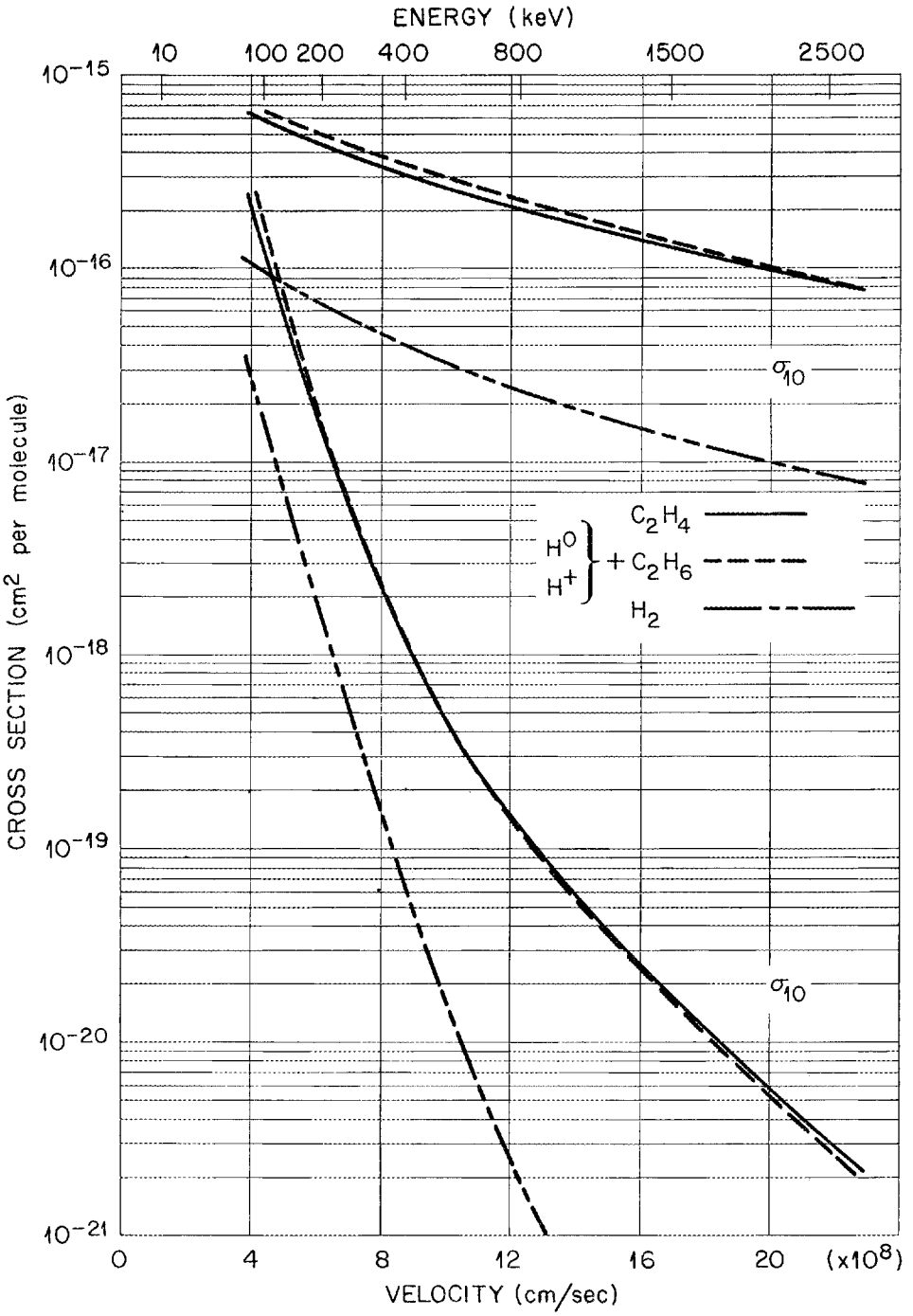

Fig. 21. The single-electron capture and loss cross sections for protons and atomic hydrogen, respectively, in ethane, ethylene, and hydrogen.

CHAPTER V

ACCURACY AND VALIDITY OF THE MEASUREMENTS

The uncertainties in the measured cross sections result primarily from the following factors: (1) uncertainty in the effective path length of the collision cell; (2) approximate corrections for small variations from "thin" target conditions; (3) uncertainties in the measurement of target gas pressures; (4) statistical and systematic uncertainties in the measurement of beam intensities; (5) impurities in the target gases; and (6) possible excited states in the incident atomic hydrogen beam.

The path lengths of the collision cells were measured for both the long and short collision cells to within $\pm$ 0.06 inches. The increase in measured path length due to gas streaming through the apertures as a result of differential pumping of the collision cells was estimated by a comparison of data obtained by means of the two collision cells as well as the calculations presented in Appendix II. This error results in a measured cross section slightly higher than the "true" value. The increase in path length due to differential pumping was estimated to be less than 1% for the long cell. Both the simple calculations in Appendix II and the comparison of data obtained with the two collision cells show that end effects of approximately 3% occurs with the short collision cell.

Errors in the measured cross sections due to multiple collisions result in the measured value being smaller than the "true" value. Corrections to the data to account for variations from "thin" target conditions were not considered necessary for the short cell due to the small probability of second collisions occurring. The maximum gas density used corresponded to the ratio $I_{H^+}/(I_{H^0} + I_{H^+}) = 0.05$ which resulted in less than 2.5% error in the measured cross sections. When the long path length collision cell was used the departure from "thin" target conditions was more pronounced. Values of $I_{H^+}/(I_{H^0} + I_{H^+}) = 0.20$ were encountered when large cross sections were measured. The error in the cross section determined as a result of allowing $I_{H^+}/(I_{H^0} + I_{H^+})$ to approach 0.20 is approximately 10%. The correction necessary to account for this systematic error was explained in section C of Chapter III. The approximate manner of this correction, which was applied to all cross sections obtained by means of the long collision cell, introduced uncertainties of $\pm$ 3% in the absolute values of the cross sections.

The uncertainty in the absolute pressure measurement is approximately $\pm$ 3% as is described in Appendix I. Uncertainties in the measurement of relative pressures due to meter fluctuations and small drifts in pressure during data accumulation also amount to approximately 3%.

The uncertainties in the determination of beam intensities result from two major causes, statistical errors in single particle counting techniques and errors in the determination of the average particle currents

when the electrometer was used. The electrometer calibration was accurate to within a few percent. Enough data were accumulated in all cases to reduce counting statistics to less than 1%; however, the current averaging process may introduce uncertainties as high as 10%.

Random uncertainties in the cross sections due to the determination of beam intensities and target gas pressures can be evaluated best by the uncertainties in obtaining the slope of a straight line through the points of a plot of the intensity ratios versus pressure. This plot has a tendency to average the fluctuations for individual points when the cross section is evaluated. The slope of each set of points was determined by a least squares fit calculated by means of an ORNL computer. Uncertainties in the slope of the straight line vary from 3 to 5% depending on the manner in which the intensities were measured. The larger uncertainty is associated with intensity data obtained by means of the Faraday-cup.

Since cross sections were determined from the slope of a straight line which resulted from plots of the intensity ratios versus pressure, the effect of uncertainties in the knowledge of absolute target gas pressures were minimized. In the pressure range used, an error in the absolute pressure as high as 10% was found to cause less than 2% error in the measured cross section. The uncertainty of $\pm$ 3% in the absolute value of the pressure which occurred in the present work was, therefore, negligible when cross sections were determined in this way.

The combined effects of the uncertainties discussed above result in uncertainties in the measured electron capture and loss cross sections of 8% and 6%, respectively. The larger uncertainty results from the use of the Faraday-cup for these measurements.

The target gases, except water vapor, were purchased from commercial sources. These gases had less than 0.5% impurities except for CO_2 which was 98.5% pure. Water vapor was obtained from triply distilled water which had been pumped by means of a fore pump for eight hours while being frozen and thawed in order to remove absorbed gases. The impurities in the target gases were estimated to affect the measured cross sections by less than 1%.

Since the neutral hydrogen beam is formed by electron capture the existence of excited states in the beam must be considered. The majority of the excited states decay in the 24 inch distance between the first and second collision cells. For example, the 2p state will decay to the ground state before a 2.5 MeV particle has moved more than approximately 1 inch. The metastable 2s state has a lifetime of a few milliseconds; however, this state is quenched by a perpendicular electric field greater than 30 volts per centimeter.[54] The 2s state is, therefore, quenched by the deflection voltage used to remove all charged particles from the neutral beam. Other highly excited states may have lifetimes long enough to reach the second collision chamber; however, since the population of

excited states by electron capture is proportional to n^{-3}, the fraction of neutral particles with these highly excited states is negligible.

SECTION B. DOUBLE-ELECTRON CAPTURE CROSS SECTIONS FOR INCIDENT PROTONS IN THE ENERGY RANGE 75 TO 250 keV

CHAPTER VI

INTRODUCTION

The process of double-electron capture consists of the simultaneous transfer of two electrons from bound states in the target atom to bound states in the incident particle. The double-electron capture cross sections for incident protons are particularly interesting due to the simplicity of the system. The incident proton and outgoing negative hydrogen ion exist only in the ground state, thus removing many difficulties normally encountered in theoretical computations. Calculations of the double-electron capture cross sections ($\sigma_{1\bar{1}}$) have been made by Mittleman[55] for protons incident on a molecular hydrogen target. Gerasimenko[56] and Rosentsveig and Gerasimenko[57] have calculated cross sections for double-electron capture from helium targets. The majority of the experimental results have been obtained for proton energies less than 65 keV; however, Williams[46] has measured $\sigma_{1\bar{1}}$ for protons in hydrogen in the energy range of 400 to 1000 keV and Schryber[48] has measured $\sigma_{1\bar{1}}$ for protons in helium, argon, and nitrogen at energies of 585 and 750 keV. In the present work the double-electron capture cross sections are obtained for energies at which

the Born approximation is expected to be valid. For most practical purposes this region is reached for incident proton energies greater than approximately 100 keV.[56] The results of the measurement of double-electron capture cross sections for the target gases H_2, He, Ar, Kr, N_2, and H_2O for incident protons with energies in the range 75 to 250 keV are presented later in this section.

CHAPTER VII

THEORY

Two different theoretical approaches have been made to the calculation of double-electron capture cross sections. The first is a Born approximation of the type applied to single-electron capture. This calculation has the difficulty of a lack of orthogonality of initial and final states. The second approach has been the application of the impact parameter formulation. This approach is found to give much better agreement with experimental results.

A. Born Approximation

The integral cross sections for simultaneous capture of two electrons by protons from helium were calculated in the first Born approximation by Gerasimenko.[56] Approximate wave functions Ψ and ϕ were used for the ground states of hydrogen and helium, respectively. The wave functions were taken to be

$$\Psi = \left(\frac{Z^3}{\pi}\right)^2 e^{-Z(\underline{r}_1 + \underline{r}_2)} \quad ; \quad \phi = \left(\frac{Z'^3}{\pi}\right)^2 e^{-Z'(\underline{P}_1 + \underline{P}_2)} \qquad (45)(46)$$

where $Z = 0.69$ and $Z' = 1.69$; $\underline{r}_1$ and $\underline{r}_2$ are radius vectors of the electrons relative to the proton and $\underline{P}_1$ and $\underline{P}_2$ are radius vectors of the electrons

relative to the α-particle. The scattering amplitudes were reduced to a form convenient for numerical integration. The results obtained in this calculation are nearly a factor of 100 larger than the corresponding measured values.

B. Impact-Parameter Formulation

The Born approximation used in double-electron capture calculations has been shown by Mittleman[58] to be seriously in error because of the lack of orthogonality of the non-interacting initial and final states. In order to overcome this non-orthogonality, Mittleman[55] applied a modification of a Hartree-Fock approximation which he described in reference 58. This approximation had the property that the first Born approximation vanished when the correlation of the two transferred particles was neglected. This expresses the obvious physical effect that it takes at least two perturbing interactions to make two uncorrelated particles change state, so that in the first approximation the Born result should vanish. Therefore one would need to go to the second order Born terms in order to get a nonvanishing result. Rather than do this Mittleman employed a simpler, but equivalent, method in which the two-particle amplitude is obtained as a product of two one-particle exchange amplitudes. This method was applied to the reaction

$$H^+ + H_2 \rightarrow H^- + 2H^+ \qquad (47)$$

The correlation of the two electrons was neglected and simple forms of the potential for electrons in H_2 and H^- were used in place of the Hartree-Fock potentials. With these approximations and approximate ground state wave functions for H_2 and H^- the problem can be reduced to one of calculating single-particle exchange amplitudes. These single-particle exchange amplitudes can be evaluated in many ways and Mittleman evaluates them in two different ways.

One method of evaluation is the simple Born approximation analogous to the Brinkman-Kramers calculation of protons on hydrogen. Either the initial or final perturbation could be used; however, the results would not be the same since the exact bound state wave functions are not used. Mittleman used the initial perturbation in his evaluation of this Born amplitude.

Another method[55] for evaluation of the one-particle exchange amplitude is a form of the Born approximation in which V_i is replaced by the commutator $[V_i, \pi_i]$ where π_i is a projection operator onto the initial states. This has the effect of correcting for the lack of orthogonality of initial and final states. The cross sections calculated in this "modified" way are smaller than those of the simple Born approximation and more nearly in agreement with experimental results as is shown in the next chapter. It should be noted that the results of this impact-parameter formulation are expected to be poor for incident proton energies less than 50 keV.

CHAPTER VIII

EXPERIMENTAL METHOD AND RESULTS

A simple mathematical description of the double-electron capture process is very similar to that previously described (section B of Chapter III) for single-electron capture. The changes in the charge state of an initially pure proton beam as it interacts with a target gas are given by Equations (20, 21, and 22) of Chapter III. If one considers "thin" target conditions and the initial conditions $F_o = F_{\bar{1}} = 0$ and $F_1 = 1$, these equations can be reduced to:

$$dF_1 = -F_1 \sigma_{1\bar{1}} d\pi - F_1 \sigma_{10} d\pi \tag{48}$$

$$dF_o = F_1 \sigma_{10} d\pi \tag{49}$$

$$dF_{\bar{1}} = F_1 \sigma_{1\bar{1}} d\pi \quad . \tag{50}$$

The growth by charge transfer of the negative ion component in the proton beam is given by

$$\frac{dF_{\bar{1}}}{d\pi} = F_1 \sigma_{1\bar{1}} \quad . \tag{51}$$

Equation (51) may be easily solved to give

$$F_{\bar{1}} = \sigma_{1\bar{1}} \pi = \sigma_{1\bar{1}} \alpha P \tag{52}$$

where

$$\alpha P = 9.90 \times 10^{15}\ P(\text{mm})\ \ell(\text{cm})\ T^{-1}(^{\circ}K)$$

P = target gas pressure in torr

ℓ = target cell path length in centimeters

T = absolute temperature of the target gas in degrees Kelvin.

Thus, for "thin" target conditions one can determine $\sigma_{1\bar{1}}$ from the slope of the straight line which results from a plot of $F_{\bar{1}}$ versus P in the same manner as was described in section C of Chapter II for single-electron capture and loss. However, if the target density becomes high enough for secondary collisions to occur within the collision cell one must solve the three component equations [Equations (20, 21, and 23) of Chapter III] for a complete description of the process. When one considers the possible occurrence of secondary collisions, the solution to the complete three component differential equations can be written in the form

$$F_{\bar{1}} = \sigma_{1\bar{1}}\ \alpha\ P + \chi\ P^2 \qquad (53)$$

where χ includes the cross sections σ_{10}, $\sigma_{1\bar{1}}$, $\sigma_{0\bar{1}}$, $\sigma_{\bar{1}1}$, and $\sigma_{\bar{1}0}$, and has been evaluated by Fogel.[59] Therefore, the onset of multiple collisions can be recognized by the appearance of a quadratic shape in a plot of $F_{\bar{1}}$ versus P. In Figure 22, the linear and quadratic regions indicated by Equation (53) can be easily seen. The measured values for the double-electron capture cross sections were obtained from the slope of the linear portion of the $F_{\bar{1}}$

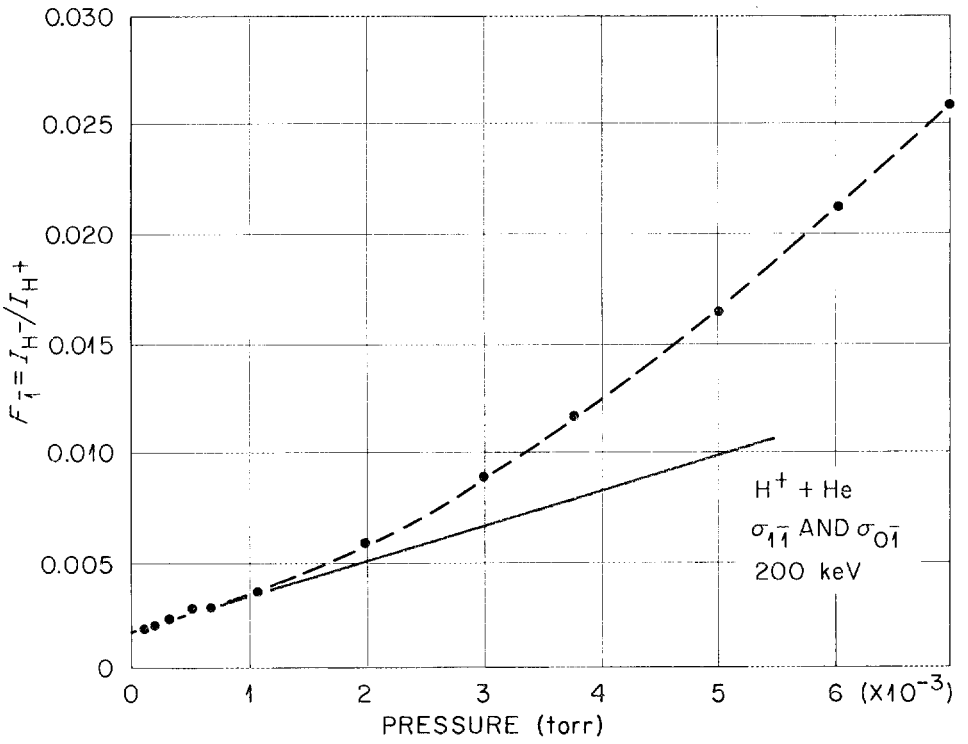

Fig. 22. An example of the increase in the ratio I_{H^-}/I_{H^+} with an increase in target gas pressure.

versus P plots. Since the slope was determined from data taken with target gas pressures less than 6×10^{-4} torr, the contribution to the slope due to secondary collisions was considered negligible. In each case enough data were plotted to see the onset of the quadratic portion of the curve; in this way we were confident that the straight line portion of the curve, used for cross section calculations, was well separated from the quadratic portion.

The apparatus used for the measurement of F_{-} as a function of proton energy and gas density is the same as was described in Chapter III and shown schematically in Figure 1. The short path length collision cell was used and the collision cell wall temperature was measured by an iron-constantan thermocouple taped to the cell wall. The value of α in Equation (52) was calculated to be $2.18 \times 10^{+17}$ mm^{-1}-cm^{-2}. Data were obtained by means of two different experimental configurations. The first set of data was obtained from the apparatus arranged such that the protons followed a linear path from the bending magnet through the collision cells. A second set of data was obtained with the apparatus modified by a bend of approximately 1° placed after the first two apertures. This slight bend removed the neutral background produced by beam interactions with residual gas molecules and defining apertures between the analyzing magnet and the entrance to the collision cell. The protons were bent by the electric field produced by the first set of electrostatic deflection plates into the collision chamber. The results obtained from

the two experimental configurations were averaged together and are quoted in Table 6. The uncertainties in these values vary from 8% for the larger cross sections to nearly 20% for the smaller. This large uncertainty is due primarily to small signal-to-noise ratios involved in measuring the small cross sections.

In Figure 23 the double-electron capture cross sections for protons on hydrogen are compared with previous experimental and theoretical results. There are no previous experimental results in the energy range of the present work; however the present results join smoothly at both low and high energies with the results of Williams.[46,60] The measured values obtained for impact energies less than 60 keV by McClure[61] and Fogel et al.,[62] which are in close agreement with the data of Williams, were omitted to preserve clarity in the drawing. The theoretical results of Mittleman[55] are in wide disagreement with the experimental work. Although the "corrected" results of Mittleman are still much larger than the measured values at energies above 100 keV, the correction for non-orthogonality of initial and final state wave functions applied by Mittleman in the "corrected" calculation is a step toward agreement with experimental results.

The cross sections for double-electron capture by protons on helium are shown in Figure 24. The measured cross sections reported by Williams,[60] Fogel et al.,[62] and Schryber[48] for impact energies less than

TABLE 6

DOUBLE-ELECTRON CAPTURE CROSS SECTIONS

Proton Energy (keV)	Cross Section Per Molecule — Target Gas		
	H_2	He	Ar
75	$(7.97 \pm 0.78) \times 10^{-20}$	$(9.27 \pm 0.75) \times 10^{-20}$	----
100	$(1.73 \pm 0.18) \times 10^{-20}$	$(3.29 \pm 0.26) \times 10^{-20}$	$(1.14 \pm 0.09) \times 10^{-19}$
125	$(3.08 \pm 0.38) \times 10^{-21}$	$(1.02 \pm 0.08) \times 10^{-20}$	$(2.95 \pm 0.24) \times 10^{-20}$
150	$(9.18 \pm 1.50) \times 10^{-21}$	$(3.80 \pm 0.45) \times 10^{-21}$	$(1.00 \pm 0.09) \times 10^{-20}$
175	$(1.82 \pm 0.23) \times 10^{-22}$	$(1.49 \pm 0.25) \times 10^{-21}$	----
200	$(9.1 \pm 2.1) \times 10^{-23}$	$(7.12 \pm 1.18) \times 10^{-22}$	$(1.73 \pm 0.37) \times 10^{-21}$
225	----	----	----
250	----	----	----

TABLE 6 (cont.)

Proton Energy (keV)	Cross Section Per Molecule — Target Gas		
	Kr	N_2	H_2O
75	----	----	----
100	$(1.66 \pm 0.15) \times 10^{-19}$	$(1.86 \pm 0.15) \times 10^{-19}$	$(1.68 \pm 0.13) \times 10^{-19}$
125	$(3.65 \pm 0.30) \times 10^{-20}$	$(7.63 \pm 0.61) \times 10^{-20}$	----
150	$(8.53 \pm 0.68) \times 10^{-21}$	$(2.36 \pm 0.19) \times 10^{-20}$	$(2.25 \pm 0.18) \times 10^{-20}$
175	----	----	----
200	$(1.07 \pm 0.08) \times 10^{-21}$	$(5.06 \pm 0.40) \times 10^{-21}$	$(4.05 \pm 0.32) \times 10^{-21}$
225	----	----	----
250	----	$(1.05 \pm 0.08) \times 10^{-21}$	$(1.05 \pm 0.08) \times 10^{-21}$

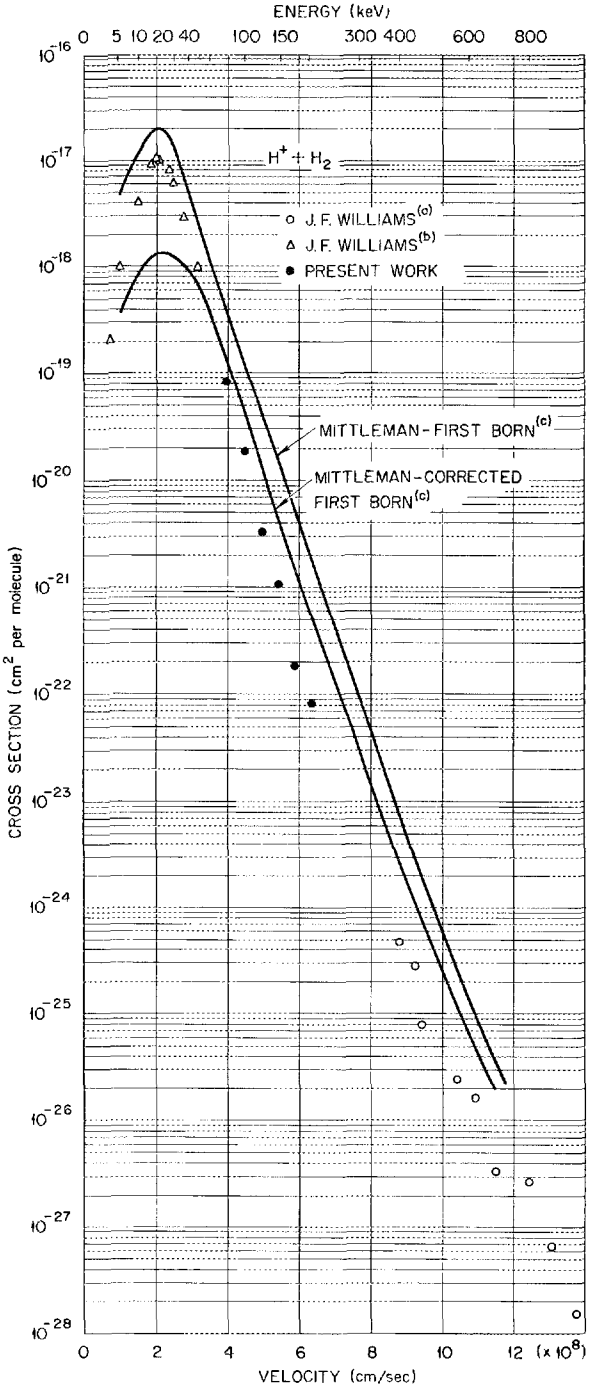

Fig. 23. The double-electron capture cross sections for protons on hydrogen with previous experimental and theoretical results. Experimental results: (a) see reference 60 and (b) see reference 46. Theoretical results: (c) see reference 55.

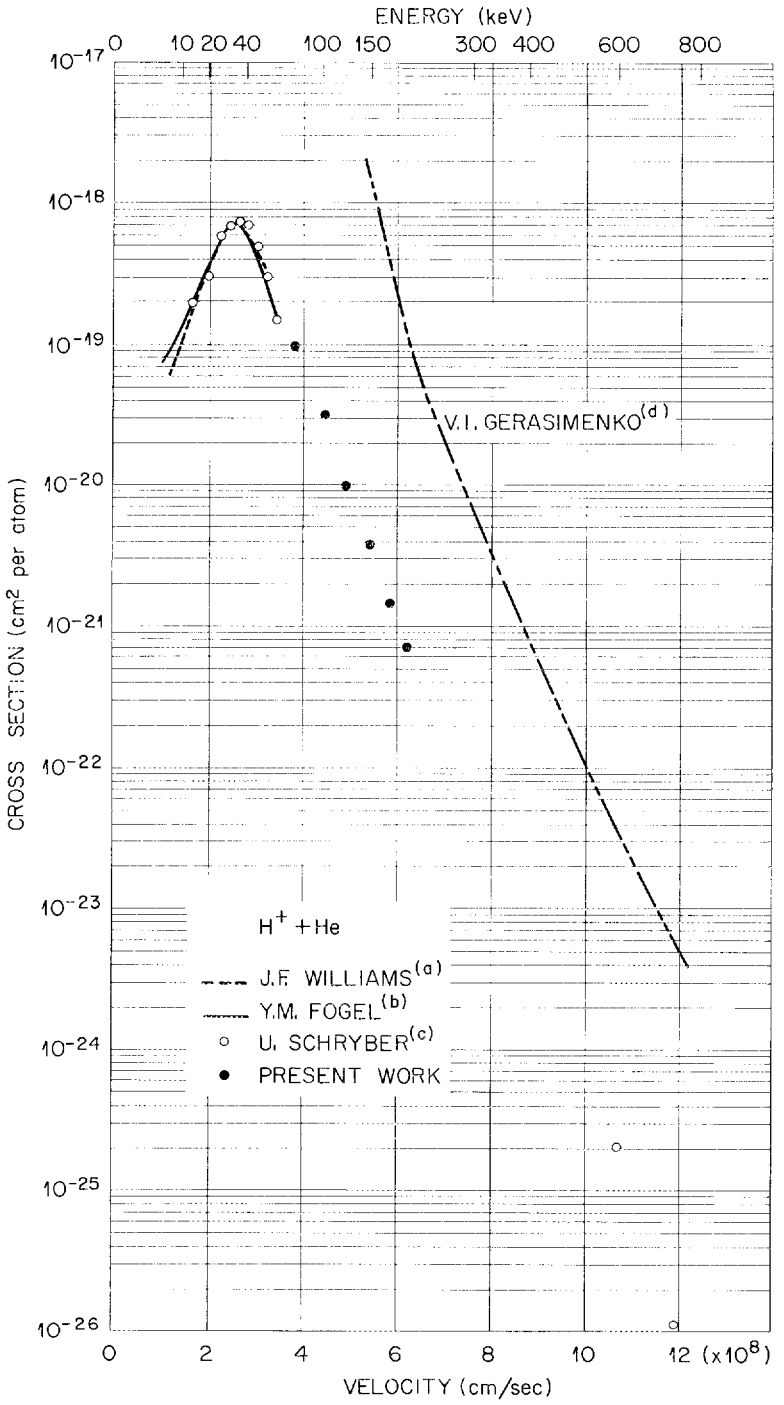

Fig. 24. The double-electron capture cross sections for protons on helium with previous experimental and theoretical results. Experimental results: (a) see reference 60, (b) see reference 62, and (c) see reference 48. Theoretical results: (d) see reference 56.

65 keV are in close agreement and join smoothly with the results of the present measurements. If the present results are extrapolated to higher energies the extrapolation would pass in close agreement with the results of Schryber[48] at proton energies of 585 and 750 keV. The only theoretical predictions in the energy range of the present work are due to Gerasimenko.[56] The results of his first Born calculation are more than 100 times greater than the measured values.

Figure 25 shows the double-electron capture cross sections for protons on argon. This is the only target gas for which previous measurements have been reported in the energy range of the present work. The agreement between these previous measurements of Afrosimov et al.[63] and the results of the present work is excellent. There is, however, considerable scatter among the various measurements at impact energies less than approximately 40 keV. Also, the results of Schryber[48] for incident proton energies of 585 and 750 keV appear to be larger than would be suggested by an extrapolation of the present results to these energies.

Figure 26 shows the present work obtained for protons on krypton in the energy range of 100 to 200 keV and previous measurements for energies less than 60 keV. The present measurements join smoothly with the low-energy measurements of Williams[60] and Fogel et al.[62]

Schryber[48] has measured cross sections for double-electron capture by protons on nitrogen. His measurements were for incident proton

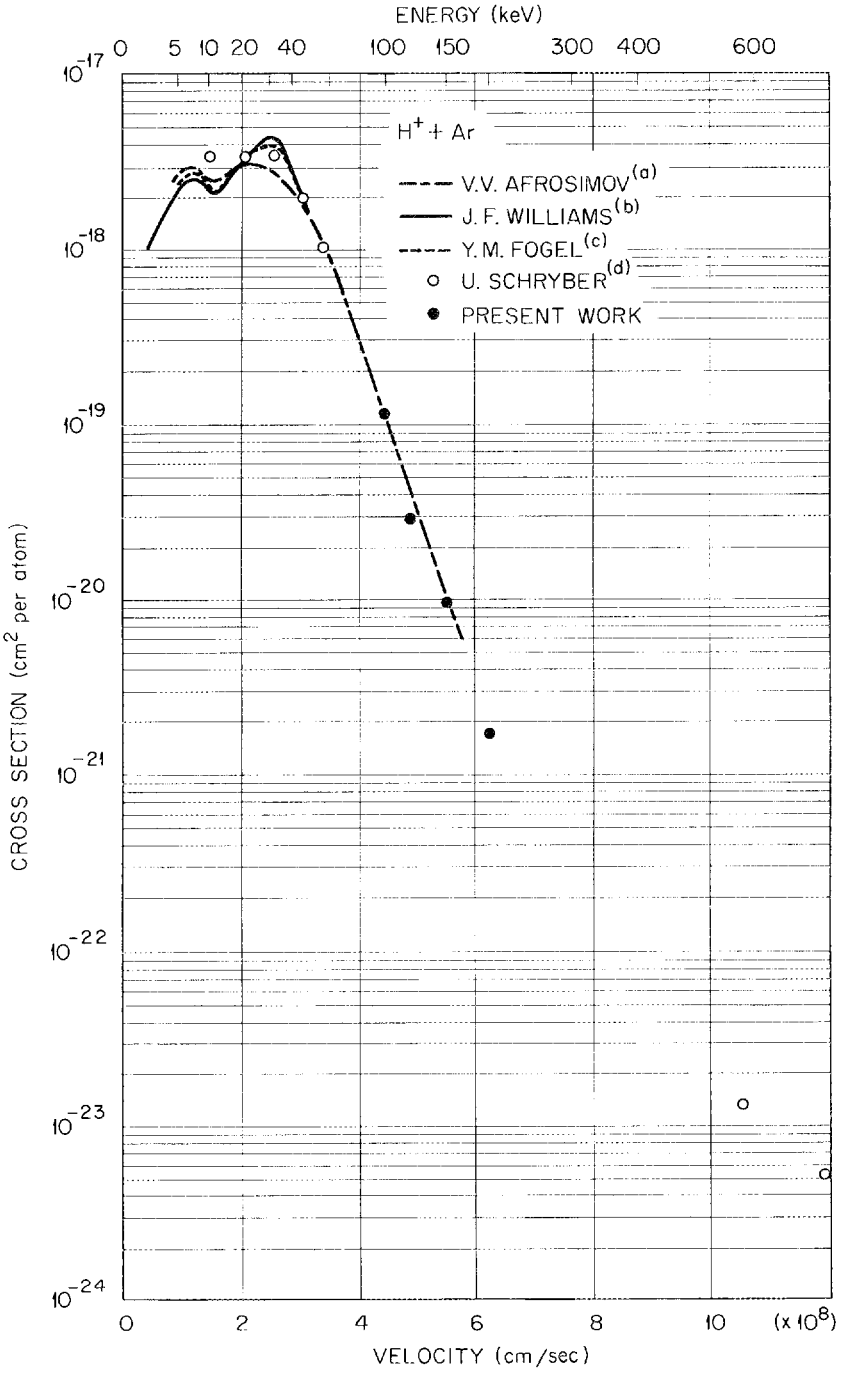

Fig. 25. The double-electron capture cross sections for protons on argon with previous experimental results. Experimental results: (a) see reference 63, (b) see reference 60, (c) see reference 62, and (d) see reference 48.

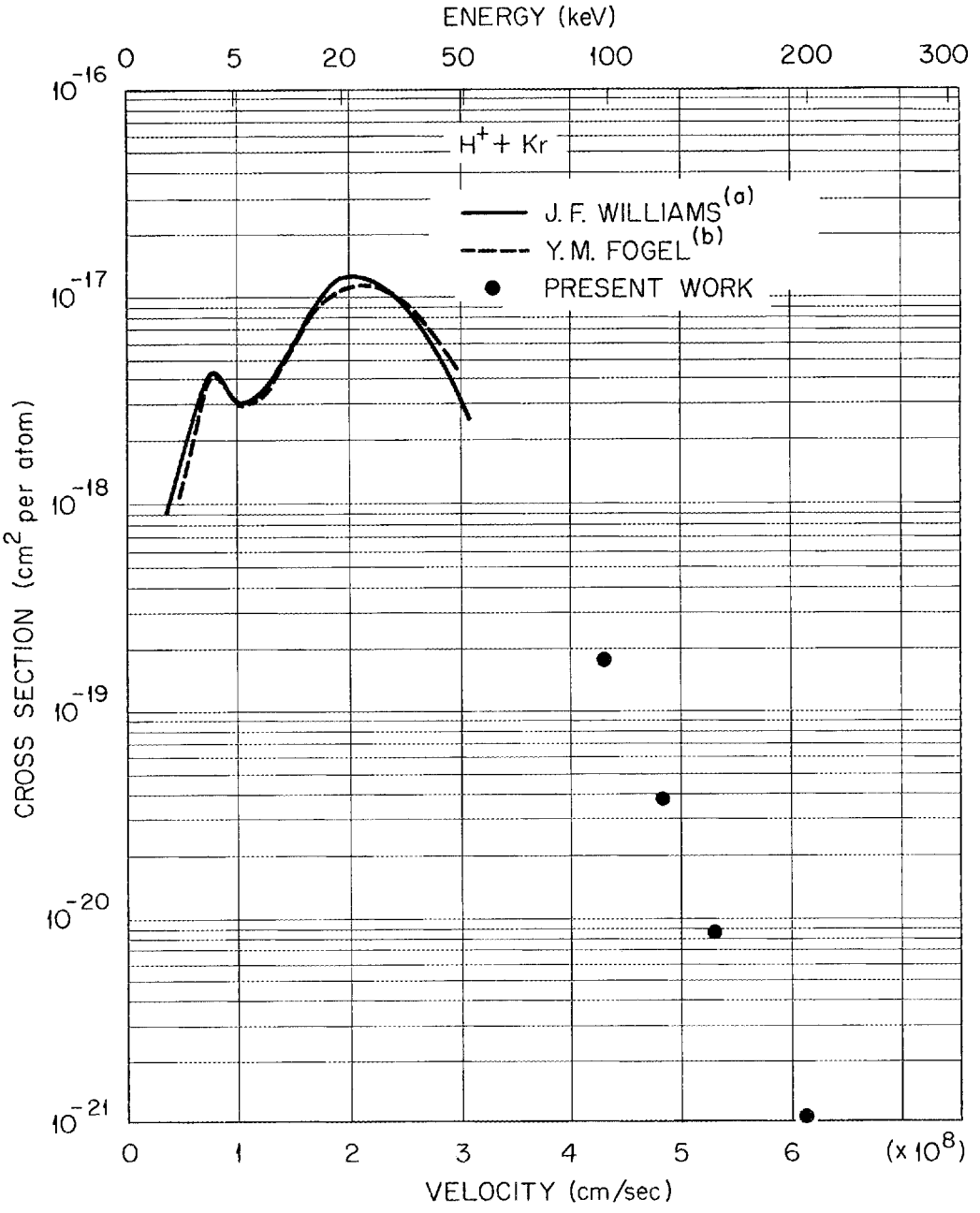

Fig. 26. The double-electron capture cross sections for protons on krypton with previous experimental results. Experimental results: (a) see reference 60 and (b) see reference 62.

energies of 10 to 30 keV and 585 and 750 keV. Figure 27 shows the results of Schryber and the results of the present measurements. These two sets of measurements join smoothly at low energies; however, an extrapolation of the present results to higher energies would suggest smaller values than were measured at 585 and 750 keV by Schryber.

There have been no previous measurements reported for double-electron capture by protons on water vapor; therefore this data is presented only in Table 6. The cross sections for water vapor are found to be very similar in value to those obtained for nitrogen.

The velocity dependences of the double-electron capture cross sections were determined from plots of $\log_{10} \sigma_{1\bar{1}}$ versus $\log_{10} E$ as are shown in Figure 28. A straight line resulting from this plot indicates that $\sigma_{1\bar{1}}$ is proportional to v^{-k} where k is a constant and is determined from the slope of the line. As can be seen in Figure 28, a straight line is not obtained for all target gases throughout the energy range studied. However, with the exception for hydrogen, the gases studied in this work all exhibited a straight line at energies greater than 100 keV. The velocity dependences calculated from the straight line portions of these plots are given in Table 7; the velocity dependence for hydrogen was estimated from the curved line. The double-electron cross sections for each target gas were found to vary approximately as v^{-12} for the energy range studied.

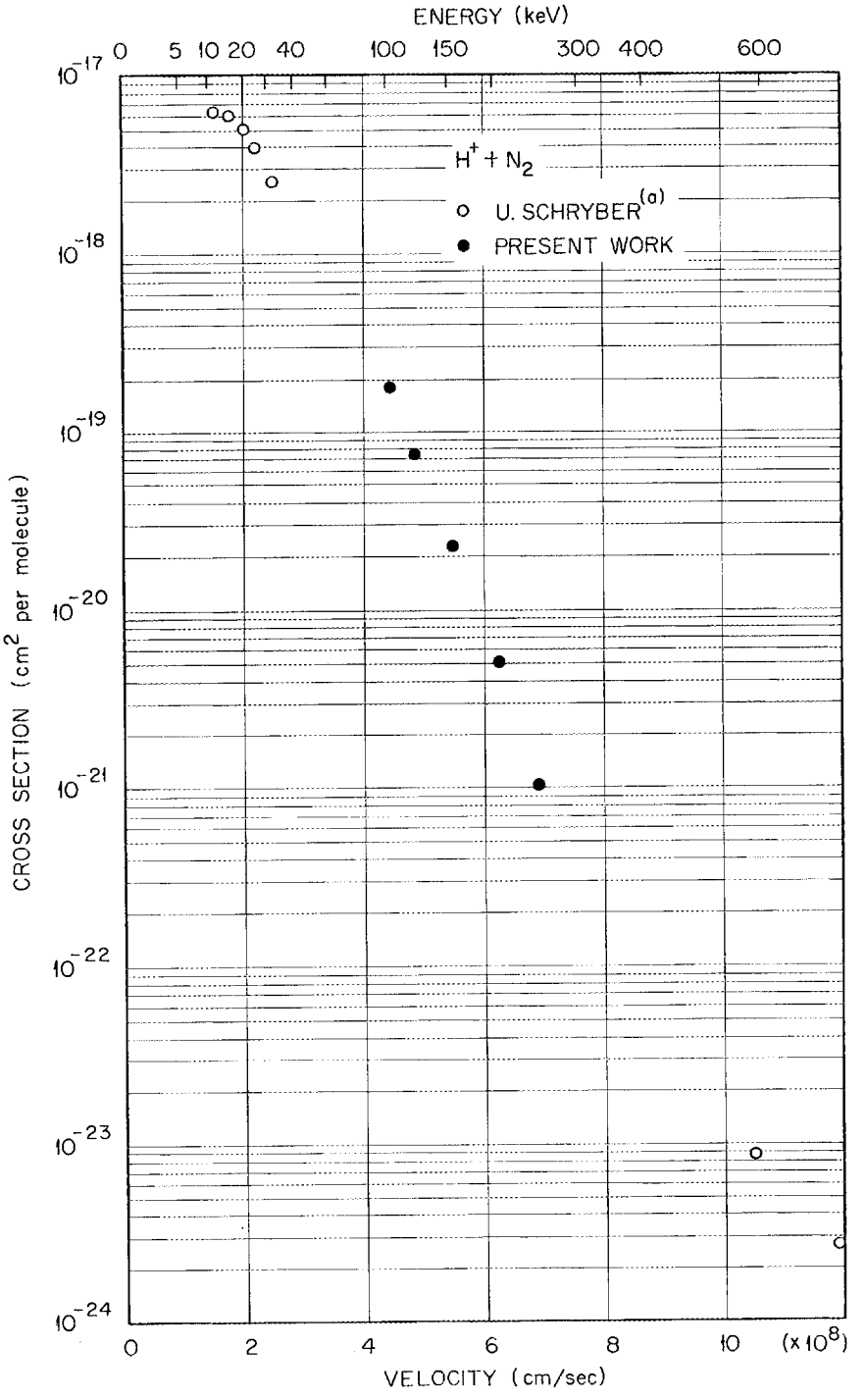

Fig. 27. The double-electron capture cross sections for protons on nitrogen with previous experimental results. Experimental results: (a) see reference 48.

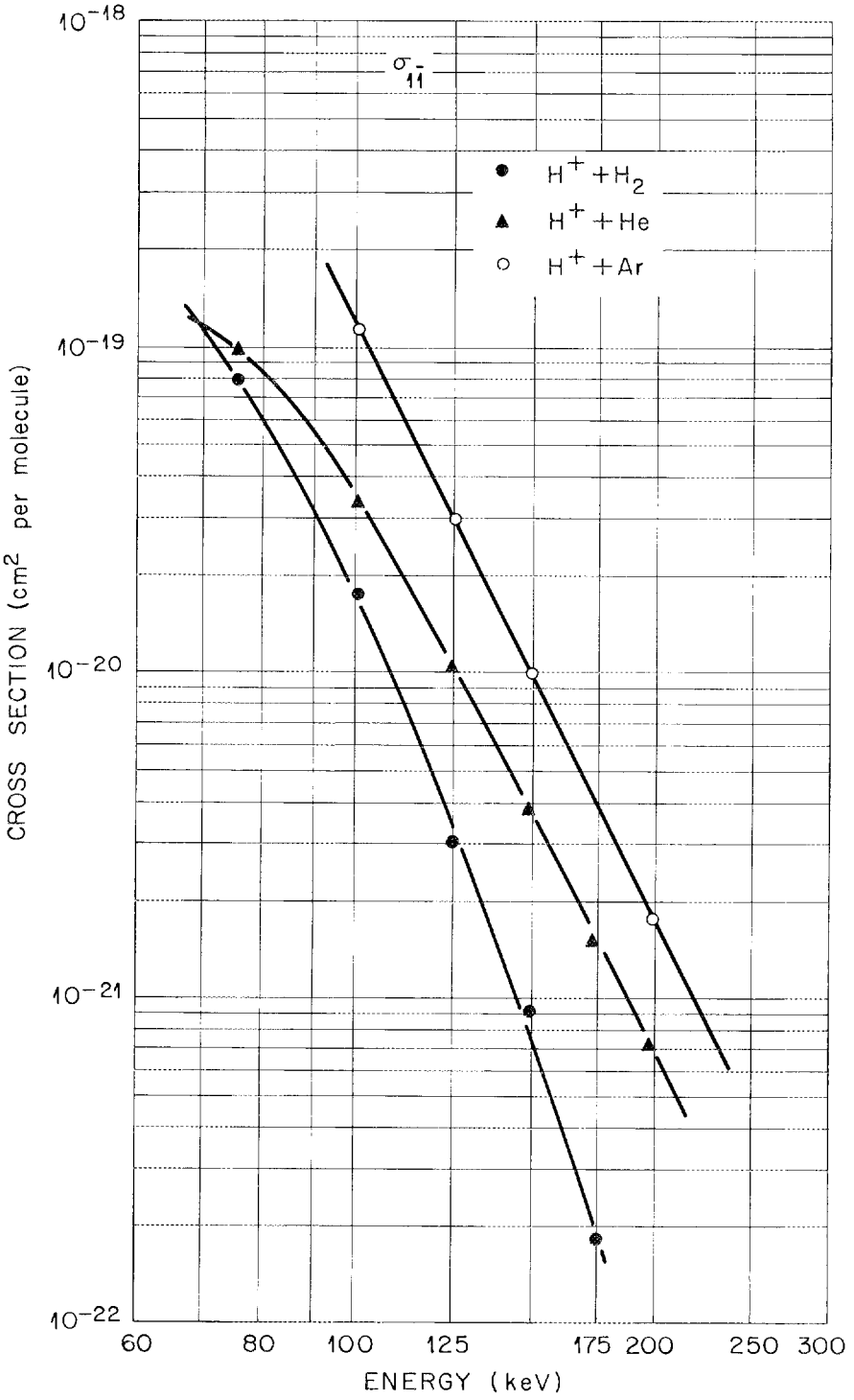

Fig. 28. The $\log_{10}$ of the double-electron capture cross sections versus the $\log_{10}$ of the incident proton energy for the target gases hydrogen, helium, and argon.

TABLE 7

VELOCITY DEPENDENCE OF THE
DOUBLE-ELECTRON CAPTURE CROSS SECTIONS

Target Gas	H_2	He	Ar	Kr	N_2 H_2O
Velocity dependence	$v^{-15} \rightarrow v^{-12}$	$v^{-11.8}$	$v^{-12.2}$	$v^{-14.6}$	v^{-12}

CHAPTER IX

ACCURACY AND VALIDITY OF THE MEASUREMENTS

The error limits associated with the double-electron capture cross sections are a result of the same experimental uncertainties as were described in Chapter V for single-electron transfer. One basic difference in the determination of limits of uncertainties for the double-electron capture cross sections is the much greater statistical uncertainties involved in the determination of beam intensities. Due to the very small cross sections at higher energies, the signal-to-noise ratio is quite small. This small signal-to-noise ratio becomes the dominant feature in the uncertainties associated with these cross sections. In several cases three or four measurements of the cross sections were made. The error limits assigned to the cross sections are based on the reproducibility of the measured values. The error limits assigned are from $\pm$ 8% for the largest double-electron capture cross section to $\pm$ 20% for the smaller cross sections. These uncertainties include the variations in the measured values obtained in several scans as well as the instrumental uncertainties previously discussed.

CHAPTER X

CONCLUSIONS

The measured cross sections for single-electron transfer have been compared to the existing theoretical and experimental values. The present work was found to be in close agreement with previous measurements. Agreement between the present work and the Born estimates of the electron capture cross sections calculated by Mapleton and by Nikolaev is found to be quite good. However, discrepancies between experimental cross sections and the values calculated by impulse and impact parameter calculations occur at energies above a few hundred kilovolts. The predictions by Mapleton and by Nikolaev of capture from inner electron shells is found to be in qualitative agreement with structure found in the experimental capture cross sections of argon, krypton, and nitrogen. This structure is also noted for the hydrocarbon gases studied as was seen in the variance of the velocity dependence of the cross sections.

The asymptotic velocity dependences for single-electron capture and loss are found to be in qualitative agreement with the predictions of Bohr. The $v^{-10.6}$ dependence found for the cross sections for electron capture by protons from hydrogen measured in this work is similar to the v^{-11} dependence calculated by distorted wave and second order Born approximations

as the asymptotic dependence at high energies. It was not expected that this asymptotic velocity dependence should be obtained at the low energies of the present measurements.

An application of the sum rule for the determination of molecular cross sections was found to give semi-quantitative agreement for the various carbon-containing molecules studied in this work. Although this sum rule may be used for approximate calculations, the role of molecular forces on the total molecular cross section was demonstrated at energies as high as 2.5 MeV.

The double-electron capture cross sections measured in this work are found to join smoothly with previously measured values at lower energies. The theoretical predictions, which exist only for hydrogen and helium targets, are in wide disagreement with the measured values. The modification of the calculation for hydrogen cross sections which includes corrections for the non-orthogonality of the wave functions is found to bring the theoretical values closer to the measured values.

PART II. THE K-, L- AND M-, AUGER, L-COSTER-KRONIG, AND THE CONVERSION-ELECTRON SPECTRA OF PLATINUM IN THE DECAY OF ^{195}Au

CHAPTER XI

INTRODUCTION

Within the past few years there has been a renewed interest in the investigation of the Auger effect and low-energy electron spectroscopy in general. This interest has been brought about on the one hand by developments in the field of high resolution electron spectrometers, by new methods for the preparation of "mass-free" radioactive sources, and by new methods for the detection of very-low-energy electrons, and on the other hand by recent progress in theoretical work. The scarcity of experimental data in the area of L-Auger and Coster-Kronig spectra has prompted the present study of the L-Auger and Coster-Kronig spectra of platinum. It is hoped that this work will help provide incentive for the laborius calculation of theoretical Auger intensities for the region of intermediate atomic numbers.

Much experimental and theoretical work has been published on the K-Auger process. The application of an intermediate coupling scheme to this process has resulted in the prediction of satellite lines associated with several K-Auger transitions. The satellite lines have been observed for elements with atomic numbers near Z = 50; however these lines have not been reported for atomic numbers as high as Z = 78. The K-Auger

studies in the decay of ^{195}Au presented in this work were recorded at high resolution in order to compare the experimental results to existing theoretical predictions.

The decay scheme of ^{195}Au is well established with respect to the spins and parities of the excited states of ^{195}Pt. However, recent publications do not agree on values for the electron capture branching ratios. In this work, the branching ratios are investigated by means of the measured conversion-electron spectra with the hope of resolving these discrepancies. The conversion-electron line intensities may also be used to assign multipolarities to the gamma-ray transitions in ^{195}Pt.

Considerable interest has developed in recent years in the comparison of relative intensities of L-subshell conversion-electrons which have been measured to those which have been deduced from theoretically calculated conversion coefficients. Discrepancies have been found not only between theoretical and experimental L-subshell intensity ratios, but also between ratios deduced from theoretical values of different authors. These discrepancies between theoretical values are believed to be related to nuclear structure effects which are only approximately accounted for in the calculations. In the present work the conversion-electron line intensities were used in the calculation of conversion coefficients, in the investigation of the electron capture branching ratios, and in the comparison of experimental L-subshell ratios to those deduced from theory.

CHAPTER XII

THEORY

A. The Auger Effect

When a neutral atom is ionized in an inner shell the initial vacancy is filled by an electron from one of the higher (less tightly bound) levels in a time of $10^{-17} - 10^{-14}$ seconds. The atom then possesses an excess energy equal to the difference in the ionization energy of the two levels. This excess energy may be carried off either by the emission of a photon or the ejection of an electron from an outer shell. The latter process is called the Auger process and the ejected electron is called an Auger electron after the French physicist Pierre Auger who first observed these electrons. Auger first noted this process through paired tracks obtained in a Wilson expansion chamber which contained inert gases ionized by a beam of X-rays (for a historical review see reference 64).

Knowledge of the energies and intensities of Auger electrons is important for the evaluation of the usefulness of particular atomic coupling schemes used in atomic calculations. The observation of satellite lines in the K-Auger process was evidence of the validity of the use of intermediate coupling. From an experimental point of view, knowledge of the energies and intensities of Auger electrons is necessary

both to differentiate internal-conversion electrons and β-particles from Auger electrons and to determine the number of initial electron vacancies from the number of Auger electrons. Knowledge of the number of initial vacancies is useful in the investigation of nuclear decay schemes, particularly those of electron capture isotopes. Auger lines can also be used for energy calibration in the low-energy region where several line energies are known with an accuracy of 5 parts in 10^4.

Auger transitions are classified in groups according to the electron shell in which the initial vacancy occurs. If the initial vacancy is produced in the K-shell, the resulting transition is a K-Auger transition and initial L-shell vacancies result in L-Auger transitions, etc. Following the Auger transition the atom has two vacancies in its electronic structure. The initial vacancy plus the two final vacancies define a particular Auger transition; for example the transition KL_1L_2 is a K-Auger transition with final vacancies in the L_1 and L_2 subshells. Transitions written as KL_1L_3 and KL_3L_1 are considered identical as is required by energy conservation. L-Auger electrons correspond to processes of the type $L_oX_pY_q$, where the initial vacancy is in the L_o subshell and final vacancies are in the X_p and Y_q subshells, X and Y being any shell higher than L and the subscripts o, p, q denote particular subshell. An Auger transition may be described in general as $V_oX_pY_q$. In this notation V and o designate the electron shell and subshell, respectively, in which the initial vacancy occurred. The $L_oL_pX_q$ transitions

are a special type of L-Auger transition called Coster-Kronig transitions. Coster-Kronig transitions are energetically possible only in a limited region of the periodic table.

The above classification of Auger lines is not completely satisfactory. One might interpret the Auger process in this way as an inner atomic photo-effect of X-rays. However, this interpretation meets with difficulty in that KL_1 radiative transitions are forbidden by the selection rule $\Delta\ell = \pm 1$, whereas KL_1Y_q Auger transitions are observed. Furthermore, according to the $V_oX_pY_q$ notation, there should be six lines in the KLL group: KL_1L_1, KL_2L_2, KL_3L_3, KL_1L_2, KL_1L_3, and K_2L_3; however the actual number of KLL lines has been found experimentally to be as many as nine. This difficulty in designating Auger lines is brought about by the assignment of definite values to o, p, and q which implies that the total angular momentum of the individual electrons in the X and Y shells is a good quantum number. The total angular momentum of the individual electrons is a good quantum number only in the j-j coupling scheme which is valid for heavy elements. For elements of low atomic number the final states are described by L and S, where $L = \ell_1 + \ell_2$ and $S = s_1 + s_2$. This description of the L-S or Russell-Saunders coupling scheme which results from strong coupling between the ℓ_i themselves and between the s_i themselves with weak coupling between total L and S.[65,66]

In order to account for all of the Auger lines observed when high resolution spectroscopy is applied to Auger spectra of elements of intermediate atomic number, an intermediate coupling scheme must be employed. This coupling scheme allows for states not allowed in pure L-S coupling by considering a linear combination of Russell-Saunders functions. The additional lines are very weak and the intermediate coupling states merge smoothly into L-S states at low Z or into j-j coupling states at high Z.

The energies of K-Auger lines have been calculated by Asaad and Burhop[67] and more recently by Hörnfeldt.[68] A nonrelativistic, intermediate coupling theory was applied. Screening was included by a factor $(Z - Z_s)$ where Z_s is the screening constant. The two calculations differ in the manner in which relativistic effects were included. Asaad and Burhop included a factor $(1 - \alpha Z^2)$ while Hörnfeldt included the factor $(1 - \beta Z^3)$ to account for the Z dependence of the relativistic effects. The values for α and β were selected to obtain agreement with experimental work at a given value of Z. The results of these two authors differ very little; however, somewhat better agreement with experiment is obtained by Hörnfeldt.

When accurate calculations of Auger energies are not available, such as for energies of L-Auger transitions, an approximate method for calculating the energies is used. The approximate kinetic energy of an Auger electron is given by

$$E(V_o X_p Y_q) = E(V_o) - E(X_p) - E'(Y_q) \tag{54}$$

where $E(V_o)$ and $E(X_p)$ refer to the binding energies of the V_o and X_p electrons in the neutral atom and $E'(Y_q)$ refers to the binding energy of the Y_q electron in an atom ionized in the X_p shell. For many practical purposes $E'(Y_q)$ can be obtained from a linear interpolation between the binding energy of an electron in the Y_q shell of the neutral atom and the binding energy of an electron in the same shell of an atom with an atomic number one higher. The "effective incremental charge" ΔZ depends on the Auger group and final vacancy in question. Before the more accurate calculations of K-Auger line energies were available, Equation (54) was used to determine K-Auger energies. The values for ΔZ were found experimentally by Bergström and Hill[69] to be 0.55 for final vacancies in the L_1 and L_2 shells and 0.76 for final vacancies in the L_3 shell while Mladjenovic and Slatis[70] reported ΔZ = 0.59, 0.58, and 0.61 for final vacancies in the M_1, M_2, and M_3 shells, respectively. Equation (54) is more commonly used to calculate transition energies for the L, M, ... Auger groups, where ΔZ is taken to be one.[71]

An Auger transition is caused by the electrostatic interaction between the electron which is ejected from a bound state and the electron which fills the hole in the transition. The probability W_a for the Auger transition to occur is given by

$$W_a = \frac{2\pi}{\hbar} \sum_{if} \left| \iint \Psi_f^*(\underline{r}_1)\Psi_f^*(\underline{r}_2)V(\underline{r}_1 - \underline{r}_2)\Psi_i(\underline{r}_1)\Psi_i(\underline{r}_2)d\underline{r}_1 d\underline{r}_2 \right|^2 \qquad (55)$$

where $\Psi_i(\underline{r}_1)$ is the Schroedinger wave function of the first electron in its initial state and $\Psi_f(\underline{r}_1)$ is its wave function in the final state. Similarly, $\Psi_i(\underline{r}_2)$ and $\Psi_f(\underline{r}_2)$ are the initial and final state wave functions of the second electron. The interaction potential is $V(\underline{r}_1 - \underline{r}_2) = e^2/(\underline{r}_1 - \underline{r}_2)$.

Several calculations of KLL Auger transition probabilities have been made by Asaad and his co-workers. Their work includes a relativistic calculation which reduces to j-j coupling in the nonrelativistic limit,[72] a relativistic, intermediate coupling calculation,[73] and most recently intermediate coupling calculations which include configuration interactions.[74-76] These most recent calculations were made in an attempt to resolve discrepancies at low atomic number between experimental and theoretical KLL relative intensities (see reference 77). Listengarten[71] has also calculated the KLL Auger transition probabilities. His calculations differ from Asaad's relativistic j-j coupling calculations by the manner in which screening was considered. The KLM Auger transition probabilities have been calculated by a nonrelativistic intermediate coupling scheme by Asaad and Burhop.[67]

Very little theoretical work has been done on the L-Auger process. Rubenstein and Snyder[78,79] have applied pure Russell-Saunders (L-S) coupling to the investigation of the L-Auger spectra of the lighter elements,

argon, krypton, and silver. Asaad[80] has derived expressions for transition probabilities in j-j coupling in terms of radial integrals for initial $S_{\frac{1}{2}}$, $P_{\frac{1}{2}}$, and $P_{3/2}$ vacancies and, using the transition amplitudes of Rubenstein and Snyder, has calculated the transition probabilities for the L-Auger spectra of argon, krypton, and silver.[81]

Asaad has also calculated the transition probabilities for several Coster-Kronig transitions. In reference 82 he applied intermediate coupling to calculate the relative intensities of the $L_1L_{2,3}M_{4,5}$ transitions for Z = 29-50 and for seven other Z values from 76 to 90. He also used the j-j coupling scheme to calculate the relative intensities of the $L_1L_3M_4$ and $L_1L_3M_5$ transitions for seven atomic numbers from 76 to 90.

In order to calculate the number of initial vacancies in a given shell or subshell from a knowledge of the Auger line intensities one must know the fluorescence yield corresponding to that level. The fluorescence yield is defined as

$$\omega_y = \frac{\text{Number of Y-shell X-rays}}{\text{Number of primary Y-shell vacancies}} \tag{56}$$

and is the fraction of the initial vacancies in an electron shell which gives rise to X-rays. The Auger yield is defined in a similar way as

$$a_y = \frac{\text{Number of Y-shell Auger-electrons}}{\text{Number of primary Y-shell vacancies}} \quad . \tag{57}$$

For the simple case, when the initial vacancies are produced in the K-shell

$$a_K + \omega_K = 1 \quad . \tag{58}$$

If the K vacancies are produced only by K conversion of gamma rays, ω_K can be determined from

$$\omega_K = 1 - \frac{\text{K-Auger intensity}}{\text{K-conversion intensity}} \quad . \tag{59}$$

The determination of the L-shell fluorescence yields is complicated by the possibility of vacancy transfer between subshells by Coster-Kronig transitions. The equations for the L-shell fluorescence yield which correspond to Equation (58) for the K-shell fluorescence yield are

$$\omega_{L_1} + a_{L_1} + f_{L_1L_2} + f_{L_1L_3} = 1 \tag{60}$$

$$\omega_{L_2} + a_{L_2} + f_{L_2L_3} = 1 \tag{61}$$

$$\omega_{L_3} + a_{L_3} = 1 \tag{62}$$

where $f_{L_iL_j}$ is the relative probability that an initial L_i vacancy is filled by an L_j electron as a result of a Coster-Kronig transition.

The K-shell fluorescence yield may be calculated by means of a semi-empirical relationship due to Burhop[83]

$$\frac{\omega_K}{1 - \omega_K} = (-A + BZ - CZ^3)^4 \quad . \tag{63}$$

According to Hagedoorn and Wapstra[84] the numerical values for the constants in Equation (63) are

$$10^2\, A = 6.4, \qquad 10^2\, B = 3.40, \qquad 10^6\, C = 1.03. \tag{64)(65)(66}$$

With these constants, ω_K is given by Equation (63) with an accuracy of $\pm$ 0.005 independent of Z.

B. The Internal Conversion Process

When a nucleus is formed in an excited state for which the excitation energy is insufficient for nuclear particle emission, the dominant modes of deexcitation are electromagnetic transitions. The electromagnetic transitions are of two main types:

1) Emission of a γ-ray, of energy k and angular momentum L; where k is in units of $m_o c^2$ and L in units of $\hbar$. The angular momentum of the transition may take on any value consistent with the relationship $|J_i - J_f| \leq L \leq |J_i + J_f|$, where J_i and J_f are the angular momenta of the initial and final nuclear states.

2) Internal conversion of an orbital electron. The energy of the ejected electron is $k(m_o c^2) - E_B$ where E_B is the electron binding energy in units of $m_o c^2$ and the angular momentum of the electron is j_f. The magnitude of j_f is given as the resultant of j_i and L where L is defined above and j_i is the total angular momentum of the initial state.

The ratio of probabilities for process (2) to process (1), $\alpha = \frac{N_e}{N_\gamma}$, is called the internal conversion coefficient. The internal conversion coefficient is a function of the energy and multipolarity of the transition, the parity of

the initial and final states of the nucleus, and the atomic number of the nucleus. Because of their dependence on nuclear properties, experimentally determined conversion coefficients are useful in assigning spins and parities to nuclear states. The more subtle effects of the finite size of the nucleus may also be investigated through the study of internal conversion coefficients.

A brief description of the theory of the internal conversion process will be presented here; detailed descriptions are given in references 85 and 86.

The internal conversion process may be described as an exchange of virtual photons between the nucleus, initially in an excited state Ψ_i, and an electron, initially in a bound state Ψ_i. After this interchange the nucleus and electron are in states Ψ_f and Ψ_f, respectively, the latter referring to a continuum state. If one sums over all unobserved parameters describing the intermediate state, the transition probability may be shown to be

$$N_e = \left| e^2 \int\int d\tau_n d\tau (\underline{j}_n \cdot \underline{j} - \rho_n \rho) \frac{e^{ikr'}}{r'} \right|^2 \qquad (67)$$

where $e^2 = 1/137$; $\underline{j}_n$, $i\rho_n$ and $\underline{j}$, $i\rho$ are components of the nucleon and electron four-currents. The integration symbol over the nucleon space also implies a sum over all nucleons and $\underline{r}' = \underline{r}_n - \underline{r}$. For a Dirac particle $\underline{j} = \Psi_f^* \underline{\alpha} \Psi_i$ and $\rho = \Psi_f^* \Psi_i$ where $\underline{\alpha}$ is the Dirac velocity operator.

The evaluation of Equation (67) is carried out by expanding the Green's function in eigenfunctions of spin and parity. If the nucleus is considered as a point in space, no physical dimensions, that part of the transition matrix element which contains the dynamic nucleon current 4-vector will cancel out in the ratio $\alpha = \frac{N_e}{N_\gamma}$. The conversion coefficient can then be described in terms of the interaction of the virtual photon and the electron transition 4-current. The conversion coefficient for a point nucleus has the general form

$$\alpha \propto \left| \int d\tau \underline{j} \cdot \underline{B}_L^M \right|^2 \tag{68}$$

where $\underline{B}_L^M$ is a vector potential which describes the virtual photon.

The fact that the nucleus has a finite size affects the calculated internal conversion coefficients in two ways, referred to as the static and dynamic effects. The static effect arises from a modification of the electrostatic interaction by the finite size of the nuclear charge distribution. If one assumes that the electron does not penetrate the nucleus ("no-penetration" model) then the modification of the conversion coefficient comes from the altered behavior of the electron wave functions Ψ_i and Ψ_f, especially in the region where $\underline{r} < \underline{R}$. The static effect is incorporated by applying a smeared out charge distribution in the calculation which results in the reduction of the M1 conversion coefficients; this reduction is as large as 50% for Z = 60. For other multipoles the effect of the finite extent of the nuclear charge distribution is generally negligible.

The dynamic effect of the finite size of the nucleus results from the penetration of the nucleus by the electron. In this case the ratio of matrix elements $\frac{N_e}{N_\gamma}$ is modified from Equation (68) to the following:

$$\alpha \propto \left| \int d\tau \, \underline{j} \cdot \underline{B}_L^M (1 - \lambda) \right|^2 \tag{69}$$

where λ depends on features of nuclear dynamics (such as the nucleon current 4-vectors) and requires a nuclear model. The importance of dynamic effects in internal conversion was first emphasized by Church and Weneser.[87]

The static effects due to the finite size of the nucleus have been included in calculations of the internal conversion coefficients by Sliv and Band[88]. These authors have also attempted to include dynamic effects by the assumptions that the nucleon currents are confined to the nuclear surface $\underline{j}_n(\underline{r}_n) = \delta(\underline{r}-\underline{R})$. This assumption removes the dependence on nuclear structure and the results are very similar to the "no-penetration" model. This approximation is assumed quite accurate in that the dynamic effects are expected to be important only for hindered γ-transitions. The effects of screening are found to be small (approximately 10%) for K-shell conversion; however screening effects become appreciable for conversion in higher shells. In order to incorporate the effects of screening, one need change only the radial functions. A Thomas-Fermi-Dirac potential[89] was used to account for screening effects.

Calculations for internal conversion coefficients have also been made by Rose.[90] His calculations include modifications due to the static

effect of the finite size of the nucleus; however, Rose uses a "no-penetration" model which assumes that the electron does not penetrate the nucleus. Both the treatments of Rose and of Sliv and Band regard the dynamic effect as small; thus their results should differ very little.

Due to the variations of the internal conversion coefficients with angular momentum and parity, the tabulated values may be used for determination of the character of electromagnetic transitions. A comparison of measured to theoretical conversion-electron intensity ratios can also be used to determine the multipolarity of the transition. The L-subshell ratios are much more sensitive to multipolarity admixtures than are K/L ratios and, therefore, give a more accurate indication of the character of the radiation. In Chapter XV of this work the multipolarities of the transitions in ^{195}Au are investigated by use of both Sliv and Band's and Rose's tabulated conversion coefficients.

CHAPTER XIII

EXPERIMENTAL APPARATUS

A. The Vanderbilt Spectrometer

The electron spectra reported in this work were obtained by means of the Vanderbilt iron-free, double-focusing, beta-ray spectrometer. This spectrometer has a 30 centimeter radius and is capable of momentum resolution (fwhm) better than 0.10%. A description of the spectrometer can be found in reference 91. The magnet current for the low-energy spectra ($E \lesssim 10$ keV) was supplied by a bank of lead storage batteries instead of by the electronically regulated generator. The battery-supplied current was varied manually by means of series resistors made up of various combinations of 1/8 in. steel drill rod and rheostat resistance wires.

In this way current regulation of 5 parts in 10^5 could be obtained; whereas the constancy of the generator is only 1 part in 10^3 at these low energies.

B. The Low-Energy Electron Detection System

Electrons having energies less than approximately 50 keV were detected by a post-accelerating, continuous flow, Geiger-Muller counter previously described by Mehlhorn and Albridge.[92] The counter is of the

loop-anode, end-window type and is normally operated at 4 cm gas pressure. The counter gas is a mixture of 67% - 33% argon-ethylene. The gas pressure is regulated by means of a Cartesian manostat placed between the counter and a pump that is used to maintain the gas flow. The gas flow is regulated to give a pressure of approximately 200 microns on the fore pump side of the manostat.

The detector is attached to the exit port of the spectrometer through a lucite insulator. In this way the detector can be raised to a positive potential with respect to the spectrometer walls which are at ground potential. The low-energy electrons passing out of the exit slit of the spectrometer are then accelerated by the counter potential and are better able to penetrate the counter window. The voltage for the counter walls and the anode is supplied through a potential divider by a John Fluke and Co. Model 410 A, 1 to 10 keV high voltage supply. For this work a typical counter wall voltage was 5000 volts while the anode potential was about 1100 volts positive with respect to the counter walls. Between the counter and the spectrometer exit a small negative deceleration voltage (120 V) was applied to remove very-low-energy secondary electrons. This voltage was reduced when electrons which had initial energies of less than 120 eV were analyzed.

The counter windows were made of very thin films of Zapon (a trade name for Zaponite Q Lacquer of the Glidden Paint Co.) which were supported

over the counter window by a 90% transmitting copper screen. The films were made by floating the Zapon liquid on a surface of water. Very thin windows were necessary because of the difficulties which arise when high post-acceleration voltages must be used. The films used in this work were less than 40 $\mu g\text{-}cm^{-2}$ in thickness (approximately 3 keV "cut-off") which enabled the detection of electrons of 0 and 3 keV energy with 62% and 92% transmission, respectively, when a post-acceleration voltage of 5000 volts was used. Estimations of the thickness and transmission of the Zapon films were made by comparison with electron transmission data given by Lane and Zaffarano.[93]

The operating characteristics of the post-acceleration counter have been investigated by several authors.[92, 94, 95] These investigators discovered an electron "focusing effect" in the operation of the counter which resulted in the enhancement of very-low-energy electron lines. In reference 94 it is pointed out that proper positioning of the counter entrance slit will eliminate this focusing problem. The "focusing effect" was also found to be minimized by the use of a counter window which is wider than the spectrometer exit aperture.

C. The High-Energy Electron Counter

The measurements of several electron lines with energies greater than 50 keV were made using both the counter described above and an

end-window, loop-anode, continuous gas flow, Geiger-Mueller counter described by Duncan.[96] The counter gas (67%-33% argon-ethylene mixture) is maintained at 8 cm gas pressure by a Cartesian manostat and the gas flow is monitored by means of a thermocouple gage in the vacuum line between the Cartesian manostat and a fore pump. A flow rate is maintained such that a pressure of 0.20 torr exists in this vacuum line. A counter window of Zapon film of approximately 100 $\mu g\text{-}cm^{-2}$ thickness was used. A film of this thickness is 100% transmitting to electrons with energies greater than 50 keV.[93]

CHAPTER XIV

THE ^{195}Pt, K-, L-, AND M-AUGER AND L-COSTER-KRONIG SPECTRA MEASUREMENTS

A. Introduction

Because of the inherent difficulties of low-energy electron spectroscopy, few papers have been published of experimental studies of L-Auger spectra; and the majority of this work was done with photographic recording instruments which give rather poor intensity measurements. The experimental techniques used and the results obtained in early (1925 through 1957) investigations of L-Auger spectra, which were confined to the high atomic number elements lead, bismuth, and thallium, have been reviewed by Sujkowski and Slätis.[97] They find general agreement among the energies and intensities of the strong lines, but wide variations among those of the weaker lines of the spectra. In recent years improvements in the experimental techniques of electron spectroscopy have made possible more accurate measurements of low-energy spectra. Quantitative measurements of the energies and intensities of the L-Auger lines of tellurium,[98] mercury,[99] and thallium[100] have been made by means of double-focusing spectrometers and spectrographic techniques have been used to obtain energy and intensity measurements for rhenium,[101] platinum,[102]

gold,[103] uranium,[95,104,105] neptunium,[106] and others.[107] Päschke[108] recorded the L-Auger spectrum of gold by means of a 180° spectrometer equipped with a GM counter. Electrostatic spectrometers have been used to measure the L-Auger[109] and M-Auger[110] spectra of krypton and magnetic lens spectrometers were used to record the L-Auger spectra of cesium,[111] bismuth,[112] and thallium.[112] In the present work the L-Auger spectrum of platinum has been measured with approximately 1% resolution. This work is compared with other L-Auger intensities measured for high atomic number ($Z \cong 80$) and with the theoretical values of Asaad.[81]

The electron spectrum was scanned to zero energy in order to observe the region containing Coster-Kronig transitions. The L-Coster-Kronig transitions are of interest because a recent calculation of Asaad[82] predicts these lines to be very intense. Most of the L-Coster-Kronig lines of platinum are masked by the M-Auger spectrum; however, it was possible to obtain a total L-Coster-Kronig plus M-Auger intensity and to set tentative upper limits on the intensities of two of the L-Coster-Kronig transitions.

A large amount of work, both theoretical and experimental, has been published on the KLL Auger spectra. A comprehensive review of this work is given in references 71, 113, and 114. There is good agreement among measurements for high Z ($Z \cong 80$) elements; however, Mehlhorn and Albridge[77] have pointed out discrepancies at low Z between the

non-relativistically calculated KLL relative intensities and the experimentally determined values. Recently Asaad,[74] Körber and Mehlhorn,[75] and Mehlhorn and Asaad[76] used the configuration interaction in an attempt to resolve these discrepancies at low and intermediate Z. At high Z ($Z \cong 80$), Asaad's relativistic calculations[72,73] are in agreement with experimental results. By means of the intermediate coupling scheme, Asaad and Burhop[67] have calculated the energies and intensities of KLL and KLM Auger spectra. In the present work, the energies and intensities of the KLL and KLM Auger lines of platinum were analyzed for comparison with theory and with the results of other measurements in the same Z-region.

B. Source Preparation

In order to study very-low-energy electrons the source must be as free of mass as possible to minimize energy loss by the electrons in the source itself. The ^{195}Au activity was supplied in a carrier free form from the Nuclear Science and Engineering Corporation, Pittsburgh, Pennsylvania. Electroplating was chosen as the method of depositing the cleanest possible source of ^{195}Au with the greatest efficiency. An initial source was plated onto a 54 mg-cm^{-2} platinum backing; however, this source was not usable due to a very high background which was attributed to backscattering of electrons in the platinum backing. In order to reduce this high background

a second source (1 x 20 mm^2) was prepared by electroplating the activity from a nearly neutral solution (pH ≅ 6), obtained by neutralizing the HCl with NH_4OH, onto a 630 $\mu g\text{-}cm^{-2}$ mylar film vacuum coated with approximately 10 $\mu g\text{-}cm^{-2}$ silver (the silver thickness was estimated from light transmission curves of reference 93). The plating time, current density and the pH of the plating solution which were approximately 12 min, 100 $ma\text{-}mm^{-2}$ and pH ≅ 6, respectively, proved to be critical parameters in depositing the activity before the silver backing was dissolved by the plating solution. This source was visibly clean; however, it was evident that some mass was deposited since the momentum resolution (fwhm) varied from 0.45% at 9 keV to 0.91% at 5 keV while a constant 0.2% resolution was obtained for energies above 50 keV. This mass is assumed to be inactive gold present as an impurity in the platinum target that was used to obtain ^{195}Au by (p, n) and (p, 2n) reactions.

During the first scan of the L-Auger spectrum the heating element burned out in the thermostatically regulated reference magnet. This malfunction (not immediately discovered) introduced some uncertainties into the energy calibration of the L-Auger data taken with the above source. By the time the malfunction was discovered some diffusion of the activity in the the backing had occurred making it necessary to prepare another source to check the results of the first scan. This source was electroplated from 0.1 N HCl onto a 5.4 $mg\text{-}cm^{-2}$ platinum foil. The resolution

was slightly better with this source (0.4% at 9 keV and 0.85% at 5 keV) and more accurate energy measurements were obtained; however the background was higher due to backscattering of electrons from the platinum source backing.

C. Experimental Procedure and Results

1. The L-Auger Spectrum

The L-Auger spectrum recorded from the mylar backed source is shown in Figure 29. A post-acceleration voltage of 5000 volts was used for these measurements providing approximately 100% transmission for the lowest-energy electrons (approximately 5 keV) of the spectrum. A retarding voltage of 120 volts preceded the post-accleration chamber in order to reduce the background of low-energy scattered electrons.

The $L_3M_2M_3$ line (one of the most isolated in the spectrum) was used as a standard line shape in the analysis of the first set of data. This line shape was adjusted to account for the variation of resolution with momentum. The shape correction was based on the assumption that the line is made up of a symmetric distribution of electrons that have undergone no energy loss and a distribution of electrons that have lost energy by collisions within the source. The symmetric part of the line was determined by "folding over" the high-energy side. The remaining part of the line, after subtraction of the symmetric part, was corrected for the

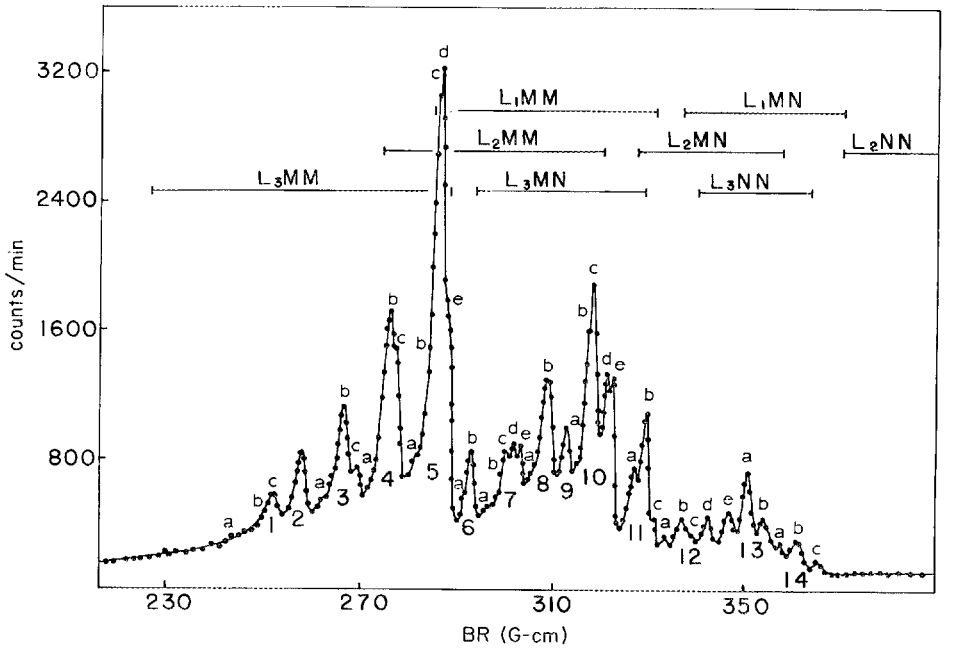

Fig. 29. The L-Auger spectrum of platinum. For clarity of reproduction not all of the experimental points are plotted.

E^{-1} dependence of electron energy loss.[115-117] This corrected energy loss spectrum was added back to the symmetric line and, if necessary, the width was altered slightly to obtain the most consistent fit to the experimental data. The $L_3M_2M_3$ standard line shape was corrected in this manner at four different energies within the L-Auger spectrum in order to account for the small variations of shape with energy.

In order to resolve the complex spectrum, a standard line shape was fitted to all lines in the spectrum, beginning with the highest energy one. Slight adjustments in line positions and heights were made so that the sum of the individual lines was the same as the experimental spectrum. The relative intensities of the lines were determined by measuring the areas by means of a planimeter and dividing the measured values by BR.

A different method of obtaining a standard line was used in the analysis of the data from the second source. We investigated the effect of the addition of ^{59}Co carrier mass on the shape of the 7.3 keV K-conversion line in the decay of ^{57}Co. Figure 30 shows the 7.3 keV K-conversion line as recorded from ^{57}Co sources containing different amounts of added ^{59}Co carrier. Although a quantitative analysis of this data was impossible due to uncertainties in the knowledge of the ratio of active to inactive cobalt atoms in the source, the various line shapes are useful in the analysis of complex line spectra. The line recorded from a ^{57}Co source that had an estimated one-to-one ratio of the inactive to active cobalt atoms fitted

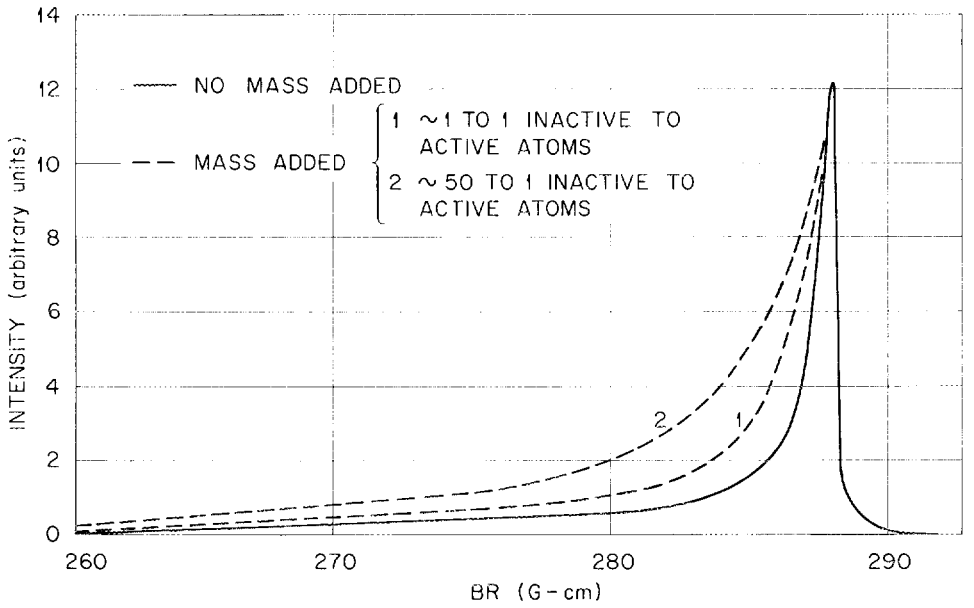

Fig. 30. The variation of line shape with carrier mass added to the source.

well the platinum L-Auger lines in the region of 9.5 keV. A plot of momentum resolution versus momentum for the L-Auger lines appeared to be linear over the energy range 5.8 to 9.5 keV; therefore the $L_3M_2M_3$ L-Auger line of platinum (an isolated line at 5.8 keV) and the 7.3 keV internal conversion line of ^{57}Co were normalized to the same peak height and plotted, and the standard line shapes for intermediate energies were then obtained by linear interpolation of these line shapes. These standard lines were then used to resolve the spectrum as described above.

A relatively long period of time elapsed (~18 months) between the first data scan from the mylar backed source and the second data scan from the platinum backed source. During this time the "focusing effect" due to the post-acceleration counter was investigated by Hall[94] and by Zender[95] with the latter author devising a method to eliminate this effect. The "focusing effect" is an enhancement of the measured intensities of the low-energy electron lines relative to those of higher energy lines which is caused by application of the post-acceleration voltage. This enhancement is more than would be expected in obtaining 100% transmission of the low-energy electrons through the counter window. The investigations of Hall and of Zender show that one can reduce or eliminate the "focusing effect" by using a counter window that is wider than the spectrometer exit aperture or by positioning the center of the counter window on the radius of curvature of the spectrometer. During the first scan of the L-Auger spectrum a 3 mm

wide counter window and a 2 mm wide exit aperture were used. Since the counter aperture was wider than the exit aperture, the "focusing effect" was expected to be negligible. For the second scan the counter window was closely centered on the radius of curvature of the spectrometer. The small variations between the intensities obtained under the two conditions were random in nature. Since centering the detector was shown by Zender to eliminate the "focusing effect", the random nature of the differences between the two scans is further evidence that the "focusing effect" was negligible during the first scan.

The intensities from the first and second scans were normalized and averaged and the results are given in Table 8. The normalization made was by an average normalization factor weighted heavily to well resolved lines. The quoted uncertainties in intensities include the differences in the results of the two measurements as well as the maximum changes in intensities which can be introduced by variations in the shape and positions of the standard lines. The measured energies reported were obtained from the second scan in which no energy drift was noted. The uncertainties in these energies, due primarily to uncertainties in the position of the standard lines within the spectrum, are approximately 0.5%. The quoted uncertainties in the energies and intensities correspond to approximately two standard deviations.

TABLE 8

ENERGIES AND RELATIVE INTENSITIES
OF THE L-AUGER TRANSITIONS OF PLATINUM

Line No.	Assignment	Energy (keV) Z = 78		Relative Intensities	
		Calculated ΔZ = 1	Measured	This work Z = 78	Theory[81] Z = 47
	$L_3M_1M_1$	4.842			0.28
1a	$L_3M_1M_2$	5.118	5.124	1.5 ± 0.8	0.28
1b	$L_3M_2M_2$	5.389	5.442	1.0 ± 0.8	0.09
1c	$L_3M_1M_3$	5.533	5.52	4.10 ± 0.35	5.75
2	$L_3M_2M_3$	5.795	5.783	12.0 ± 0.3	9.50
3a	$L_3M_1M_4$	5.976	6.014	2.3 ± 1.5	0.65
	$L_3M_1M_5$	6.061			0.59
3b	$L_3M_3M_3$	6.176	6.176	17.1 ± 1.5	14.44
3c	$L_3M_2M_4$	6.247	6.266	0.7 ± 0.7	0.81
	$L_3M_2M_5$	6.332	6.313	3.7 ± 1.0	9.0
4a	$L_2M_1M_1$	6.554	6.580	1.0 ± 0.8	0.15
4b	$L_3M_3M_4$	6.628	6.623	14.9 ± 1.0	14.10
4c	$L_3M_3M_5$	6.713	6.693	18.9 ± 0.9	23.00
5a	$L_2M_1M_2$	6.827	6.751	2.2 ± 1.6	2.88
5b	$L_3M_4M_4$	7.071	7.057	(1.4)	10.68*
5c	$L_2M_2M_2$	7.098	7.114	13.0 ± 3.0 (11.6)	2.72
5d	$L_3M_4M_5$	7.156	7.170	34.6 ± 4.0	12.62*
	$L_1M_1M_1$	7.170			2.78

TABLE 8 (cont.)

Line No.	Assignment	Energy (keV) Z = 78		Relative Intensities	
		Calculated ΔZ = 1	Measured	This work Z = 78	Theory[81] Z = 47
5e	$L_2M_1M_3$	7.233	7.224	18.4 ± 2.2	0.30
	$L_3M_5M_5$	7.236			12.14*
6a	$L_1M_1M_2$	7.446	7.462	1.0 ± 0.7	5.43
6b	$L_2M_2M_3$	7.506	7.507	7.8 ± 0.6	9.71
	$L_3M_1N_1$	7.507			0.06
7a	$L_3M_1N_2$	7.622	7.652	2.8 ± 0.8	0.03
	$L_2M_1M_4$	7.685			0.10
	$L_1M_2M_2$	7.717			0.03
	$L_3M_1N_3$	7.721			0.50
	$L_2M_1M_5$	7.770			0.59
	$L_3M_2N_1$	7.778			0.03
7b	$L_1M_1M_3$	7.852	7.833	1.9 ± 0.3	10.80
7c	$L_2M_3M_3$	7.885	7.883	2.7 ± 0.3	0.28
	$L_3M_2N_2$	7.893			0.03
7d	$L_3M_1N_4$	7.921	7.940	4.0 ± 0.7	
	$L_3M_1N_5$	7.915			
	$L_2M_2M_4$	7.956			5.37
	$L_3M_2N_3$	7.992	7.966	1.0 ± 0.4	0.81
7e	$L_2M_2M_5$	8.041	8.030	6.0 ± 0.6	10.00
8a	$L_1M_2M_3$	8.123	8.124	2.0 ± 0.7	0.53

TABLE 8 (cont.)

Line No.	Assignment	Energy (keV) Z = 78		Relative Intensities	
		Calculated ΔZ = 1	Measured	This work Z = 78	Theory[81] Z = 47
	$L_3M_1O_1$	8.157			
	$L_3M_3N_1$	8.159			0.87
	$L_3M_1N_6$	8.180			
	$L_3M_1N_7$	8.184	8.192	1.1 ± 0.6	
	$L_3M_2N_4$	8.186			
	$L_3M_1O_{2,3}$	8.196			
	$L_3M_2N_5$	8.204			
	$L_3M_1O_{4,5}$	8.263	8.249	2.0 ± 0.7	
8b	$L_3M_3N_2$	8.274			1.0
	$L_1M_1M_4$	8.304	8.299	4.9 ± 0.5	8.96
	$L_2M_3M_4$	8.337	8.342	7.7 ± 0.5	7.41
	$L_3M_3N_3$	8.373	8.370	1.6 ± 0.4	2.76
	$L_1M_1M_5$	8.389			13.50
	$L_2M_3M_5$	8.421			1.00
	$L_3M_2O_1$	8.429			
	$L_3M_2N_6$	8.451	8.433	2.0 ± 0.4	
	$L_3M_2N_7$	8.455			
	$L_3M_2O_{2,3}$	8.468			
9	$L_1M_3M_3$	8.504	8.535	5.1 ± 1.0	0.10

TABLE 8 (cont.)

Line No.	Assignment	Energy (keV) Z = 78		Relative Intensities	
		Calculated ΔZ = 1	Measured	This work Z = 78	Theory[81] Z = 47
	$L_3M_2O_{4,5}$	8.534	8.593	0.7 ± 0.2	
	$L_3M_3N_4$	8.566			
	$L_1M_2M_4$	8.575			0.31
	$L_3M_3N_5$	8.985			
	$L_3M_4N_1$	8.602			0.25
10a	$L_1M_2M_5$	8.660	8.645	1.0 ± 0.3	3.39
	$L_3M_5N_1$	8.682			0.155
	$L_3M_4N_2$	8.722	8.742	0.3 ± 0.2	0.06
10b	$L_2M_4M_4$	8.780	8.780	5.9 ± 0.8	0.18*
	$L_3M_5N_2$	8.797			0.71
	$L_3M_3O_1$	8.809	8.852	15.2 ± 0.7	
	$L_3M_4N_3$	8.816			1.30
10c	$L_3M_3N_6$	8.832			
	$L_3M_3N_7$	8.836			
	$L_3M_3O_{2,3}$	8.853			
	$L_2M_4M_5$	8.865			8.25*
	$L_3M_5N_3$	8.896	8.917	0.20 ± 0.15	2.10
	$L_3M_3O_{4,5}$	8.915	8.957	1.7 ± 0.4	
	$L_2M_5M_5$	8.945			10.50*
	$L_1M_3M_4$	8.956			4.08

TABLE 8 (cont.)

Line No.	Assignment	Energy (keV) Z = 78		Relative Intensities	
		Calculated ΔZ = 1	Measured	This work Z = 78	Theory[81] Z = 47
	$L_3M_4N_4$	9.010			
10d	$L_3M_4N_5$	9.028	9.002	6.4 ± 0.5	
	$L_1M_3M_5$	9.041			3.11
	$L_3M_5N_4$	9.090			
10e	$L_3M_5N_5$	9.108	9.070	11.3 ± 0.4	
	$L_2M_1N_1$	9.216			0.03
	$L_3M_4O_1$	9.252			
	$L_3M_4N_6$	9.275	9.216	0.65± 0.60	
	$L_3M_4N_7$	9.279			
	$L_3M_4O_{2,3}$	9.296			
11a	$L_2M_1N_2$	9.331			0.23
	$L_3M_5O_1$	9.333			
	$L_3M_5N_6$	9.355	9.336	2.1 ± 1.0	
	$L_3M_4O_{4,5}$	9.358			
	$L_3M_5N_7$	9.359			
	$L_3M_2O_{2,3}$	9.380			
	$L_1M_4M_4$	9.400	9.393	1.3 ± 0.4	0.48
	$L_2M_1N_3$	9.430			0.03
11b	$L_1M_4M_5$	9.485	9.466	6.9 ± 0.6	19.5
11c	$L_1M_5M_5$	9.564	9.573	1.4 ± 0.3	5.55

TABLE 8 (cont.)

Line No.	Assignment	Energy (keV) Z = 78		Relative Intensities	
		Calculated ΔZ = 1	Measured	This work Z = 78	Theory[81] Z = 47
12a	$L_2M_1N_{4,5}$	9.630	9.656	1.01 ± 0.15	
	$L_2M_2N_3$	9.701			1.05
12b	$L_2M_3N_1$	9.867	9.853	1.61 ± 0.30	0.05
	$L_2M_1N_{6,7}$	9.880			
	$L_2M_2N_{4,5}$	9.900			
12c	$L_2M_3N_{2,3}$	10.030	10.010	0.61 ± 0.30	0.86
12d	$L_2M_2N_{6,7}$	10.160	10.188	1.56 ± 0.30	
	$L_1M_1N_{4,5}$	10.250			
	$L_2M_3N_{4,5}$	10.280			
	$L_3N_1N_3$	10.296			0.06
12e	$L_2M_5N_{1,2}$	10.450	10.448	2.97 ± 0.39	0.65
	$L_3N_{2,3}N_3$	10.450			
	$L_2M_4N_{2,3}$	10.474			0.55
	$L_3N_1N_{4,5}$	10.500			
13a	$L_3N_3N_{4,5}$	10.700	10.661	5.8 ± 0.75	
	$L_2M_{4,5}N_{4,5}$	10.750			
13b	$L_3N_4N_{4,5}$	10.882	10.860	1.98 ± 0.29	
	$L_3N_{2,3}N_{6,7}$	10.900			
	$L_3N_5N_5$	10.915			
	$L_2M_4N_{6,7}$	10.985			

TABLE 8 (cont.)

Line No.	Assignment	Energy (keV) Z = 78		Relative Intensities	
		Calculated ΔZ = 1	Measured	This work Z = 78	Theory[81] Z = 47
14a	$L_2M_5N_{6,7}$	11.065	11.070	0.66 ± 0.08	
	$L_3N_4N_{6,7}$	11.151			
	$L_1M_3N_{6,7}$	11.161			
14b	$L_1M_{4,5}N_{4,5}$	11.375	11.292	1.18 ± 0.12	
	$L_3N_{6,7}N_{6,7}$	11.415			
14c	$L_1M_4N_{6,7}$	11.604	11.566	0.41 ± 0.10	

* Z = 36

The calculated energies are based on the binding energies from ref. 118. The theoretical relative intensities were normalized to the experimental ones as described in the text.

The calculated energies given in Table 8 were obtained from the formula

$$E_{L_iXY} = (E_{L_i})_Z - (E_X)_Z - (E_Y)_{Z+\Delta Z} \tag{70}$$

where E_{L_iXY} is the energy of the L_iXY Auger electrons, $(E_{L_i})_Z$ and $(E_X)_Z$ the binding energies of the L_i and X electron shells of element Z and $(E_Y)_{Z+\Delta Z}$ the binding energy of the Y-shell of an atom already ionized in the X-shell. The value of ΔZ lies in the range $0.7 \leq Z \leq 1.3$, the average taken to be one;[71] the binding energies are given by Hagström et al.[118] Since the assignments given in Table 8 were made by comparing calculated and measured energies, it is not possible to discuss in general the agreement between the calculations and measurements. However, the assignments of the isolated lines $L_3M_1M_3$, $L_3M_2M_3$, and $L_3M_3M_3$ are unambiguous, and the fact that the measured and calculated energies for these lines agree so closely (within 15 eV) supports the choice of $\Delta Z = 1$.

Asaad[81] has calculated Auger probabilities in j-j coupling for an initial L_i vacancy for elements of atomic number 18, 36, and 47. In order to compare his work to experimentally determined relative intensities, the number of initial L_i vacancies per disintegration must be determined since this number depends on the mode of vacancy production. The L-vacancies of ^{195}Pt result from (1) L-capture, (2) L-conversion, (3) $K\alpha_1$ and $K\alpha_2$ X-rays, (4) KLL and KLX Auger transitions, and (5) L-shell hole transfer

by Coster-Kronig transitions. The distribution of vacancies presented in Table 9 were calculated from the decay scheme presented by Harris et al.,[119] the $(L_1/K)_o$ capture ratio given by Brysk and Rose,[120] the fluorescence yields, Coster-Kronig yields, and (M + N + .../L) capture ratio given by Wapstra et al.,[121] and the L-subshell electron capture ratios given by Konopinski and Rose.[122] The uncertainties quoted in Table 9 are based upon the uncertainties which were reported for each value used in the calculation and which were propagated as standard deviations. The theoretical relative L-Auger intensities of Asaad[81] were modified to correspond to the same relative number of initial L-subshell vacancies as those calculated for ^{195}Pt. These values were then normalized to the experimental intensities and presented in Table 8. The normalization factor was determined by considering only lines with initial L_3 vacancies whose measured intensities had less than 20% uncertainty. If the electron capture branching ratios of the decay scheme presented by Goedbloed et al.[123] or the present work (see Chapter XV) are used instead of those of Harris et al.,[119] the numbers of vacancies calculated for each L-subshell will increase by approximately 8%; however, the relative number of L-subshell vacancies does not change.

Since the calculated Auger probabilities are expected to depend strongly on Z (see reference 81), one cannot expect good agreement between the calculated (Z = 47) and experimental (Z = 78) values; however, since Asaad's calculation of relative intensities is the only one available for

TABLE 9

DISTRIBUTION OF VACANCIES IN THE L-SUBSHELLS OF ^{195}PT PER DISINTEGRATION OF ^{195}AU

Contribution from	Electron subshell			
	K	L_1	L_2	L_3
Electron capture[a,b]	0.358	0.466	0.033	0.001
Internal conversion[c]	0.735	0.339	0.042	0.014
Radiative transfer from the K-shell[d]			0.295	0.540
Auger transfer from the K-shell[c]		0.038	0.025	0.033
Coster-Kronig transfer[d]			0.17	0.50
Total	1.09 ± 0.12	0.84 ± 0.10	0.56 ± 0.10	1.09 ± 0.10

a) See ref. 119 for decay scheme data.

b) See ref. 120 for (L_1/K) ground state capture ratio.

c) Present work

d) See ref. 121 for fluorescence and Coster-Kronig yields.

individual L-Auger lines, the comparison was made. Furthermore, the relative L-vacancies listed will be useful for normalizing the results of future theoretical calculations for higher Z. There are numerous large discrepancies between the measured intensities for platinum and the theoretical values for Z = 47; however, in a number of cases intense (or weak) lines in the measured spectrum were also intense (or weak) in the calculated one. A theoretical calculation of intensities for the L-Auger spectra of elements of high atomic number is needed.

Table 10 shows a comparison of the L-Auger intensities of this work with the experimental results for atomic numbers 79, 80, 81, 83, and 92 and the theoretical results of Asaad[81] for Z = 47. The intensities are compared for the same initial L-subshell vacancy since the relative number of initial L-subshell vacancies is different for each isotope. Where complex lines involving individual lines which originated from different initial L-subshell vacancies were not resolvable the calculations of Asaad was used as a guide to the intensity distribution between the lines. Since Asaad's calculations may not accurately relate to elements with atomic numbers as high as Z = 78, this procedure may introduce discrepancies in the comparison of results; however, this procedure should be at least as accurate as the previous practice of using the L-S coupling calculations of Rubenstein and Snyder as a guide. The results were all normalized to the present data, again employing an average normalization factor weighted

TABLE 10 A

THEORETICAL AND EXPERIMENTAL L-AUGER INTENSITIES FOR ATOMIC NUMBERS NEAR Z = 78

Line	Relative Intensities						
	Theory	Experiment					
	Z=47[81]	This work Z = 78	Z = 79[108]	Z = 80[99]	Z = 81[100]	Z = 83[112]	Z = 92[95]
$L_3M_1M_1$	9	---	---	---	---	---	---
$L_3M_1M_2$	9	50 ± 26	---	96	---	---	---
$L_3M_2M_2$	3	33 ± 18	---	---	---	---	---
$L_3M_1M_3$	183	135 ± 12	345	144	232 ± 49	180	213 ± 50
$L_3M_2M_3$	307	396 ± 10	403	384	336 ± 19	354	266 ± 100
$L_3M_1M_4$	21	76 ± 50	---	---	(37)	---	---
$L_3M_1M_5$	19		---	---	(78)	---	---
$L_3M_3M_3$	465	555 ± 50	288	620	(176)	650 ($L_3M_2M_5$)	520 ± 65
$L_3M_2M_4$	26	23 ± 23	345		(176)	---	---
$L_3M_2M_5$	299	122 ± 33	345	73	(100)	650 ($L_3M_3M_3$)	150 ± 52
$L_3M_3M_4$	453	490 ± 33	690	538	(368)	595	600 ± 80
$L_3M_3M_5$	741	625 ± 30	690	547	(710)	575	640 ± 90
$L_3M_4M_4$	361	(46)	230	202	---	---	(130)

TABLE 10 A (cont.)

Line	Relative Intensities						
	Theory	Experiment					
	Z=47[81]	This work Z = 78	Z = 79[108]	Z = 80[99]	Z = 81[100]	Z = 83[112]	Z = 92[95]
$L_3M_4M_5$	407	(930)	1725	1056	(1590)	1280	(1400)
$L_3M_5M_5$	392	(584)	920	826	(858)	650	(850)
$L_3M_1N_1$	2	(1.2)	---	---	---	---	107
$L_3M_1N_2$	1	(1.8)	---	---	---	---	---
$L_3M_1N_3$	16	(32)	---	---	(208)	---	---
$L_3M_2N_1$	1	(1.8)	---	---	---	---	---
$L_3M_2N_2$	1	(6.3)	---	32	---	---	---
$L_3M_1N_4$	---	---	---	---	} (61)	---	---
$L_3M_1N_5$	---	---	---	---		---	---
$L_3M_2N_3$	26	32 ± 12	---	63	---	---	---
$L_3M_3N_1$	28	36 ± 22	---	---	---	---	---
$L_3M_2N_4$	---	---	---	} 153	} (195)	---	---
$L_3M_2N_5$	---	---	---			---	---
L_3M_3N	32	(67)	---	57	115 ± 49	---	---

TABLE 10 A (cont.)

Line	Relative Intensities						
	Theory	Experiment					
	Z=47[81]	This work Z = 78	Z = 79[108]	Z = 80[99]	Z = 81[100]	Z = 83[112]	Z = 92[95]
$L_3M_3N_3$	89	(3.5)	345	163	245 ± 50	---	---
$L_3M_3N_4$	---	---	288	134	270	---	295
$L_3M_3N_5$	---	---				---	---
$L_3M_4N_1$	8	(10)	---	38	---	---	---
$L_3M_5N_1$	1	(2)	---		---	---	---
$L_3M_4N_2$	2	9 ± 8	---		---	---	---
$L_3M_5N_2$	23	(150)	---		---	---	---
$L_3M_4N_3$	42	(54)	---	---	24	---	70
$L_3M_3N_{6,7}$	---	---	---	144		---	---
$L_3M_5N_3$	70	8 ± 5	---		---	---	---

( ) indicates the use of theory as a guideline in the assessment of the intensity distribution of a complex line.

TABLE 10 B

THEORETICAL AND EXPERIMENTAL L-AUGER INTENSITIES
FOR ATOMIC NUMBERS NEAR Z = 78

Line	Relative Intensities			
	Theory	Experiment		
	Z = 47 [81]	Present work Z = 78	Z = 80 [99]	Z = 81 [100]
$L_2M_1M_1$	9	79 ± 63	---	---
$L_2M_1M_2$	176	175 ± 127	---	---
$L_2M_2M_2$	166	(915)	98	---
$L_2M_1M_3$	18	(67)	---	---
$L_2M_2M_3$	592	(610)	980	607
$L_2M_1M_4$	6	(15)	---	---
$L_2M_1M_5$	36	(93)	---	---
$L_2M_3M_3$	17	(216)	334	547
$L_2M_2M_4$	328	(318)		547
$L_2M_2M_5$	610	477 ± 48	470	---
$L_2M_3M_4$	452	607 ± 40	432	607
$L_2M_3M_5$	61	(154)	196	---
$L_2M_4M_4$	11	(153)	865	1220
$L_2M_4M_5$	506	(1340)	1410	3640
$L_2M_5M_5$	643	(105)	294	---
$L_2M_1N_1$	2	(50)	---	---
$L_2M_1N_2$	14	(171)	---	---
$L_2M_1N_3$	2	(3)	---	---

( ) indicates the use of theory as a guideline in the assessment of the intensity distribution of a complex line.

TABLE 10 C

THEORETICAL AND EXPERIMENTAL L-AUGER INTENSITIES
FOR ATOMIC NUMBERS NEAR Z = 78

Line	Relative Intensities			
	Theory	Experiment		
		Present work		
	Z = 47[81]	Z = 78	Z = 80[99]	Z = 81[100]
$L_1M_1M_1$	116	(755)	---	---
$L_1M_1M_2$	226	97 ± 68	---	---
$L_1M_2M_2$	1	(33)	---	---
$L_1M_1M_3$	451	182 ± 29	300	230
$L_1M_2M_3$	22	197 ± 68	---	1030
$L_1M_1M_4$	376	477 ± 49	400	---
$L_1M_1M_5$	564	(131)	400	---
$L_1M_3M_3$	13	494 ± 97	---	---
$L_1M_2M_4$	6	(17)	200	---
$L_1M_2M_5$	141	(92)	200	---
$L_1M_3M_4$	170	(35)	} 500	230
$L_1M_3M_5$	129	(620)		230
$L_1M_4M_4$	20	(109)	620	---
$L_1M_4M_5$	811	665 ± 59	810	650
$L_1M_5M_5$	231	138 ± 30	200	570

( ) indicates the use of theory as a guideline in the assessment of the intensity distribution of a complex line.

heavily toward well resolved lines. The comparison for Z = 82 and 92 was made for only the L_3 subshell due to the uncertainties in obtaining intensities for unresolved lines arising from different initial L-subshell vacancies.

D. The M-Auger and L-Coster-Kronig Spectrum

An attempt was made to measure the intensity of the L-Coster-Kronig transitions relative to the L-Auger lines in order to compare these values with the recent values calculated by Asaad. This measurement is extremely difficult due to the low energy of the electrons. These electrons are easily absorbed by mass deposited with the source activity and they are difficult to detect since they are easily absorbed by counter windows. The amount of source mass is difficult to assess. The active ^{195}Au deposited contributes a negligible (approximately 10^{-5} $\mu g\text{-}cm^{-2}$) amount of mass; however, we estimate that the unknown solids in the original ^{195}Au solution (quoted by the suppliers as 0.1 $mg\text{-}ml^{-1}$) could contribute as much as 1 $\mu g\text{-}cm^{-2}$ to the source thickness.

A second method can be used to estimate the amount of mass on the source. As previously noted (see Section A of this chapter) the resolution at low energies is a function of momentum; thus one can estimate the maximum energy loss from the change in momentum resolution. This energy loss can then be compared with stopping power values for electrons

of corresponding energies and the effective thickness of mass traversed can be determined. The electron stopping powers were estimated by considering the stopping power of electrons and protons to be identical for equal velocities and using the proton stopping powers published by Whaling.[124] The source thickness estimated in this manner is approximately 2 $\mu g\text{-}cm^{-2}$ which is in reasonable agreement with the value, 1 $\mu g\text{-}cm^{-2}$, estimated from the inert solids in the solution.

The M-Auger and L-Coster-Kronig spectra are shown in Figure 31; Figure 32 shows the remaining low-energy electron spectrum to zero energy. In order to detect electrons with energies less than 120 eV, the retarding potential was removed from the post-acceleration counter. A post-acceleration potential of 5000 volts enabled detection of these low-energy electrons with 62% transmission at 0.0 keV and 92% at 3.25 keV electron energy. The data shown in Figures 31 and 32 are raw data and have not been corrected for transmission.

Due to the complexity of the superimposed LLN Coster-Kronig and M-Auger transitions no detailed analysis was possible. The total intensity of this group of lines was estimated by measuring the area defined by the line group. The area was corrected for transmission and divided by BR in order to compare it to the L-Auger spectrum. The calculated energies of the $L_1L_3M_4$ and $L_1L_3M_5$ transitions place these lines by themselves below the energy of the M-Auger and LLN Coster-Kronig

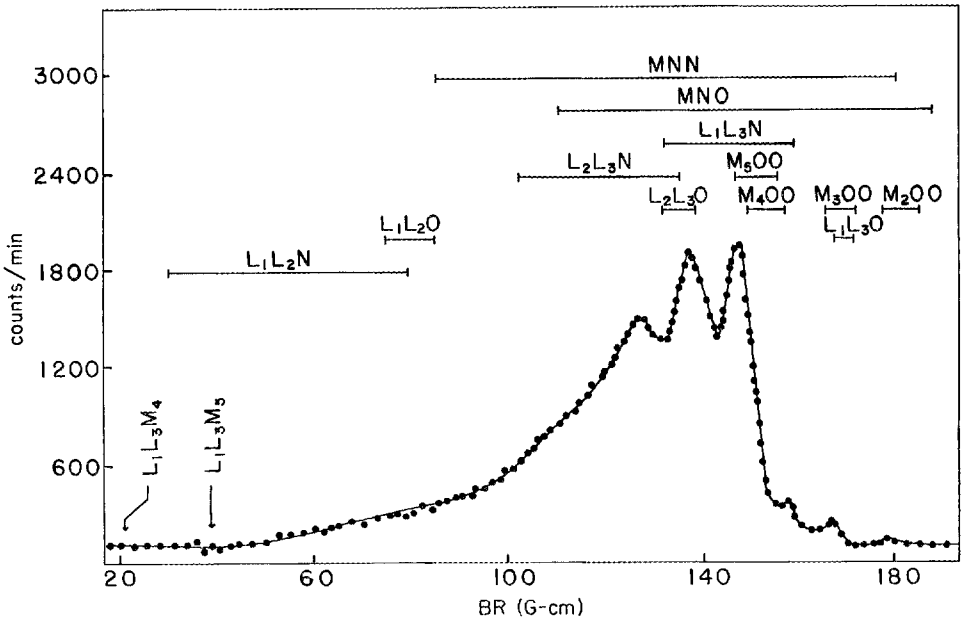

Fig. 31. The M-Auger and L-Coster-Kronig spectra of platinum.

groups. The calculated positions of these lines are shown in Figures 31 and 32. It was possible only to set tentative upper limits on the intensities of the $L_1L_3M_4$ and $L_1L_3M_5$ Coster-Kronig lines. The measured intensity ratios $L_1L_3M_4/L_3M_2M_3$ and $L_1L_3M_5/L_3M_2M_3$ are $\lesssim 1$ each; whereas the ratios deduced from Asaad's relative intensities[82] are 19 and 23, respectively. The sum of the intensities of the L-Coster-Kronig and M-Auger lines is approximately 150 times that of the $L_3M_2M_3$ Auger lines. These intensity ratios are termed tentative since it cannot be determined conclusively what affect the source mass has on these low-energy lines. Since the calculated energies of the $L_1L_3M_4$ and $L_1L_3M_5$ electrons are only 37 and 122 eV, respectively, and since the stopping power in gold for electrons of 37 eV and 122 eV is approximately 95 and 118 eV-μg^{-1}-cm^2, respectively, these electrons would be strongly absorbed in the source if the source thickness is approximately 1 μg-cm^{-2} as estimated.

Because of the uncertainties in source thickness, no definite conclusions regarding the intensities of the $L_1L_3M_4$ and $L_1L_3M_5$ lines can be reached. It should also be noted that the gradual decrease in intensity at the low-energy side of the lines observed at approximately 140 BR (Figure 31) could be a result of source absorption. If so, the measured intensity of the M-Auger and LLN Coster-Kronig lines would be a lower limit.

The two lines shown in Figure 32 at approximately 8 and 10 eV, respectively, might at first be thought to be attributed to Coster-Kronig

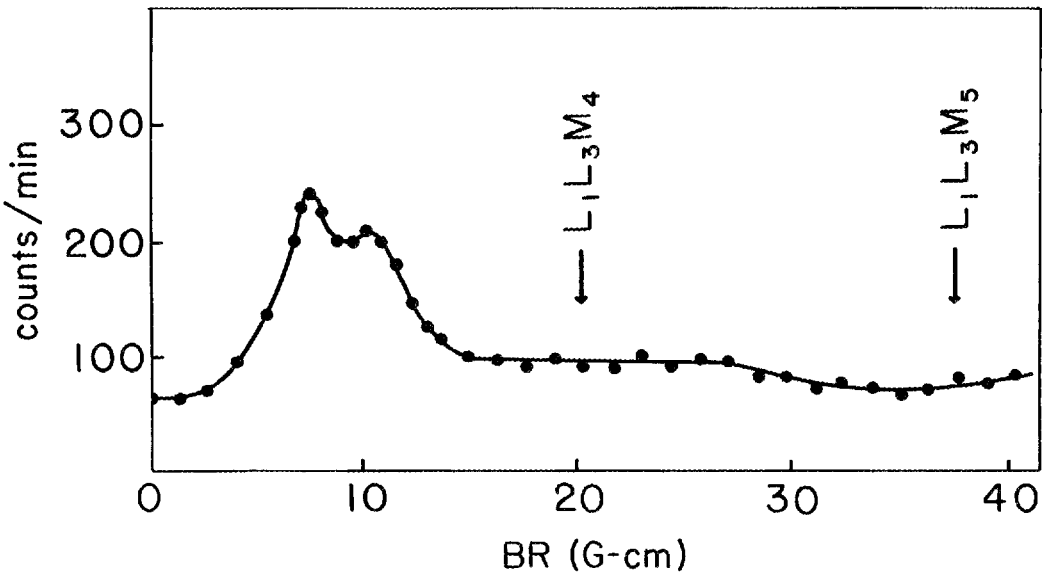

Fig. 32. The very-low-energy electron spectrum of platinum.

transitions or other low-energy Auger processes; however, it has been demonstrated that these lines do not come directly from the ^{195}Au source. These lines were still observed when the source was covered by a Zapon film of sufficient thickness to stop electrons of energies less than approximately 3 keV. These lines were also observed for other radioactive sources (see reference 95). When the electron intensities are corrected for BR and these lines are plotted as an energy distribution (see Figure 33) they have approximately the same shape as an electron line at 10 eV found by Hubbell et al.[125] The low-energy electron line found by Hubbell et al. is normalized to the intensity of the present measurements and plotted in Figure 33. These low-energy lines have been attributed to electrons scattered from the aluminum source holder and spectrometer walls and to secondary emission electrons from the source. They do not come directly from low energy transitions within the source itself.

E. The K-Auger Spectrum

The K-Auger spectrum was recorded at 0.2% resolution (fwhm) from the mylar backed source. The energy of the K-Auger electrons ($E \cong 50$ keV) was sufficient to ensure 100% transmission through the detector window without the aid of post-acceleration. The KLL and KLX spectra of platinum are shown in Figure 34. To resolve overlapping lines, the KL_2L_3 line shape was used after the low-energy tail was adjusted to

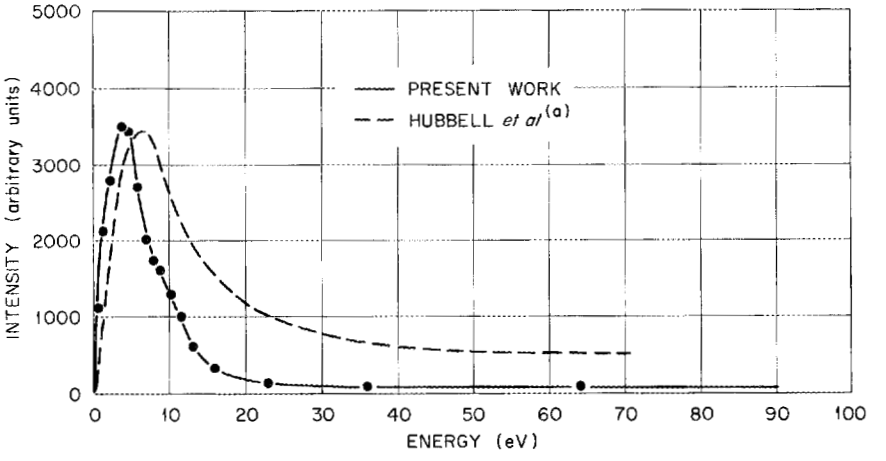

Fig. 33. The very-low-energy spectrum of platinum plotted as an energy distribution and compared to previous similar data. (a) see reference 125.

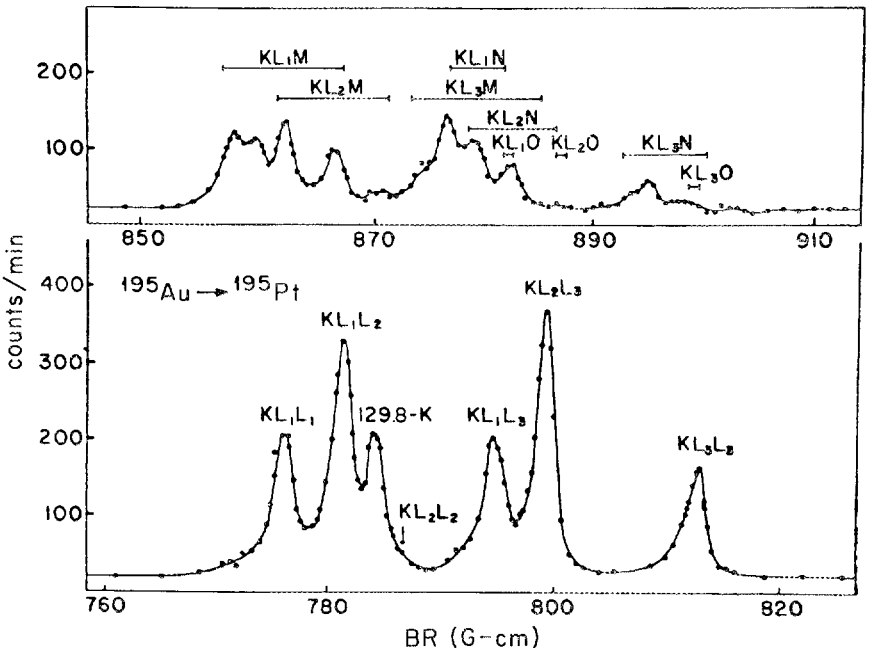

Fig. 34. The KLL and KLX Auger spectra of platinum.

give the most consistent line fit throughout the spectrum. Although the KL_3L_3 line appears isolated, it would not be used as a standard because its shape is distorted on the low-energy side by the KL_3L_3 (^3P_o) satellite line.[113] By means of a standard line shape, the KL_3L_3 (^3P_o) line was graphically resolved (see Figure 35) and the energy and intensity measured. The energies and intensities of the KLL Auger lines are given in Table 11 and those of the KLX lines are given in Table 12.

The theoretical energies presented in Table 11 are based on the equations of Asaad and Burhop[67] in the intermediate coupling approximation. One set is calculated by Hörnfeld,[68] the other by Listengarten.[71] The two sets differ in the manner in which approximate relativistic corrections were introduced. Listengarten applied a term $(1 - \alpha Z^2)$ while Hörnfeldt used the factor $(1 - \beta Z^3)$, α and β being adjustable parameters. The agreement between the theoretical and experimental values is within the $\pm$ 0.2% uncertainties assigned to the measured energies. In Table 11, the present work is compared to various experimental and theoretical relative intensities for KLL lines of elements of atomic number near 78. The theoretical values presented in Table 11 are based on the following calculations: Line 11 shows the results of the relativistic calculations of Asaad[72] in j-j coupling for atomic number 80, using wave functions obtained numerically on electronic computers. Line 12 gives the values of line 11 adjusted by Asaad[73] in an approximate manner to include

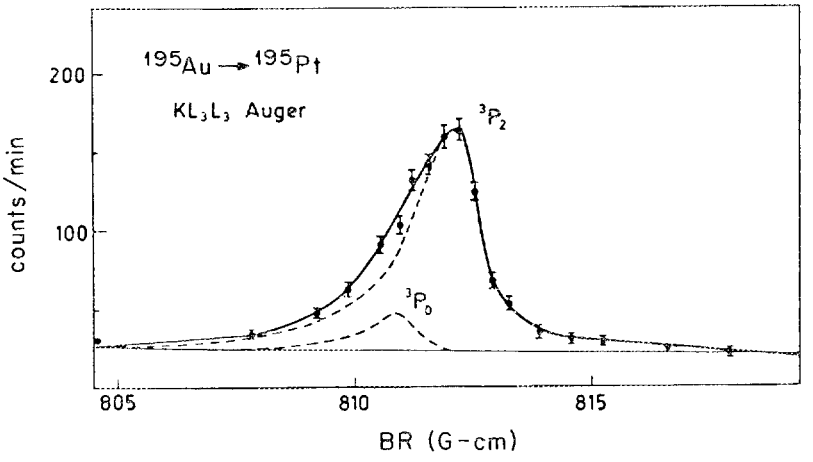

Fig. 35. The KL_3L_3 Auger line showing the graphical resolution of the $^3P_0$ satellite line.

TABLE II

ENERGIES AND RELATIVE INTENSITIES OF THE KLL AUGER TRANSITIONS OF PLATINUM

Line	KL_1L_1	KL_1L_2	KL_1L_3	KL_2L_2	KL_2L_3	$KL_3L_3(^3P_2)$	$KL_3L_3(^3P_0)$
Energies							
1. Present work (Z=78)*	50.32±0.10	50.97±0.10	52.67±0.11	51.55±0.10	53.27±0.10	55.04±0.11	54.87±0.11
2. Calculated[68] (Z=78)	50.388	51.005	52.679	51.566	53.289	55.020	54.956
3. Calculated[71] (Z=78)	50.372	51.003	52.676	51.541	53.260	54.983	
Relative intensities							
Experimental							
4. Present Work (Z=78)	1.0	1.42±0.18	0.85±0.12	0.19±0.10	1.69±0.22	0.59±0.09	0.062±0.013
5. Herrlander[126] (Z=80)	1.0	1.68±0.13	0.85±0.10	0.14±0.07	1.84±0.15	0.76 ± 0.08	
6. Jung[127] (Z=80)	1.0	1.48±0.11	0.79±0.08	0.19±0.10	1.69±0.16	0.69 ± 0.07	
7. Hörnfeldt[68] (Z=80)	1.0	1.70	0.90	0.20	1.60	0.80	
8. NaII[99] (Z=80)	1.0	1.32±0.10	0.85±0.06	0.40±0.03	1.27±0.08	0.76 ± 0.05	
9. Ewans[128,129,a] (Z=78)	1.0	1.40±0.25	0.90±0.10	0.20±0.10	1.40±0.25	0.80 ± 0.20	
10. Wolfson[114] (Z=79)	1.0	1.54±0.11	0.99±0.09	0.11±0.03	1.83±0.13	0.75 ± 0.07	
Theoretical							
11. Asaad[72] (Z=80)	1.0	1.44	0.82	0.09	1.46	0.66	
12. Asaad[73] (Z=80)	1.0	1.51	0.67	0.095	1.49	0.54	0.091
13. Asaad[74] (Z=80)	1.0	1.17	2.09	0.195	3.48	1.66	0.30
14. Listengarten[a] (Z=79)	1.0	1.67	0.95	0.07	1.38	0.60	
15. Asaad[67] (Z=80)	1.0	1.20	2.27	0.15	4.32	2.12	0.28

*The error limits of the measured energies are ± 0.2%

[a] quoted in reference 114

TABLE 12

ENERGIES AND RELATIVE INTENSITIES OF THE KLM AUGER LINES OF PLATINUM

Line	Energy this work	Energy $\Delta Z = 1$	Relative Intensities*			
			This work Z = 78	Ewans[128,129] Z = 78	Nall[99] Z = 80	Asaad[67] Z = 80
KL_1M_1	61.093	61.078	0.35 ± 0.05	0.5	0.35	0.31
KL_1M_2	61.365	61.354	0.32 ± 0.04	0.3	0.43	0.19
KL_2M_1	61.731	61.695	0.47 ± 0.02	0.5	0.75	0.60
KL_1M_3		61.760				
KL_2M_2		61.971		---		
KL_1M_4	62.326	62.212	0.35 ± 0.05	0.4	0.75	0.98
KL_1M_5		62.297				
KL_2M_3		62.377				
KL_2M_4	62.839	62.829	0.11 ± 0.05	---	0.89	0.32
KL_2M_5		62.914		---		

KL_3M_1	63.406	63.406	0.11 ± 0.05	---	0.16	0.315
KL_3M_2	63.694	63.682	0.44 ± 0.09	0.50	0.40 (+$KL_1N_{4,5}$)	0.801
KL_1N_{1-3}	63.870	≈63.8	0.10 ± 0.05			

*Normalize to $KL_iL_1 = 1.0$

TABLE 12 (cont.)

Line	Energy this work	Energy $\Delta Z = 1$	Relative Intensities* This work Z = 78	Ewans[128,129] Z = 78	Nall[99] Z = 80	Asaad[67] Z = 80
KL_3M_3	64.037	64.088	0.40 ± 0.12	0.40		0.848
$KL_1N_{4,5}$		≈64.16			0.69 (+$KL_1N_{4,5}$)	---
KL_2N_1	64.195	64.360	0.10 ± 0.05	0.25		---
KL_1O_{1-3}		≈64.4				---
$KL_1N_{6,7}$		≈64.4				---
KL_3M_4	64.495	64.540	0.25 ± 0.07		0.38 (+$KL_2N_{4,5}$)	0.520
$KL_1O_{4,5}$		≈64.5				
$KL_2N_{2,3}$		≈64.76			0.73	
KL_3M_5		64.625				
KL_3N_{1-7}	---	≈66.5	0.18 ± 0.06	0.2	0.30	---

*Normalize to $KL_1L_1 = 1.0$

effects of intermediate coupling. This adjustment was based on the manner in which intermediate coupling affected nonrelativistic j-j calculations. The most recent theoretical treatment of the KLL Auger spectra (shown in line 13) is a calculation of Asaad[74] based on the intermediate coupling and configuration interaction. This calculation was made in an attempt to resolve discrepancies between the theoretical and experimental KLL relative intensities at low Z. The values of Listengarten given in line 14 are the values extrapolated to atomic number 79 as quoted by Wolfson and Baerg.[114] Listengarten's results are relativistic, but differ from Asaad's values (line 11) in the manner in which screening was considered. Line 15 is a nonrelativistic, intermediate coupling calculation by Asaad and Burhop.[67]

There is general agreement among the experimental intensities listed in Table 11 except for the KL_2L_2 and KL_2L_3 values given by Nall et al.[99] Agreement between the experimental values and the theoretical results of Asaad[72] is quite good except that the theoretical value for the KL_2L_2 line is too small. Asaad's latest results[74] which include the configuration interaction, give agreement with the measured KL_2L_2/KL_1L_1 ratio; however, his theoretical KL_1L_3, KL_2L_3, and KL_3L_3 intensities are more than twice as large as the experimental ones.

The measured intensity of the KL_3L_3 (^3P_o) satellite line (Table 11) is the first to be reported in this Z-region. The ratio $KL_3L_3(^3P_o)/KL_3L_3(^3P_o + {}^3P_2)$

is found to be 0.095 ± 0.024. This value is not in agreement with the value of 0.15 deduced from Asaad's theoretical intensities which include the configuration interaction. Furthermore, Asaad's intensities (relative to the KL_1L_1 line) for the $KL_3L_3(^3P_0)$ and $KL_3L_3(^3P_2)$ components are larger than the experimental intensities by a factor greater than 2. The original theory of Asaad and Burhop[67] gives for the ratio $KL_3L_3(^3P_0)/KL_3L_3(^3P_0 + {}^3P_2)$ a value of 0.12 at Z = 80; this value agrees with our experimental value just within the limits of error. Again, however, the individual theoretical intensities are much larger than the experimental ones.

Table 12 is a comparison of the KLX energies and relative intensities measured in the present work with values of other workers and with theory. The theoretical relative intensities are from a nonrelativistic intermediate coupling calculation of Asaad and Burhop.[67] The transition energies were calculated using $\Delta Z = 1$ and the binding energies of Hagstrom et al.[118] The intensities reported here agree well with the earlier experimental work of Ewan[128, 129] but not with the theoretical values of Asaad and Burhop nor with the experimental values of Nall et al.[99] The value of KLX/KLL as determined by the present work (Z = 78) is 0.548 ± 0.044. This value is in approximate agreement with the values 0.53 found by Passel et al.[130] for Z = 80, 0.496 ± 0.015 found by Nall et al.[99] for Z = 80, 0.71 ± 0.15 found by Broyles et al.[131] for Z = 80 and

0.56 found by Herrlander et al.[126] for Z = 82. It does not agree with the value 0.86 given by Steffen et al.[132] for Z = 78. The line of best fit to all the experimental values, as given by Bergstrom and Nordling,[113] yields KLX/KLL = 0.55 at Z = 78, which is in good agreement with the value measured in this work.

CHAPTER XV

THE CONVERSION-ELECTRON SPECTRUM IN THE ELECTRON CAPTURE DECAY OF ^{195}Au

A. Introduction

Previous investigations of the internal conversion spectrum in the decay of ^{195}Au were executed by means of permanent magnet[133-136] and lens[137] spectrometers with only approximate intensity measurements being obtained. The resolution obtained in these early studies was not sufficient to resolve many of the electron lines; thus, only rough estimations of the transition multipolarities could be made based on relative intensity ratios of groups of conversion lines. In the present work, the electron spectrum was recorded at high resolution by means of the Vanderbilt double-focusing spectrometer, and accurate energy and intensity measurements were obtained. The resolution was sufficient to resolve the L-subshell conversion-electron lines of the three major gamma-rays so that L-subshell conversion ratios could be used to determine transition multipolarities. The L-subshell intensity ratios were compared to the theoretical values for a dual purpose: 1) to determine multipolarities and 2) to look for anomalous L-subshell ratios.

Although the spins, parities, and approximate energies of the ground and exited states of ^{195}Pt are well established, the population of these states by electron capture in the decay of ^{195}Au is less certain. The relative capture ratios to the excited states of ^{195}Pt can be determined by means of published gamma-ray intensities and the conversion-electron intensities of this work. Furthermore the ground state capture probability can be determined with the aid of the measured K-Auger intensities and published L/K and L/(M + N + ...) capture ratios. The electron capture branching ratios are calculated for the decay of ^{195}Au and compared to previously reported values.

Published gamma-ray intensities were normalized to the relative electron intensities reported here and conversion coefficients calculated. This calculation is useful since wide variations occur among conversion coefficients previously reported. The observation of the K-conversion line of the 210 keV transition proves the existence of the previously reported 210 keV transition. Previously, there had been no electron line detected for this transition.

B. Source Preparation

Two ^{195}Au sources were used in the measurement of the conversion-electron spectrum. The first source was previously described in section B of Chapter XIV. It was prepared by electroplating the activity from a

nearly neutral solution (pH $\cong$ 6) onto a silver coated mylar backing. For high resolution studies the spectrometer transmission is necessarily low; thus a more intense source was needed. The source prepared for this purpose was approximately eight times more intense than previous sources and had a narrow profile (0.5 x 20 mm^2) to enhance resolution. This source was electroplated from a 0.1 N HCl solution onto a 54 $mg\text{-}cm^{-2}$ platinum foil.

C. Experimental Method and Results

The measurements were made by means of the double-focusing spectrometer described in Chapter XIII. An initial scan of the spectrum at 0.2% resolution (fwhm), shown in Figure 36, was made using the low-energy counter with no post acceleration; the counter walls and deceleration plate were electrically grounded. Further scans at higher resolution were made on the conversion lines of the 129.8 keV transition (0.17%) using the low-energy counter and on the conversion lines of the 98.8 keV transition (0.13%) using the high-energy counter. The spectra obtained at high resolution are shown in Figure 37. The K-conversion line of the 210 keV transition, shown in Figure 38, was observed only by means of the high-energy detector. The counter windows were sufficiently thin to ensure 100% transmission for all conversion-electrons. While the K- and L-subshell lines were well resolved, the conversion lines of outer shells were graphically resolved in the manner previously described for the Auger lines (see section C of Chapter XIV). The standard lines used for this work were resolved L-shell conversion lines.

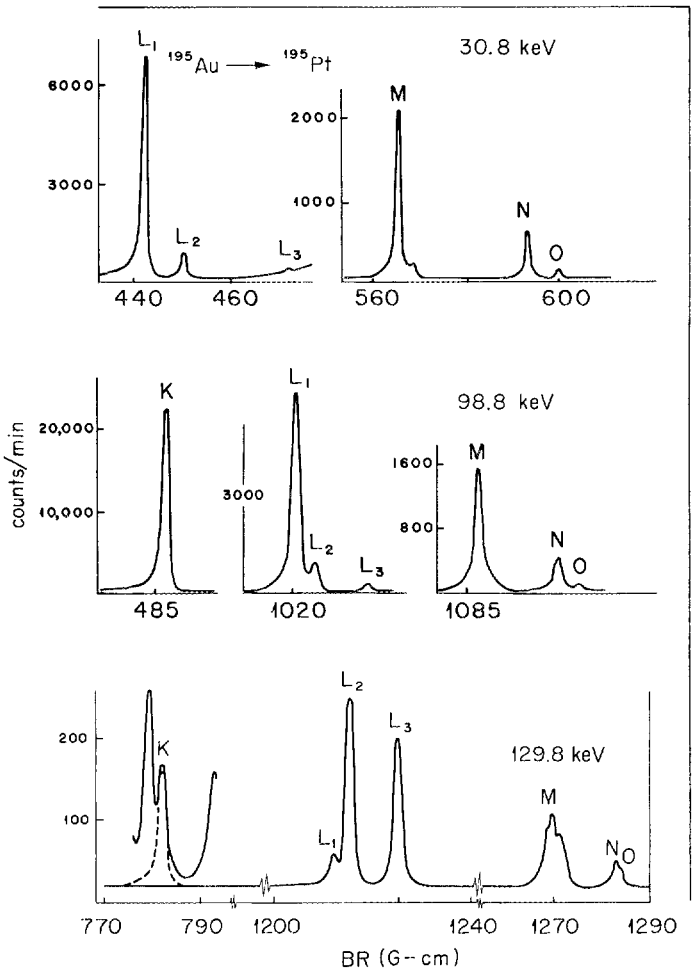

Fig. 36. The initial scan of the conversion-electron spectrum with 0.2% resolution (fwhm).

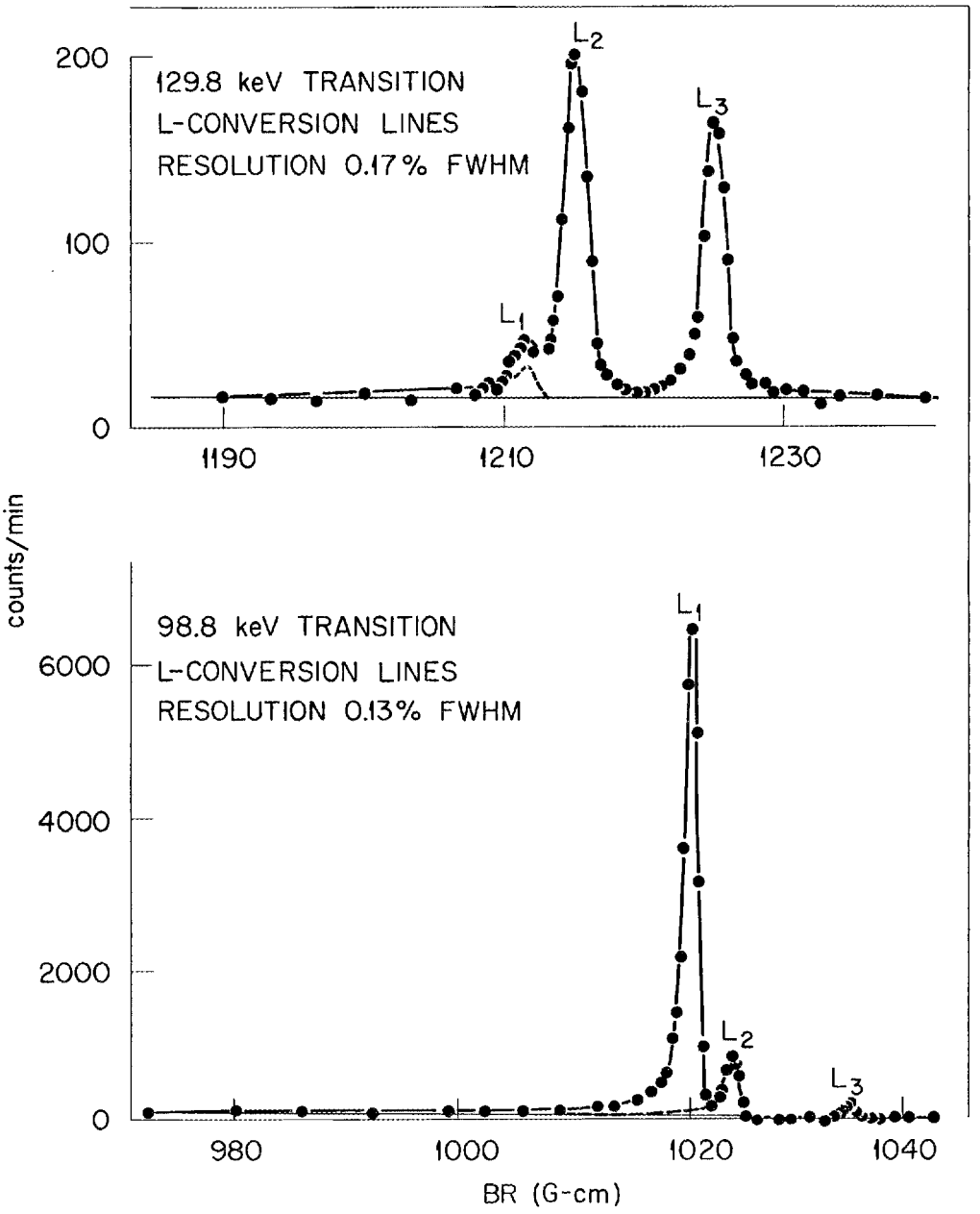

Fig. 37. L-conversion lines of the 98.8 and 129.8 keV transitions recorded with high resolution.

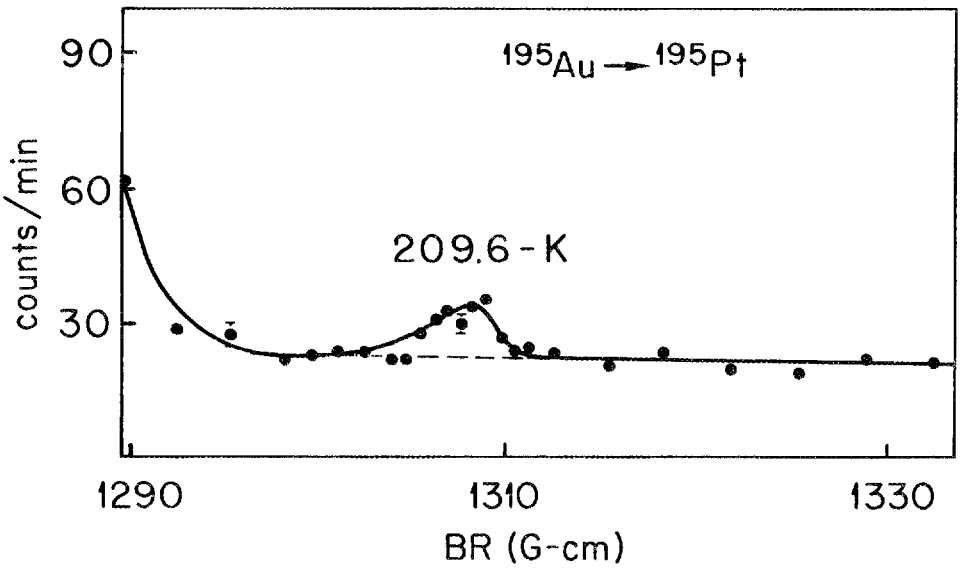

Fig. 38. The K-conversion line of the 210 keV transition.

The areas of the conversion-electron lines were measured by means of a planimeter and divided by BR to obtain the intensities reported in Table 13. The error limits assigned to the intensities are to be interpreted as standard deviations and include the uncertainties in area measurements as well as statistical uncertainties in the raw data. For each raw data point on a curve these statistical uncertainties were less than 3% except for the K-conversion line of the 210 keV transition for which the statistics were approximately 15%. The data taken from the more intense source were normalized to the other data by means of the intensity of the L_3 line of the 129.8 keV transition. The error limits quoted in Table 13 include an estimation of the uncertainty in the normalization procedure.

The selected energies of the three major gamma rays reported in Table 13 are weighted averages of the energies calculated from each conversion line. The binding energies of Hagstrom et al.[118] were used. The transition energies 129.83 ± 0.26, 98.84 ± 0.20, and 30.80 ± 0.06 keV obtained in this work are to be compared with the values 129.4, 98.5, and 30.8 keV given by Cressman and Wilkinson.[133] McGowan and Stelson[138] have previously reported a transition at 210 keV in the gamma spectrum of ^{195}Pt excited by Coulomb excitation. No electron line from this transition has been reported previously. We observed the K-conversion line of this transition and deduced a transition energy of 209.6 ± 0.4 keV. The measured energies have been assigned an estimated uncertainty of 0.2%. This

TABLE 13

CONVERSION-ELECTRON DATA IN THE DECAY OF ^{195}AU

Conversion Shell	Electron Energy (keV)	Transition Energy* (keV)	Relative Line Intensity
L_1	16.94	30.82	25.25 ± 0.75
L_2	17.54	30.82	1.98 ± 0.06
L_3	19.25	30.81	0.34 ± 0.07
M_1	27.49	30.79	5.06 ± 0.20
M_2	27.76	30.80	0.61 ± 0.07
N_1	30.07	30.79	1.37 ± 0.10
O	30.68	30.78	0.22 ± 0.07
Selected transition energy: 30.80 ± 0.06			
K	20.51	98.90	90.10 ± 1.48
L_1	84.93	98.82	12.0 ± 0.25
L_2	85.56	98.83	1.15 ± 0.05
L_3	87.24	98.80	0.35 ± 0.04
$M_{1,2}$	95.031	98.33	2.99 ± 0.12
M_3	95.742	98.77	0.17 ± 0.03
N	97.73	98.45	0.75 ± 0.05
O	98.45	98.51	0.11 ± 0.04
Selected transition energy: 98.84 ± 0.20			

*The transition energies were calculated from the measured electron energies and the binding energies given by Hagström et al.[118]

TABLE 13 (cont.)

Conversion Shell	Electron Energy (keV)	Transition Energy* (keV)	Relative Line Intensity
K	51.32	129.72	0.49 ± 0.08
L_1	115.92	129.81	0.033 ± 0.010
L_2	116.61	129.88	0.45 ± 0.04
L_3	118.33	129.90	0.33 ± 0.03
M_1	126.27	129.57	0.23 ± 0.04
M_2	126.39	129.42	
M_3	126.71	129.36	
N	128.77	129.49	0.07 ± 0.02
Selected transition energy: 129.83 ± 0.26			
K	131.20	209.6 ± 0.4	0.004 ± 0.002
Selected transition energy: 209.6 ± 0.4			

*The transition energies were calculated from the measured electron energies and the binding energies given by Hagström et.al.[118]

uncertainty includes possible systematic errors in calibration as well as random deviations in the measurements. The uncertainties are conservatively assigned and may be smaller than indicated. The sum 98.84 + 30.80 = 129.64 is within 0.15% of the measured value of 129.83 keV.

The electron capture branching ratios in the decay of ^{195}Au can be calculated by means of the following equations.

$$NP_{209.6} = I_{e209.6} + I_{\gamma 209.6} \tag{71}$$

$$NP_{129.8} = I_{e129.8} + I_{\gamma 129.8} + I_{e30.8} + I_{\gamma 30.8} \tag{72}$$

$$NP_{98.8} = I_{e98.8} + I_{\gamma 98.8} - I_{e30.8} - I_{\gamma 30.8} \tag{73}$$

$$NP_o = \frac{P_o}{P_{K_o}} \left[\frac{I_{K\text{ - Auger}}}{a_K} - I_{e209.6K} - I_{e98.8K} \right.$$
$$\left. - I_{e129.8K} - NP_{129.8}\left(\frac{P_{129.8K}}{P_{129.8}}\right) - NP_{98.8}\left(\frac{P_{98.8K}}{P_{98.8}}\right)\right] \tag{74}$$

where

N = number of ^{195}Au disintegrations per unit time (a normalization factor)

P_E = fraction of total electron capture to energy level E

P_{EK} = fraction of electron capture to energy level E that is K electron capture

I_{eK} = conversion-electron intensity associated with the transition of energy E

I_{eEK} = K-conversion-electron intensity associated with the transition of energy E

$I_{\gamma E}$ = gamma-ray intensity associated with the transition of energy E

$I_{K\text{-Auger}}$ = K-Auger electron intensity

a_K = K-Auger yield for Z = 78 .

In order to evaluate the above equations the relative gamma-ray intensities must be known and properly normalized to the electron intensities measured in this work. The relative gamma-ray intensities used were mean averages of intensities reported by Harris et al.[119] and Goedbloed et al.[123] The latter authors report no error limits; therefore, error limits of ± 10% were assigned to their work for the purpose of computing the standard deviation of the mean value. The mean gamma-ray intensities were normalized to the electron intensities of the present work by means of the K-conversion coefficient of the 129.8 keV transition. This transition has previously[119,133-137] been assigned as pure E2 which agrees with the present assignment discussed later in this chapter. The theoretical E2 K-conversion coefficient $\alpha_K^{129} = 0.46$ interpolated from the tables of both Rose* and Sliv and Band**

* The conversion coefficients were interpolated from log α versus E plots from Rose's tables.[90]

**The interpolation of Sliv and Band's table[88] of conversion coefficents was obtained by means of a computer. These values were furnished by the Nuclear Data Group at Oak Ridge National Laboratory.

was used for the normalization. The normalization factor ξ was determined from the relationship

$$\xi = \frac{I_{e129.8K}}{\alpha_K^{129.8} \, I_{\gamma 129.8}} \quad . \tag{75}$$

The normalized gamma-ray intensities are presented in Table 14.

The K/ total electron capture ratios for each transition were obtained from published P_L/P_K ratios and the ratio $P_L/(P_M + P_N + \ldots) = 3.79$ given by Wapstra et al.[121] Whereas the ratio $P_L/(P_M + P_N + \ldots)$ is the same for all transitions in ^{195}Pt [the transition energies are large compared to the L binding energy (see reference 120)], the ratio P_L/P_K depends strongly on the transition energy. The ratio $P_{L129.8}/P_{K129.8}$ has been reported by Harris et al.[119] and Bisi et al.[136] to be 5.1 ± 0.2 and 5.5 ± 0.9, respectively. An average value $P_{L129.8}/P_{K129.8} = 5.3 \pm 0.5$ was used in the evaluation of Equation (74). The ratio $P_{L98.8}/P_{K98.8} = 1.12 \pm 0.3$ reported by Harris et al. and the theoretical ratio of Brysk and Rose[120] $P_{L_o}/P_{K_o} = 0.71$ were also used.

The semi-empirical relationship due to Burhop[83] with the numerical constants given by Hagedoorn and Wapstra[84] was used to calculate a value for the fluorescence yield of platinum. This relationship should be accurate to within ± 0.005. The Auger yield deduced from this result ($a_K = 1 - \omega_K$) is $a_K = 0.049 \pm 0.005$.

TABLE 14

PHOTON RELATIVE INTENSITIES REPORTED BY PREVIOUS WORKERS

Photon Energy (keV)	Relative Intensity			
	Reference 119	Reference 123	Mean*	Normalized†
30.8	13.3 ± 1.8	9.31	10.8 ± 2.0	1.43 ± 0.41
98.8	100	100	100	13.3 ± 2.9
129.8	7.7 ± 0.8	8.38	8.0 ± 1.1	1.06 ± 0.27
210	0.25 ± 0.03	0.24	0.25 ± 0.04	0.033 ± 0.009

*A 10% uncertainty was arbitrarily assigned to the values of reference 123 in order to compute the uncertainties in the averages.

†Normalized to electron intensities of Table 13, see text for details.

Since only the K-conversion line of the 209.6 keV transition was measured, the total electron intensity for this transition had to be estimated. The ratio of L/K conversion coefficients as calculated by Sliv and Band[88] were used in the estimation of the 209.6 keV L-conversion electron intensity. The K-Auger intensities were obtained by normalization of the intensities of Tables 11 and 12 to the conversion-electron intensities. An average normalization factor was obtained by comparison of the intensities of the K-conversion line of the 129.8 keV transition with the KL_1L_1 and KL_3L_3 line intensities. A small correction was made for the KXY intensities which were not observed in the present work. With the above information, the normalized gamma-ray intensities and the measured conversion-electron intensities, Equations (71) through (74) were used to calculate the following branching ratios: $P_{209.6} = (0.035 \pm 0.010)\%$, $P_{129.8} = (32 \pm 1)\%$, $P_{98.8} = (68 \pm 3)\%$, and $P_o < 5\%$. A rather large uncertainty exists in the calculation of the probability of capture to the ground state. The calculated branching ratio is very sensitive to the K-Auger electron intensity which has been normalized to the conversion-electron intensities. A negative branching ratio resulted when Equation (74) was solved; however, the uncertainty in the K-Auger intensity due to the uncertainty in the normalization factor (approximately 10%) would allow an upper limit for the ground state branching ratio of approximately 5%. The solution to Equation (74) is, therefore, strongly indicative of a zero branching ratio to the ground state. The

uncertainty in the ground state branching ratio does not effect the relative values of the branching ratios to the excited states.

The branching ratios calculated above are in relatively good agreement with early values of $P_{129} = 35\%$ and $P_{98} = 65\%$ reported by DeShalit et al.[137] However, severe discrepancies occur between the present results and the recent results of Harris et al.[119] [$P_{210} < 0.4\%$, $P_{129} = (40 \pm 6)\%$, $P_{99} = (47 \pm 6)\%$, and $P_o = (13 \pm 10)\%$] and of Goedbloed et al.[123] [$P_{210} \leq 0.5\%$, $P_{129} = 41\%$, $P_{98} = 59\%$, and $P_o < 6\%$].

The electron capture branching ratios and transition energies obtained in this work were used to modify the ^{195}Au decay scheme to that presented in Figure 39. This decay scheme is consistent with the conversion coefficients and admixtures determined later in this report.

The internal conversion coefficients for the transitions in ^{195}Pt can be determined from the electron intensities of Table 13 and the normalized gamma-ray intensities given in Table 14. The conversion coefficients calculated using these normalized gamma-ray intensities are given in Table 15 along with theoretical values. The only conversion coefficient previously measured was for K-conversion of the 98.8 keV transition. The value determined in this work, $\alpha_K^{98.8} = 6.8 \pm 1.5$, is in agreement to within experimental uncertainties with previous values of 5.9 ± 0.7 (ref. 119), 5.8 ± 1.5 (ref. 138), 6.01 ± 0.15 (ref. 123), $7.4^{+8.2}_{-2.8}$ (ref. 137), and 8.4 ± 0.5 (ref. 136). The rather large uncertainty in the present value is due to the uncertainty in the normalization factor for the gamma-ray

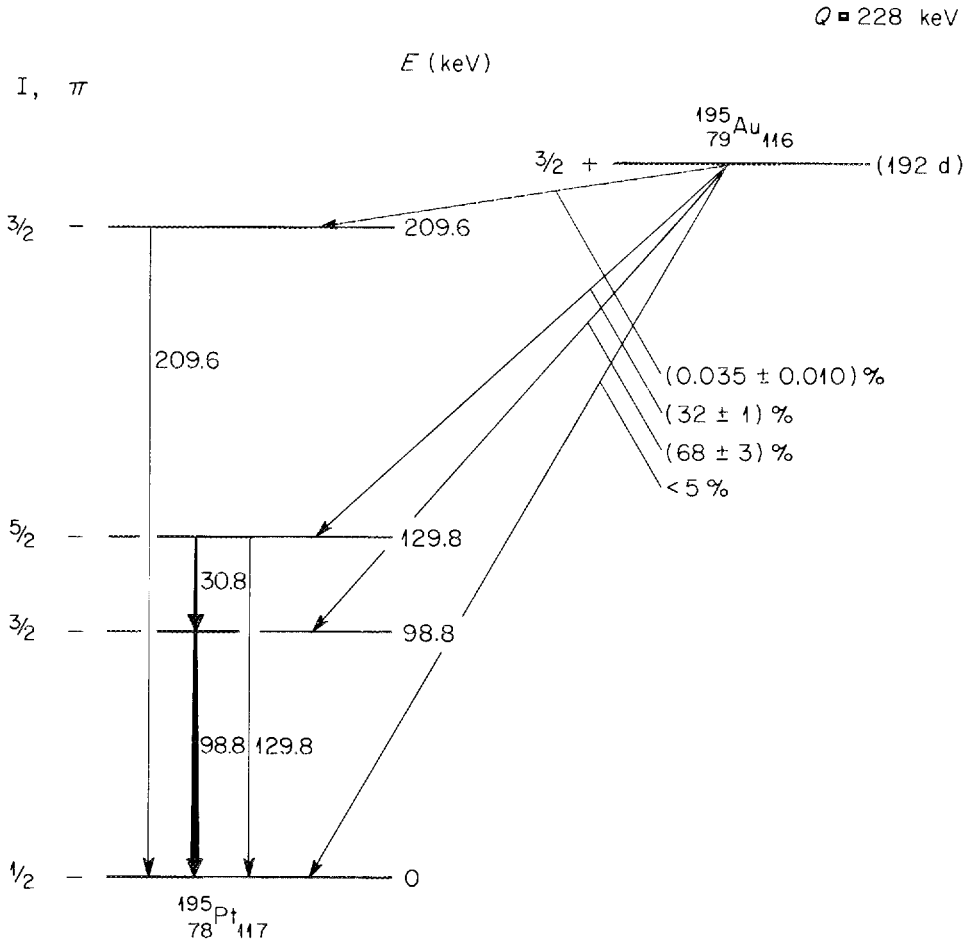

Fig. 39. The decay scheme of ^{195}Au.

TABLE 15

MEASURED AND THEORETICAL CONVERSION COEFFICIENTS

Transition Energy	Conversion Coefficient	Conversion Coefficient Values				
		This work	Sliv and Band[a]		Rose[b]	
			M1	E2	M1	E2
30.8 keV	α_{L_1}	17.5±4.5	27.3	8.82	21.5	8.4
	α_{L_2}	1.37±0.63	2.68	455	2.15	480
	α_{L_3}	0.24 ±0.08	0.306	532	0.30	640
	α_{M_1}	3.5±1.4	-	-	11.5	3.35
	α_{M_2}	0.42±0.24	-	-	1.2	220
	α_T	24.4±7.0	-	-	-	-
98.8 keV	α_K	6.8±1.5	5.74	0.695	5.8	0.71
	α_{L_1}	0.90±0.20	0.878	0.103	0.81	0.10
	α_{L_2}	0.086±0.017	0.0888	1.82	0.076	1.72
	α_{L_3}	0.026±0.006	0.00871	1.55	0.0085	1.44
	α_T	8.1±1.8	-	-	-	-
129.8 keV	α_K	0.46*	50.8(M3)	0.461	55(M3)	0.46
	α_{L_1}	0.031±0.010	28.3(M3)	0.057	34(M3)	0.06
	α_{L_2}	0.42±0.11	4.96(M3)	0.520	5.1(M3)	0.53
	α_{L_3}	0.31±0.06	27.7(M3)	0.402	28(M3)	0.48
	α_T	1.51±0.4	-	-	-	-
210 keV	α_K	0.12±0.06	0.678	0.150	0.70	0.15

a) Computer interpolated values from reference 88
b) Graphically interpolated values from reference 90.
* Normalized at this value.

intensities. There are approximately 10% error limits on both the electron intensity and the gamma-ray intensity of the line used for normalization.

In many cases the calculated conversion coefficients differ greatly from the theoretical values for pure multipoles; however, no multipole admixtures will bring about a more consistent agreement. Comparisons between theoretical and experimental conversion coefficients indicate the following multipolarities; 30.8 keV transition, pure M1; 98.8 keV transition, pure M1; 129.8 keV transition, pure E2, and 209.6 keV transition, pure E2.

A second method of assigning multipolarities is to compare K/L and L-subshell conversion-electron intensity ratios deduced from measured electron intensities with ratios deduced from theory. The L-subshell intensity ratios are much more sensitive to multipolarity changes than K/L ratios and are applied whenever the resolution is sufficient to obtain individual L-subshell relative intensities. The intensity ratios for L-subshell conversion-electrons for mixed M1-E2 transitions are related to the conversion coefficients by

$$\frac{I_{L_i}}{I_{L_f}} = \frac{A\alpha^{M1}_{L_i} + B\alpha^{E2}_{L_i}}{A\alpha^{M1}_{L_f} + B\alpha^{E2}_{L_f}} \tag{76}$$

where A is the fraction of magnetic dipole character and B is the fraction of

electric quadrapole character of the radiation; $\alpha^{M1}_{L_i}$ and $\alpha^{E2}_{L_i}$ are the M1 and E2 internal conversion coefficients for the L_i subshell. I_{L_i} and I_{L_f} are L-subshell relative electron intensities. The above relationship can be rearranged to give an expression for the M1/E2 admixture ratio

$$\frac{M1}{E2} = \frac{\alpha^{E2}_{L_i} - \left(\frac{I_{L_i}}{I_{L_f}}\right)\alpha^{E2}_{L_f}}{\alpha^{M1}_{L_f}\left(\frac{I_{L_i}}{I_{L_f}}\right) - \alpha^{M1}_{L_i}} \quad . \tag{77}$$

The admixtures for the three major gamma-ray transitions in ^{195}Pt were calculated by means of Equation (77) along with the electron intensities of Table 13 and the theoretical conversion coefficients of Table 15. In principle the same admixture should be obtained for each of the three L-subshell ratios (only two of which are independent); however, this is not always true as has been pointed out by Novakov and Hollander.[139] The admixtures obtained in this way have been found to differ between different L-subshell ratios by as much as 50%. For pure multipoles the L-subshell ratios may differ by more than 10% from the theoretical values. The L-subshell intensity ratios obtained for the three major transitions (the L-subshell conversion line intensities associated with the 209.6 keV transition were too weak to be observed) are compared to theoretical pure multipole values in Table 16. The uncertainties assigned to the L-subshell intensity ratios are based on uncertainties of less than 3% in the relative intensities of the

TABLE 16

COMPARISON OF EXPERIMENTAL AND THEORETICAL L-SUBSHELL RATIOS IN THE DECAY OF ^{195}AU

Photon energy (keV)	L-subshell ratio	L-subshell values				
		Experiment (this work)	Theory (Rose[a])		Theory (Sliv[b])	
			E2	M1	E2	M1
30.8 keV	L_1/L_2	12.8±0.5	0.0175	10.0	0.0194	10.2
	L_1/L_3	74.1±16.2	0.0131	71.5	0.0166	89.2
	L_2/L_3	5.82±1.20	0.750	7.15	0.855	8.75
98.8 keV	L_1/L_2	10.4±0.6	0.058	10.6	0.0566	9.89
	L_1/L_3	34.3±0.8	0.069	96	0.0665	101
	L_2/L_3	3.28±0.1	1.19	9.0	1.17	10.2
129.8 keV	L_1/L_2	0.073±0.023	0.119	6.66(M3)	0.110	5.70(M3)
	L_1/L_3	0.100±0.031	0.131	1.19(M3)	0.142	1.02(M3)
	L_2/L_3	1.36±0.14	1.10	0.18(M3)	1.29	0.179(M3)

a) Graphical interpolation of the tabulated values of reference 90.

b) Conversion coefficients interpolated from reference 88 for these energies by a computer and obtained from the Nuclear Data Project, Directors Division, Oak Ridge National Laboratory.

L-subshell lines. The uncertainties in the relative L-subshell intensities are much smaller than the corresponding uncertainties quoted in Table 13 which include uncertainties in the normalization factors. The theoretical values in Table 16 were derived from values interpolated from log α versus k plots of the tabulated conversion coefficients of Rose[90] and from values interpolated by a computer from the tabulated conversion coefficients of Sliv and Band.[88] The values derived from Rose's work may include uncertainties of up to 10% due to the interpolation procedure, while the computer interpolated values of Sliv and Band should be accurate to approximately 3%.

A summary of the admixtures calculated by means of conversion coefficient and by means of Equation (77) is presented here for each of the transitions populated in the electron capture decay of ^{195}Au.

The 30.8 keV Transition.

The conversion coefficients of the 30.8 keV transition, although differing from the theoretical values, are nearly in agreement within the experimental uncertainties. No E2 admixture would bring about closer agreement. The L-subshell ratios for this transition show wide variation from ratios for an M1 transition as deduced from theory; however, again no E2 admixture ($<$ 0.05% E2) would bring about better agreement. The experimental L-subshell ratios are in closest agreement with the values deduced from the theoretical conversion coefficients of Rose while the experimental values differ from the ratios deduced from the conversion coefficients of Sliv by as much as 20%.

The 98.8 keV Transition.

The 98.8 keV transition is found to have a small E2 admixture. A comparison of L-conversion coefficients shows approximately a 1% E2 admixture; whereas the K-conversion coefficient indicates pure M1. With the interpolated conversion coefficients of Rose we calculate multipolarities of: $(99.89 \pm 0.30)\%$ M1, $(98.96 \pm 0.03)\%$ M1, and $(98.43 \pm 0.11)\%$ M1 for the L_1/L_2, L_1/L_3, and L_2/L_3 ratios, respectively. Using the theoretical conversion coefficients of Sliv and Band we obtain: $(99.78 \pm 0.22)\%$ M1, $(98.90 \pm 0.10)\%$ M1, and $(98.30 \pm 0.10)\%$ M1, respectively. The final multipolarity assignment of $(99 \pm 1)\%$ M1 for the 98.8 keV transition is an average of the values calculated above. The uncertainty in this value was assigned large enough to include the extremes of the individual admixtures included in the average. The $(99 \pm 1)\%$ M1 admixture for this transition is in close agreement with the previous assignments of pure M1[134, 135, 137, 138] or small (1.42%)[133] E2 admixtures.

The 129.8 keV Transition.

No comparison to theory is possible for the 129.8 keV K-conversion line since it was used for normalization; however, the calculated L-subshell conversion coefficients appear to be about 30% lower than the theoretical E2 values. The angular momentum of the initial and final states for this transition rules out a possible M1 admixture; however an M3 admixture is possible. A comparison of measured L-subshell intensity ratios with those

deduced from theory show that no M3 admixture will bring closer agreement for the L-subshell ratios. If the measured L_1 line intensity was 30% larger and the L_2 line intensity 30% smaller close agreement would be obtained among the L-subshell ratios. Variations of the measured intensities of this magnitude are, however, outside the limits of error of this work, especially for the L_2 line intensity.

The 209.6 keV Transition.

The K-conversion coefficient of the 209.6 keV transition is indicative of a pure E2 transition in contrast to the angular correlation results of McGowan and Stelson[138] which gave 88% M1.

APPENDIX I

INVESTIGATION OF THE ACCURACY OF THE CAPACITANCE MANOMETER CALIBRATION

The cross section measurements of this work were made with target gas pressures in the region from 1×10^{-4} to 1×10^{-3} torr. Since the calibration of the capacitance manometer used to measure the gas pressure had only been checked by the manufacturer for the pressure range from 0.1 to 1.0 torr, it was necessary to investigate the accuracy of the calibration at lower pressures. This investigation was carried out by a comparison of the pressure readings of the capacitance manometer with those of a McLeod gage. A McLeod gage with a volume of 2192 cc and a capillary diameter of 0.534 mm (Consolidated Vacuum Corporation, Model GM-110) was used to obtain a measure of the reference pressure. The pressure measured by the McLeod gage was obtained from the equation*

$$P(\text{torr}) = 1.023 \times 10^{-7} (h_o - h_1)(h_2 - h_1) \qquad (78)$$

where the quantities h_o, h_1, and h_2 are defined in Figure 40 and were measured experimentally by means of a cathetometer. With care in reading and proper considerations for systematic McLeod gage errors, an accuracy of 1 to 3% can be obtained for pressure measurements as low as 1×10^{-4} torr.

*See reference 140.

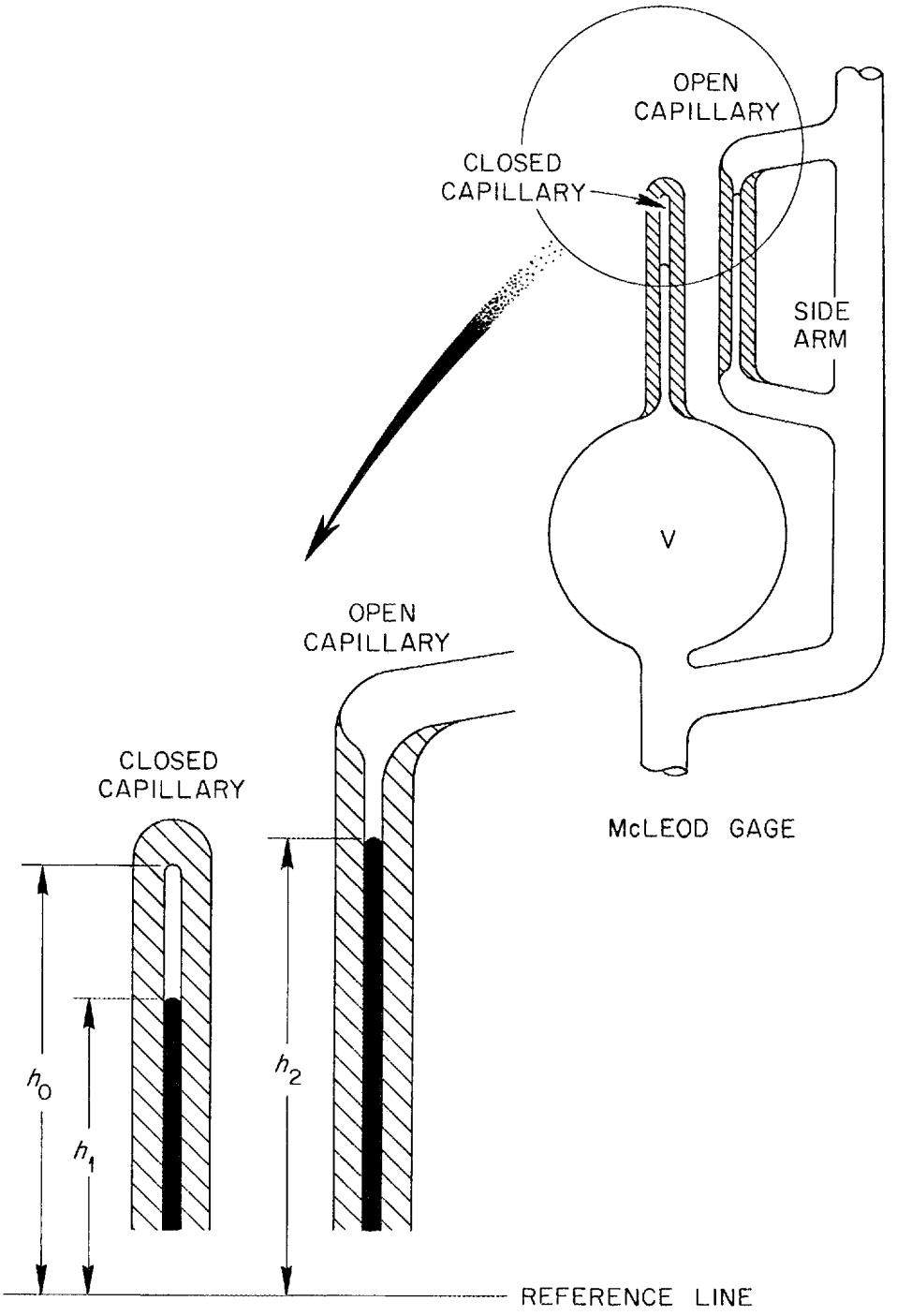

Fig. 40. The schematic representation of the McLeod gage which defines the quantities h_o, h_1, and h_2.

The three major causes of systematic errors in the use of a McLeod gage have been investigated by several authors.[141-146] These errors arise from (1) deviations from Boyle's Law, (2) different capillary depressions in the capillaries, and (3) mercury vapor streaming from the McLeod gage to the cold trap which is used to isolate the McLeod gage from the rest of the vacuum system. Extreme care must be taken to reduce or eliminate these systematic errors since any one of them may cause an error of 10% or more in the pressure readings obtained.

Deviations from Boyle's Law or the perfect gas low include the following: (1) the effect of gases which condense during compression, (2) the effect of adsorption and desorption of gases on the walls of the gage, and (3) the fact that a real gas obeys a non-ideal gas law such as that expressed by the Van der Waal equation. The errors due to these properties are eliminated by using non-condensable gases such as hydrogen, helium, nitrogen, argon, etc. and by thoroughly outgassing the McLeod gage system. In the present work only hydrogen and nitrogen gases were used and the system was heated while under vacuum in order to remove adsorbed gases.

The mercury streaming error results from mercury vapor streaming from the McLeod gage into the cold trap which isolates the McLeod gage mercury from the gage being calibrated. The mercury vapor sweeps along other gas molecules and exerts the same pumping action as occurs in a diffusion pump. This process may introduce an error of as much as 25% for

N_2 and 35% for Xe.[141,143] Since the mercury vapor pressure is a strong function of temperature, 1.9×10^{-4} torr at 0°C and 18.0×10^{-4} torr at 25°C (see reference 142), the streaming error may be reduced by cooling the McLeod gage mercury. In the present calibration work the mercury was cooled to approximately -15°C by placing the McLeod gage inside of a household freezer as shown in Figure 41. Cooling the McLeod gage to a temperature lower than the temperature of the gas chamber in which the pressure is to be measured introduces a pressure differential due to the temperature gradient. A correction for this pressure differential caused by thermal transpiration is given by the ratio $(T_g/T_m)^{\frac{1}{2}}$ where T_g is the temperature of the gas in the gas cell and T_m is the McLeod gage temperature.[147] The gas pressure measured by the cooled McLeod gage was multiplied by this ratio before comparison to the corresponding pressure measured by the capacitance manometer.

When mercury is raised in a McLeod gage which has been pumped to a high vacuum, the level of the mercury in each of the capillaries of equal cross section should be identical. However, the mercury in the capillary above the mercury reservoir may be uniformly depressed with respect to the side capillary. This uniform depression will result in an error in the pressure reading when gas has been introduced. One must determine the extent of this depression and correct for it. The magnitude of the capillary depression is determined by stopping the mercury at successive heights in the capillaries

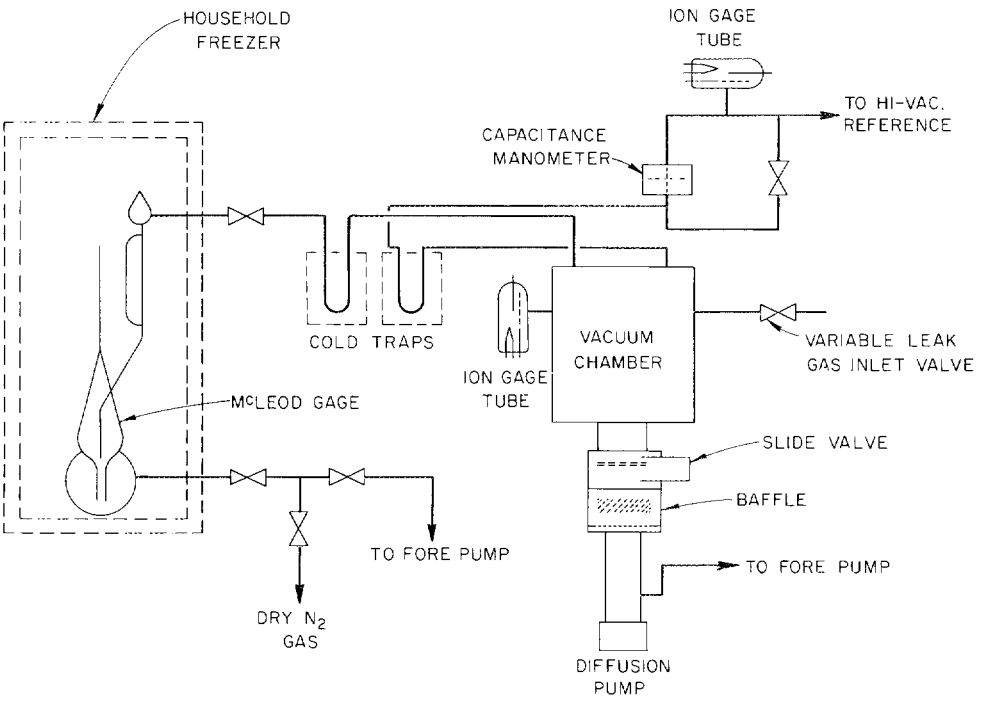

Fig. 41. A schematic drawing of the apparatus used to check the calibration of the capacitance manometer at low gas pressures.

and plotting Δh versus $1/H$ ($\Delta h = h_2 - h_1$ and $H = h_o - h_1$, where h_o, h_1, and h_2 are defined in Figure 40), the resulting straight line will intercept the Δh axis at $-\Delta h_d$ where Δh_d is the capillary depression. The true pressure can then be determined from the following equation

$$P = K(\Delta h + \Delta h_d)(H + a) \tag{79}$$

where K is the numerical constant given in Equation (78). The sorption constant a is negligible for the gases, nitrogen ($a_{N_2} = 1 \times 10^{-6}$ cm) and hydrogen ($a_{H_2} = 5 \times 10^{-8}$ cm), used in this work. The magnitude of the capillary depression Δh_d can be reduced or eliminated by proper cleaning of the capillaries, this cleaning includes thorough outgassing, and by using very clean mercury. In the present work the capillaries were heated with a torch flame while the system was evacuated to approximately 2×10^{-7} torr in order to remove adsorbed gases and only triple distilled mercury was used in the McLeod gage. In order to determine the extent of capillary depression in the present work, the mercury was stopped at successive heights in the capillaries and values of h_o, h_1, and h_2 measured. The results of these measurements are represented as a plot of Δh versus $1/H$ in Figure 42. The Δh intercept in Figure 42 indicates that Δh_d is negligible to within an uncertainty of approximately 1.0 mm. This uncertainty in Δh_d results in an uncertainty in the calculated McLeod gage pressure of approximately 3% at 1×10^{-4} torr and less than 2% at 5×10^{-4} torr.

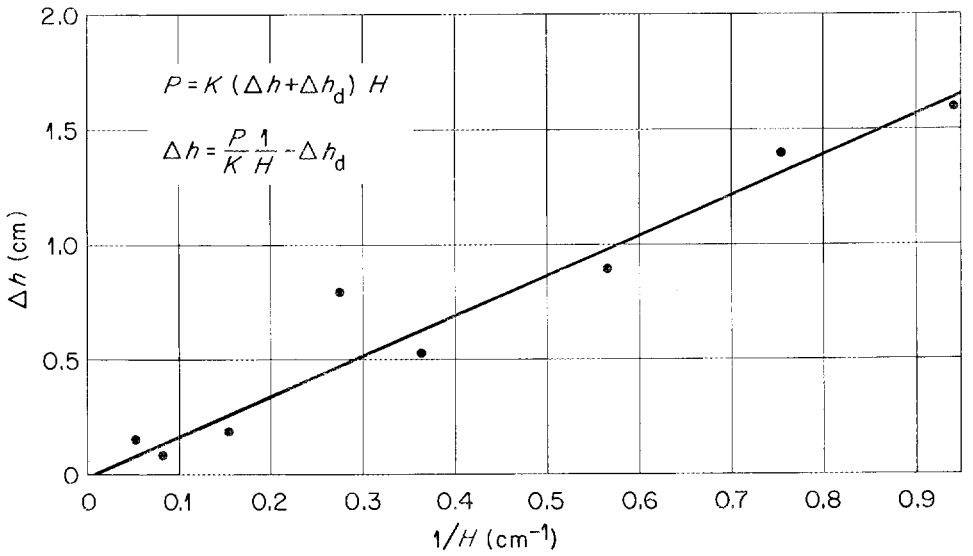

Fig. 42. The quantity Δh plotted versus 1/H. The Δh intercept is the value of the capillary depression, Δh_d, for the McLeod gage used in this work.

By careful consideration of the systematic McLeod gage errors, the reference pressure can be obtained with an accuracy of approximately 3% over the pressure range from 1×10^{-4} to 5×10^{-3} torr. Figure 43 shows the close agreement between the capacitance manometer and McLeod gage pressure readings. The agreement is well within the experimental uncertainties associated with each point.

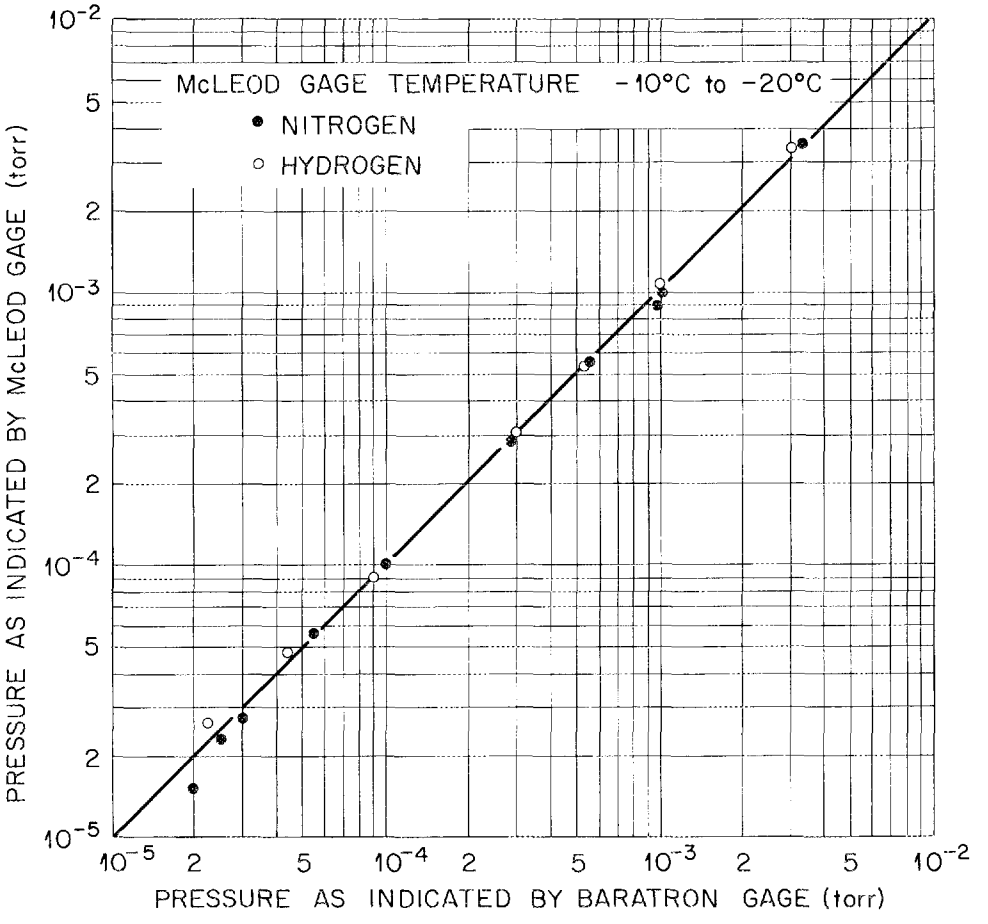

Fig. 43. A comparison of the gas pressures measured with the capacitance manometer and with the McLeod gage.

APPENDIX II

CALCULATION OF ADDITIONAL LENGTH OF THE COLLISION CELL DUE TO DIFFERENTIAL PUMPING

An estimate of the additional length of the collision cell due to gas streaming out of the apertures can be made with the aid of two assumptions. The first assumption is that the gas exhibits molecular flow in passing out of the aperture. The conditions of molecular flow are given by

$$aP_{\mu} < 5^{*} \tag{80}$$

where

a = characteristic dimensions in cm

P_{μ} = gas pressure in microns (1 micron = 10^{-3} torr).

For this calculation the characteristic dimension is taken to be the diameter of the aperture. Since the diameter of the apertures is less than 0.062 inches (0.157 centimeters) the assumption of molecular flow is valid at gas pressures less than 10 microns. In the present work the pressure was less than 1 micron on both sides of the apertures for all cross section measurements.

The second assumption made in this calculation is that the flow out of the aperture is isotropic. This would indicate that the pressure would decrease radially outside of the collision cell aperture as $1/r^2$ at distances greater than the aperture radius. Figure 44 is a sketch of the conditions assumed.

*See reference 140.

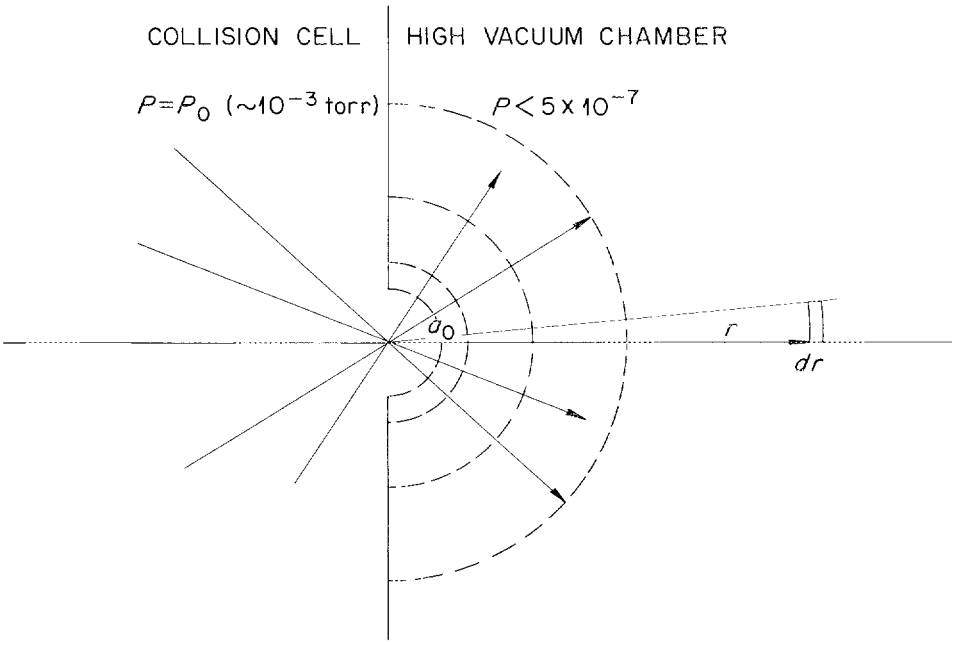

Fig. 44. A sketch of the conditions assumed in calculating the effective increase in the collision cell path length due to differential pumping of the cell.

Under the conditions of isotropic molecular flow the pressure at a point a_o, where a_o is the radius of the aperture, along r is the same as the pressure within the gas cell. The pressure at a given distance r where $r > a_o$ is given by

$$P = \frac{k}{r^2} \quad . \tag{81}$$

The constant k is evaluated by the condition that at $r = a_o$, $P = P_o$; therefore

$$k = P_o a_o^2 \tag{82}$$

where P_o is the measured gas pressure within the collision chamber.

The affects on the measured cross sections caused by gas flowing out of the apertures are due to the increased value of the product $P\ell$ relative to the product of the measured pressure P_o inside the collision chamber and the measured length of the collision chamber ℓ_o. The total "effective" value $P\ell$ is given by

$$P\ell = P_o\ell_o + P_o(a_{o_1} + a_{o_2}) + \int_{a_{o_1}}^{\infty} k/r^2 dr + \int_{a_{o_2}}^{\infty} k/r^2 dr \tag{83}$$

where

P = effective pressure

ℓ = effective path length

P_o = pressure within the gas cell

ℓ_o = measured cell path length

a_{o_1} = entrance aperture radius

a_{o_2} = exit aperture radius

k = constant determined from Equation (81) .

The value of $P\ell$ was evaluated for $P_o = 5 \times 10^{-4}$ as this pressure was near the center of the range of pressures used in the cross section measurements. Since P and ℓ individually cannot be calculated, the results are most conveniently represented in terms of the percent addition to the number density $P_o \ell_o$. This percent increase is given by

$$\frac{(P\ell - P_o \ell_o) \times 100}{P_o \ell_o} = \% \text{ end effects} . \qquad (84)$$

The increase in $P_o \ell_o$ due to end effects may be considered as an effective increase in the length ℓ_o where the pressure is taken to be the measured value P_o. For the short cell ($\ell_o = 3.06 \pm 0.06$ inches), which had $a_{o_1} = 0.020$ inches and $a_{o_2} = 0.062$ inches, the percent effective increase in ℓ_o was found to be 2.7%. Since the apertures were of the same dimensions for the long cell as for the short cell the additional length due to differential pumping is also the same; however, the percent increase in the long cell ($\ell_o = 17.5 \pm 0.06$ inches) will be less. The effective increase in the length of the long cell was found to be less than 0.5% based upon this approximate calculation.

BIBLIOGRAPHY

1. D. R. Bates and R. McCarroll, Phil. Mag. Sup. 11, 39 (1962).
2. D. R. Bates, in Atomic and Molecular Processes, edited by D. R. Bates (Academic Press, New York, 1962) p. 550.
3. M. H. Mittleman, Proc. Phys. Soc. (London) 81, 633 (1963).
4. A. Dalgarno, in Atomic Collision Processes, edited by M. R. C. McDowell (John Wiley and Sons, Inc., New York, 1964) p. 609.
5. R.H. Fowler, Phil. Mag. 47, 416 (1924).
6. L. H. Thomas, Proc. Roy. Soc. (London) A114, 561 (1927).
7. C. J. Cook, Proc. Phys. Soc. (London) 81, 789 (1963).
8. D. R. Bates and R. A. Mapleton, Proc. Phys. Soc. (London) 87, 657 (1966).
9. D. R. Bates and R. A. Mapleton, Proc. Phys. Soc. (London) 90, 909 (1967).
10. N. Bohr, Kgl. Danske Videnskab. Selskab. Mat.-Fys. Medd. 18 No. 8, 105 (1948).
11. I. S. Dmitriev and V. S. Nikolaev, Soviet Phys.-JETP 17, 447 (1963).
12. Michal Gryziński, Phys. Rev. A138, 336 (1965).
13. J. R. Oppenheimer, Phys. Rev. 31, 349 (1928).
14. H. C. Brinkman and H. A. Kramers, Proc. Acad. Sci. (Amsterdam) 33, 973 (1930).
15. H. S. W. Massey and R. A. Smith, Proc. Roy. Soc. (London) A142, 142 (1933).

16. G. C. Wick, see note added in proof by Jackson and Schiff in reference 20.

17. J. P. Keene, Phil. Mag. 40, 369 (1949).

18. F. Ribe, Phys. Rev. 83, 1217 (1951).

19. A. C. Whittier, Can. J. Phys. 32, 275 (1954).

20. J. D. Jackson and H. Schiff, Phys. Rev. 89, 359 (1953).

21. D. R. Bates and A. Dalgarno, Proc. Phys. Soc. (London) A65, 919 (1952) and A66, 972 (1953).

22. R. M. Drisko, Ph. D. thesis, Carnegie Institute of Technology (1955), unpublished.

23. R. H. Bassel and E. Gerjuoy, Phys. Rev. 117, 749 (1960).

24. D. R. Bates, Proc. Roy. Soc. (London) A247, 294 (1958).

25. R. A. Mapleton, Phys. Rev. 126, 1477 (1962).

26. R. A. Mapleton, Phys. Rev. 130, 1829 (1963).

27. R. A. Mapleton, Phys. Rev. 130, 1839 (1963).

28. R. A. Mapleton, Proc. Phys. Soc. (London) 85, 1109 (1965).

29. R. A. Mapleton, Phys. Rev. 145, 25 (1966).

30. V. S. Nikolaev, Soviet Phys.-JETP 24, 847 (1967).

31. T. F. Taun and E. Gerjuoy, Phys. Rev. 117, 756 (1960).

32. R. Aaron, R. Amado, and B. Lee, Phys. Rev. 121, 319 (1961).

33. K. Dettmann and G. Leibfried, Phys. Rev. 148, 1271 (1966).

34. D. R. Bates and G. Griffing, Proc. Phys. Soc. (London) A66, 961 (1953).

35. D. R. Bates and A. Dalgarno, Proc. Phys. Soc. (London) A66, 972 (1953).

36. D. R. Bates and G. Griffing, Proc. Phys. Soc. (London) A68, 90 (1955).

37. D. R. Bates and A. Williams, Proc. Phys. Soc. (London) A70, 306 (1957).

38. B. H. Bransden and I. M. Cheshire, Proc. Phys. Soc. (London) 81, 820 (1963).

39. M. R. C. McDowell, Proc. Roy. Soc. (London) A264, 277 (1961).

40. R. McCarroll, Proc. Roy. Soc. (London) A264, 547 (1961).

41. C. D. Moak, H. E. Banta, J. N. Thurston, J. W. Johnson, and R. F. King, Rev. Sci. Instr. 30, 694 (1959).

42. Samuel K. Allison, Rev. Mod. Phys. 30, 1137 (1958).

43. S. K. Allison and M. Garcia-Munoz, in Atomic and Molecular Processes, edited by D. R. Bates (Academic Press, New York, 1962) p. 721.

44. Lloyd L. Small, Analytic Geometry and Calculus (Appleton-Century-Crafts, Inc., New York, 1953) p. 472.

45. C. F. Barnett and H. K. Reynolds, Phys. Rev. 109, 355 (1958).

46. J. F. Williams, Phys. Rev. 157, 97 (1967).

47. L. M. Welsh, K. H. Berkner, S. N. Kaplan, and R. V. Pyle, Phys. Rev. 158, 85 (1967).

48. U. Schryber, Helv. Phys. Acta 39, 562 (1966).

49. R. A. Mapleton, Phys. Rev. 122, 528 (1961).

50. B. H. Bransden and L. T. Sin Fai Lam, Proc. Phys. Soc. (London) 87, 653 (1966).

51. P. M. Stier and C. F. Barnett, Phys. Rev. 103, 896 (1956).

52. R. A. Mapleton, Private Communication, 1967.

53. K. Watanabe, T. Nakayama, and J. Mottl, Internal Report, Dept. of Phys., Univ. of Hawaii (Dec. 1959).

54. Wade L. Fite, in Atomic Collision Processes, edited by D. R. Bates (Academic Press, New York, 1962) p. 421.

55. Marvin H. Mittleman, Phys. Rev. A137, 1 (1965).

56. V. I. Gerasimenko, Soviet Phys.-JETP 14, 789 (1962).

57. L. N. Rosentsveig and V. I. Gerasimenko - see reference 56 [unpublished, Karkow State University (U.S.S.R.)].

58. M. H. Mittleman, Proc. Roy. Soc. (London) 277, 206 (1964).

59. Y. M. Fogel, Soviet Phys.-Usp. 3, 390 (1960).

60. J. F. Williams, Phys. Rev. 153, 116 (1967).

61. G. W. McClure, Phys. Rev. 132, 1636 (1963).

62. Y. M. Fogel, R. V. Mitin, V. G. Kozlov, and N. D. Romashko, Soviet Phys.-JETP 8, 390 (1959).

63. V. V. Afrosimov, R. N. Il'in, and E. S. Solov'en, Soviet Phys.-Tech. Phys. 5, 661 (1960).

64. E.H. S. Burhop, The Auger Effect and Other Radiationless Transitions, (Cambridge University Press, Cambridge, 1952).

65. Gerhard Herzberg, Spectra of Diatomic Molecules (D. Van Nostrand Company, Inc., Princeton, N.J., 1950).

66. Robert B. Leighton, Principles of Modern Physics (McGraw-Hill Book Company, Inc., New York, 1959).

67. W. N. Asaad and E. H. Burhop, Proc. Phys. Soc. (London) 71, 369 (1958).

68. O. Hörnfeldt, Arkiv Fysik 23, 235 (1962).

69. I. Bergström and R. D. Hill, Arkiv Fysik 8, 21 (1954).

70. M. Mladjenovic and H. Slatis, Arkiv Fysik 9, 41 (1954).

71. M. A. Listengarten, Izv. Akad. Nauk SSSR (ser. fiz) 24, 1041 (1960), transl. Bull. Acad. Sci. USSR (Phys. Ser.) 24, 1050 (1960).

72. W. N. Asaad, Proc. Roy. Soc. (London) A249, 555 (1959).

73. W. N. Asaad, Nucl. Phys. 44, 399 (1963).

74. W. N. Asaad, Nucl. Phys. 66, 494 (1965).

75. H. Körber and W. Mehlhorn, Z. Physik 191, 217 (1966).

76. W. Mehlhorn and W. N. Asaad, Z. Physik 191, 231 (1966).

77. W. Mehlhorn and R. G. Albridge, Z. Physik 175, 508 (1963).

78. R. A. Rubenstein and J. N. Snyder, Phys. Rev. 97, 1653 (1955).

79. R. A. Rubenstein, Ph. D. thesis, University of Illinois (1955).

80. W. N. Asaad, Nucl. Phys. 44, 415 (1963).

81. W. N. Asaad, paper presented at the Conference on the Role of Atomic Electrons in Nuclear Transformations, Warsaw, Sept. 1963.

82. W. N. Asaad, Nucl. Phys. 63, 337 (1965).

83. E. H. S. Burhop, J. Phys. Radium 16, 625 (1955).

84. H. L. Hagedoorn and A. H. Wapstra, Nucl. Phys. 15, 146 (1960).

85. M. E. Rose, in Alpha-, Beta-, and Gamma-ray Spectroscopy, edited by K. Siegbahn (North Holland Publishing Company, Amsterdam, 1965) p. 887.

86. M. E. Rose, in Internal Conversion Processes, edited by J.H. Hamilton (Academic Press, New York, 1966) p. 15.

87. E. L. Church and J. Weneser, Phys. Rev. 104, 1382 (1956).

88. L. A. Sliv and I. M. Band, in Alpha-, Beta-, and Gamma-Ray Spectroscopy, edited by K. Siegbahn (North Holland Publishing Company, Amsterdam, 1965) p. 1639.

89. K. Umeda, J. Fac. Sci. Hokkaido Imp. Univ. II 3, 171 (1942).

90. M. E. Rose, Internal Conversion Coefficients (North Holland Publishing Company, Amsterdam, 1958).

91. J. C. Nall, Q. L. Baird, S. K. Haynes, and J. H. Hamilton, Nucl. Instr. & Meth. 16, 275 (1964).

92. W. Mehlhorn and R. G. Albridge, Nucl. Inst. & Meth. 26, 37 (1964).

93. R. O. Lane and D. J. Zaffarano, Ames Laboratory, Iowa State College, Ames, Iowa, U.S.A.E.C. Report I.S.C.-439 (December 1963).

94. D. C. Hall, Masters thesis, Vanderbilt University, Nashville, Tenn., 1965.

95. M. J. Zender, Ph.D. thesis, Vanderbilt University, Nashville, Tenn., 1966.

96. T. R. Duncan, Masters thesis, Vanderbilt University, Nashville, Tenn., 1961.

97. Z. Sujkowski and H. Slätis, Arkiv Fysik 14, 101 (1958).

98. W. R. Casey and R. G. Albridge, to be published.

99. J. C. Nall. Q. L. Baird, and S. K. Haynes, Phys. Rev. 118, 1278 (1960).

100. Z. Sujowski and O. Melin, Arkiv Fysik 20, 193 (1961).

101. C. Sébille and F. Widemann, Compt. Rend. 258, 5636 (1964).

102. J. S. Dionisio, Compt. Rend. 254, 257 (1962).

103. J. S. Dionisio, Compt. Rend. 254, 1972 (1962).

104. R. G. Albridge and J. M. Hollander, Nucl. Phys. 27, 554 (1961).

105. G. Albouy and M. Valadares, Compt. Rend. 250, 2877 (1960).

106. S. Rosenblum, J. S. Dionisio, and M. Valadares, J. Phys. Radium 17, 112 (1956).

107. J. S. Dionisio, Ann. Phys. (Paris) 9, 29 (1964).

108. R. Päschke, Z. Physik 176, 143 (1963).

109. M. O. Krause, private communication (1965).

110. Werner Mehlhorn, Z. Physik 187, 21 (1965).

111. P. Erman and Z. Sujkowski, Arkiv Fysik 20, 209 (1961).

112. K. Risch, Z. Physik 150, 87 (1958).

113. I. Bergström and C. Nordling, in Alpha-, Beta-, and Gamma-Ray Spectroscopy, edited by K. Siegbahn (North Holland Publishing Company, Amsterdam, 1965) p. 1523.

114. J. L. Wolfson and A. P. Baerg, Can. J. Phys. 42, 1781 (1964).

115. W. Mehlhorn and R. G. Albridge, Z. Physik 175, 508 (1963).

116. R. D. Birkhoff, Handbuch der Physik, Vol. 34 (1958) p. 571.

117. F. Lenz, Z. Naturforsch. 9A, 185 (1954).

118. S. Hagstrom, C. Nordling, and K. Seigbahn, in Alpha-, Beta-, and Gamma-Ray Spectroscopy, edited by K. Siegbahn (North Holland Publishing Company, Amsterdam, 1965) p. 845.

119. J. R. Harris, G. M. Rothberg, and N. Benezer-Koller, Phys. Rev. 138B, 554 (1965).

120. H. Brysk and M. E. Rose, Rev. Mod. Phys. 30, 1169 (1958).

121. A. H. Wapstra, G. J. Nijgh, and R. van Lieshout, Nuclear Spectroscopy Tables (North Holland Publishing Company, Amsterdam, 1959).

122. E. J. Konopinski and M. E. Rose, in Alpha-, Beta-, and Gamma-Ray Spectroscopy, edited by K. Siegbahn (North Holland Publishing Company, Amsterdam, 1965) p. 1327.

123. W. Goedbloed, E. Mastenbroek, A. Kemper, and J. Blok, Physica 30, 2041 (1964).

124. W. Whaling, Handbuch der Physik 34, 202 (1958).

125. H. H. Hubbell, Jr., W. J. McConnell, and R. D. Birkhoff, Nucl. Instr. & Meth. 31, 18 (1964).

126. C. J. Herrlander, R. Stockendal, and R. K. Gupta, Arkiv Fysik 17, 315 (1960).

127. B. Jung and J. Svedberg, Nucl. Phys. 20, 630 (1960).

128. G. T. Ewan, Can. J. Phys. 35, 672 (1957).

129. G. T. Ewan, J. S. Geiger, R. L. Graham, and D. R. McKenzie, Can. J. Phys. 37, 174 (1959).

130. T. O. Passel, M. C. Michel, and F. Bergström, Phys. Rev. 95, 999 (1954).

131. C. D. Broyles, D. A. Thomas, and S. K. Haynes, Phys. Rev. 89, 715 (1953).

132. R. Steffen, O. Huber, and F. Humbel, Helv. Phys. Acta 22, 167 (1949).

133. P. J. Cressmann and R. G. Wilkinson, Phys. Rev. 109, 872 (1958).

134. L. P. Gillon, K. Gopalakrishman, A. de Shalit, and J. W. Mihelich, Phys. Rev. 93, 124 (1954).

135. J. M. Cork, M. K. Brice, L. C. Schmid, G. D. Hickman, and H. Nine, Phys. Rev. 94, 1218 (1954).

136. A. Bisi, E. Germagnoli, and L. Zappa, Nuovo Cimento 11, 843 (1959).

137. A de Shalit, O. Huber, and H. Schneider, Helv. Phys. Acta 25, 279 (1952).

138. F. K. McGowan and P. H. Stelson, Phys. Rev. 116, 154 (1959).

139. T. Novakow and J. M. Hollander, Nucl. Phys. 60, 593 (1964).

140. Saul Dushman, Scientific Foundations of Vacuum Technique, Second Edition, edited by J. M. Lafferty (John Wiley and Sons, Inc., New York, 1962).

141. H. Ishii and K. Nakayama, Transactions of the Eighth National Vacuum Symposium, 1961 (Pergamon Press, Oxford, England, 1962) Vol. 1, p. 519.

142. E. deVries and P. K. Rol, Vacuum 15, 135 (1964).

143. Ch. Minke and G. Reich, Vakuum Technik 11, 86 (1962).

144. Paul H. Carr, Vacuum 14, 37 (1963).

145. Erhard W. Rothe, J. Vac. Sci. Technol. I, 66 (1964).

146. N. G. Utterback and T. Griffith, Jr., Rev. Sci. Inst. 37, 866 (1966).

147. G. A. Miller, J. Phys. Chem. 67, 1359 (1963).

INTERNAL DISTRIBUTION

1. Biology Library
2-4. Central Research Library
5. Reactor Division Library
6-7. ORNL-Y-12-Technical Library, Document Reference Section
8-57. Laboratory Records Department
58. Laboratory Records, ORNL R.C.
59. V. E. Anderson
60. E. T. Arakawa
61. C. F. Barnett
62. P. R. Bell
63-87. R. D. Birkhoff
88. T. A. Carlson
89. J. G. Carter
90. J. L. Dunlap
91. M. F. Fair
92. M. P. Feezell
93. K. Fox
94. F. W. Garber
95. W. R. Garrett
96. R. H. Huebner
97. W. H. Jordan
98. G. G. Kelley
99. M. O. Krause
100-104. R. A. Langley
105. C. E. Larson
106. J. L. Liverman
107. E. T. Loy
108. H. G. MacPherson
109. W. J. McConnell
110. K. Z. Morgan
111. H. Postma
112. J. A. Ray
113. R. H. Ritchie
114. H. C. Schweinler
115. M. J. Skinner
116. A. H. Snell
117. W. S. Snyder
118. J. E. Turner
119. A. M. Weinberg
120. R. E. Wilems
121. J. E. Cantlon (consultant)
122. J. C. Frye (consultant)
123. J. B. Hursh (consultant)
124. J. L. MaGee (consultant)
125. H. O. Wyckhoff (consultant)

EXTERNAL DISTRIBUTION

126. V. V. Afrosimov, Ioffe Institute of Physics and Tech., Leningrad, USSR, Russia
127-136. R. G. Albridge, Department of Physics, Vanderbilt University, Nashville, Tennessee
137. W. N. Asaad, Faculty of Engineering, Cairo University, Cairo, Egypt
138. G. C. Barton, Department of Physics, Weber State College, Ogden, Utah 84403
139. D. R. Bates, Department of Applied Mathematics, Queen's University, Belfast 7, Northern Ireland
140. K. H. Berkner, Lawrence Radiation Laboratory, University of California, Berkeley, California
141. M. G. Boyce, Department of Mathematics, Vanderbilt University, Nashville, Tennessee

142. B. H. Bransden, Department of Physics, University of Durham, South Road, Durham City, Scotland
143. A. B. Brill, Department of Medicine, Vanderbilt University, Nashville, Tennessee
144. I. M. Cheshire, A.E.R.E., Harwell, Berkshire, England
145. S. W. Cram, Physics Department, Kansas State Teachers College, Emporia, Kansas
146. A. Dalgarno, Mathematics Department, Queen's University of Belfast, Belfast, Ireland
147. N. Dyer, Physics Department, Vanderbilt University, Nashville, Tennessee
148. P. Erman, Nobel Institute, Stockholm, Sweden
149. Wade L. Fite, University of Pittsburgh, Pittsburgh, Pennsylvania
150. M. Garcia-Munoz, Institute for Nuclear Studies, University of Chicago, Chicago, Illinois
151. E. Gerjuoy, Physics Department, University of Pittsburgh, Pittsburgh, Pennsylvania
152. D. H. Hall, 515 Irving, Elk River, Minnesota 55330
153. J. H. Hamilton, Department of Physics, Vanderbilt University, Nashville, Tennessee
154. W. Holladay, Physics Department, Vanderbilt University, Nashville, Tennessee
155. W. F. Huebner, Los Alamos Scientific Lab., University of California, P. O. Box 1663, Los Alamos, New Mexico 87544
156. R. E. Johnson, Physics Department, Vanderbilt University, Nashville, Tennessee
157. S. N. Kaplan, Lawrence Radiation Laboratory, University of California, Berkeley, California
158. R. A. Mapleton, Air Force Cambridge Research Lab., Bedford, Mass.
159. D. H. Martin, Physics Department, North Carolina State University, Raleigh, North Carolina
160. D. W. Martin, Physics Department, Georgia Institute of Technology, Atlanta, Georgia
161. R. McCarroll, Observatoire de Paris, Mendon, S-et-O, France
162. G. W. McClure, Physical Sciences, Sandia Corporation, Sandia Base, Albuquerque, New Mexico
163. E. W. McDaniel, Physics Department, Georgia Institute of Technology, Atlanta, Georgia
164. W. Mehlhorn, Institute for Nuclear Physics, University of Münster, 44 Münster (West f), Tibussstrasse 7-15, West Germany
165. M. H. Mittleman, Space Science Institute, University of California, Berkeley, California
166. M. Mladjenović, B. Kindric Institute, P.O. Box 522, Belgrade, Yugoslavia
167-191. M. Y. Nakai, Osaka Lab., Japan Atomic Energy Research Institute, 5-8 Mii, Neyagawa-City, Osaka, Japan

192. V. S. Nikolaev, Institute of Nuclear Physics, Moscow State University, USSR, Russia
193. Carl Nordling, Physics Institute, Uppsala, Sweden
194. W. T. Pinkston, Department of Physics, Vanderbilt University, Nashville, Tennessee
195. R. V. Pyle, Lawrence Radiation Laboratory, University of California, Berkeley, California
196. U. Schryber, Physikalisches Institute, Eidg. Technische Hochschule, Gloriastrasse 35, 8006 Zürich, Switzerland
197. K. Sevier, University of Uppsala, Sweden
198. L. T. Sin Fai Lam, Department of Physics, The University, Durham, England
199. P. Sinder, Atomic Energy Documentation Center at the Gmelin Institute, 7 Woodland Avenue, Larchmont, New York 10538
200. E. W. Thomas, Physics Department, Georgia Institute of Technology, Georgia
201. John Thun, Physics Institute, Uppsala, Sweden
202-226. L. H. Toburen, Pacific Northwest Laboratory, Battelle Memorial Institute, Richland, Washington 99352
227. L. M. Welsh, Directorate of Science and Technology, Deputy Chief of Staff for Research and Development, Headquarters USAF, Washington, D.C.
228. J. F. Williams, General Atomic, Box 608, San Diego, California
229-243. Division of Technical Information Extension
244-245. University Relations Division, Fellowship Office, Oak Ridge Associated Universities, Oak Ridge, Tennessee